Thermal transport in defective and disordered materials

Cite as: Appl. Phys. Rev. **8**, 031311 (2021); https://doi.org/10.1063/5.0055593
Submitted: 30 April 2021 . Accepted: 16 July 2021 . Published Online: 27 August 2021

Riley Hanus, Ramya Gurunathan, Lucas Lindsay, Matthias T. Agne, Jingjing Shi, Samuel Graham, G. Jeffrey Snyder, et al.

Applied Physics Reviews REVIEW scitation.org/journal/are

Thermal transport in defective and disordered materials

Cite as: Appl. Phys. Rev. 8, 031311 (2021); doi: 10.1063/5.0055593
Submitted: 30 April 2021 · Accepted: 16 July 2021 ·
Published Online: 27 August 2021

View Online Export Citation CrossMark

Riley Hanus,[1,a)] Ramya Gurunathan,[2] Lucas Lindsay,[3] Matthias T. Agne,[4] Jingjing Shi,[1] Samuel Graham,[1] and G. Jeffrey Snyder[2]

AFFILIATIONS

[1]Department of Mechanical Engineering, Georgia Institute of Technology, Atlanta, Georgia 30318, USA
[2]Materials Science and Engineering, Northwestern University, Evanston, Illinois 60208, USA
[3]Materials Science and Technology Division, Oak Ridge National Laboratory, Oak Ridge, Tennessee 37831, USA
[4]Institute for Energy and Climate Research, Helmholtz-Institute Münster, Münster 48149, Germany

[a)]Author to whom correspondence should be addressed: hanusriley@gmail.com

ABSTRACT

With significant recent advancements in thermal sciences—such as the development of new theoretical and experimental techniques, and the discovery of new transport mechanisms—it is helpful to revisit the fundamentals of vibrational heat conduction to formulate an updated and informed physical understanding. The increasing maturity of simulation and modeling methods sparks the desire to leverage these techniques to rapidly improve and develop technology through digital engineering and multi-scale, electro-thermal models. With that vision in mind, this review attempts to build a holistic understanding of thermal transport by focusing on the often unaddressed relationships between subfields, which can be critical for multi-scale modeling approaches. For example, we outline the relationship between mode-specific (computational) and spectral (analytical) models. We relate thermal boundary resistance models based on perturbation approaches and classic transmissivity based models. We discuss the relationship between lattice dynamics and molecular dynamics approaches along with two-channel transport frameworks that have emerged recently and that connect crystal-like and amorphous-like heat conduction. Throughout, we discuss best practices for modeling experimental data and outline how these models can guide material-level and system-level design.

TABLE OF CONTENTS

I. THERMAL SCIENCES AND TECHNOLOGIES

A. Motivating thermal

As technology calls for more extreme structural and functional materials, pushing the upper and lower limits of thermal conductivity (κ) is an important scientific endeavor.[1–3] Energy technologies, which consider thermal properties to be primary in design (e.g., thermoelectrics, thermal barrier coatings, thermal energy storage, battery thermal runaway), would greatly benefit from improved understanding and control of these limits. In fields where thermal properties are not considered to be primary (e.g., quantum information science, memristors, hypersonics), thermal properties can be closely tied to technological success. Developing these emerging technologies with thermal properties in mind can help identify engineering challenges and elucidate positive iterative design strategies. As performance limits are pushed to extremes in existing technologies (e.g., power electronics, communication electronics, opto-electronics, rapid charging of batteries), thermal management becomes critical and the co-design of electrical, optical, and thermal properties is necessary.

B. Digital engineering of transport

First principles simulations for thermal conductivity of perfect crystals has matured in the past decades,[4] and the level of confidence in such predictions is perhaps the highest of any transport property. In the coming decades, there is tremendous potential in leveraging these first principles predictions in multi-scale models for materials containing extended defects and in device-level simulations.

Digital engineering methods (e.g., integrated computational materials engineering, ICME) have accelerated the development of structural materials, and they have successfully transferred from academic research to industry (see "From Atoms to Autos" in Ref. 5). One critical aspect enabling this success is the development of length-scale bridging methodologies, which connect atomistic simulations to device level materials properties. These length-scale bridging methodologies are rarely "one size fits all." Different material and device classes often require tailored solutions, since the simplifying assumptions that are required and/or justified often change from case to case. There is a desire to apply similar digital engineering methods to electronic, thermal, and ionic transport; however, many of the required length-scale bridging methods require development and validation.

Since a solid computational baseline has been achieved in thermal transport of pristine materials, thermal transport is a logical field to pursue multi-scale digital engineering methods. The success of such a scientific initiative will pave the way for similar approaches in electronic and ionic transport, where first principles simulations are rapidly progressing.

C. Device-level considerations

While much focus is given to material level thermal properties in the literature, thermal heat sinking to the environment in device-level applications is often a primary challenge. When materials are incorporated into technological applications, the system-level heat transport problem should be considered; from the active material to the environment. For example, devices based on thin film thermoelectrics will often be forced into a regime where power is heat sink limited due to the large temperature gradients and heat fluxes required.[6] For power electronics, Warzoha *et al.* provided a detailed review that highlights how the electronics packaging of transistors (e.g., interfaces, substrates, and heat spreaders) significantly impacts the nanoscale thermal environment and device performance.[7] Even in amorphous HfO_2 memristors, where the active device is a conductive filament that can be tens of atoms in diameter, the long-range thermal environment set by the device substrate has been shown to impact the memristive behavior.[8,9] A common theme between these cases is that the thermal boundary condition from the device to environment is often critically important. Under fixed thermal boundary conditions, the material level properties become the primary factor influencing device performance.

D. Review outline

This review focuses on the materials physics governing thermal properties. Special attention is given to the interconnection of subfields, which is critical to multi-scale, digital engineering initiatives. Less focus will be given to material already covered in recent reviews,[4,10–14] and the reader will be directed to sections of these works periodically.

We start with a broad overview of thermal transport (Sec. II). Critical concepts such as vibrational wave packets, harmonic normal mode decomposition, and phonon-gas and diffuson conduction channels are introduced at a conceptual level. Mathematical formalism is reviewed in the Appendixes, which serve to establish notation and as technical reference for common computational and analytical equations and procedures. Content is then organized in increasing level of material disorder. First, phonons in perfect crystals are reviewed (Sec. III). Special focus is given to $\mathbf{q}$-point sampling and the long wavelength (near Γ-point), low frequency limit, since behavior in this limit is expected to become increasingly important when multi-scale models are developed that consider extended defects and far-field thermal effects. Second, phonons in defective crystals are reviewed (Sec. IV). Analytical scattering theory is used to build intuition about the frequency dependence of phonon-defect scattering. Then, materials systems where lattice softening has been found to be important are highlighted, and potential mechanisms are discussed. Third, thermal boundary resistance is reviewed (Sec. V). While this may be considered a sub-category of phonons in defective crystals, it is broken out into its own section due to the uniqueness of measurements, simulations, and models used. Finally, thermal transport in disordered materials is reviewed (Sec. VI). In this case, the phonon-gas model breaks down and new materials design principles are required. These methods are discussed in relation to recently developed two-channel lattice dynamics approaches (unified lattice dynamics,[15] quasi-harmonic Green-Kubo method[16]).

II. THERMAL TRANSPORT OVERVIEW

The thermal conductivity of a solid, κ, can be thought of as a sum of contributions from different heat conduction channels, which are commonly taken to be independent. The most common channels considered are atomic vibrations (κ_{vib}) and electronic carriers (κ_e):

$$\kappa = \kappa_{vib} + \kappa_e + \cdots . \tag{1}$$

In a homogeneous solid with itinerant charge carriers, κ_e can be computed using the electrical conductivity (σ) and Lorenz number (L) through the Wiedemann-Franz law $\kappa_e = L\sigma T$. For a metal, the Lorenz number assumes the Sommerfeld value of $L = 2.44 \times 10^{-8}\ \mathrm{V}^2/\mathrm{K}^2$. It varies depending on the electronic band structure,[17] but rarely more than 30%. One must be careful when the homogeneous solid approximation fails due to the presence of electrical resistance at grain boundaries.[18] In this case, κ_e is expected to be underestimated, leading to an overestimation of κ_{vib}. In materials where charge carriers do not behave as nearly free electron quasi-particles, such as VO_2[19,20] and semi-conducting polymers,[21] the applicability of the Wiedemann-Franz law is debated and values of an effective Lorenz number can be far from the Sommerfeld value of L.

This review will focus on the heat carried by atomic vibrations κ_{vib}. κ is dominated by κ_{vib} in solids at the upper (e.g., diamond) and lower (e.g., glass) limits of thermal conductivity, and also contributes appreciably to many technological materials in between (e.g., semiconductors).

The 3×3 thermal conductivity tensor, κ^{ij}, is defined for a homogeneous solid through Fourier's law as

$$j^i = -\kappa^{ij}\, \nabla^j T, \tag{2}$$

which is depicted in Fig. 1(a). j^i is the thermal energy flux vector, and $\nabla^j T$ is the gradient of the absolute temperature. κ^{ij} can be represented by a scalar in isotropic materials and materials that exhibit cubic symmetry; it is therefore common to omit the tensor superscripts. In non-cubic materials, particularly layered compounds with van der Waals bonding, thermal anisotropy can be quite high. In this review κ implies κ^{xx}.

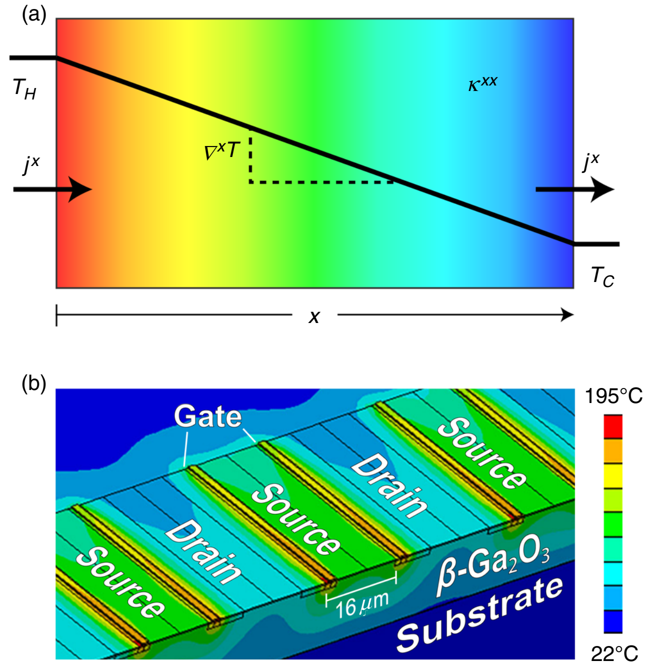

FIG. 1. (a) An illustration of a homogeneous solid in which thermal energy is flowing. A source has injected heat on the left side, and on the right side there exists a sufficiently large heat sink. When a steady state is reached, j^i is a constant in space and time, and a thermal gradient $\nabla^i T$ has been established. For a given $\nabla^i T$, the magnitude of the heat current j^i is set by the material thermal conductivity κ^{ij} through Fourier's law, Eq. (2). (b) Finite element model of a multi-fingered β-Ga_2O_3 transistor demonstrating the dramatic hot spots that can occur in power electronics and the heterogeneous nature of heat transfer when applied to technology. Reproduced from Yuan *et al.*, J. Appl. Phys. **127**, 154502 (2020),[22] with permission of AIP Publishing.

A. Wave-packets

When building an understanding of thermal transport, it is important to distinguish the concepts that emerge from wave-packet physics, specifically the relaxation time (τ), wavelength (λ), mean free path (Λ), and coherence length. In the context of vibrational thermal conductivity, wave packets are supported by the atoms bonded together in the solid. Atomic bonding is typically described by a spring mass model (Appendix A). While it is not always obvious, many aspects of transport theories rely on the concepts of wave-packets. Therefore, it is beneficial to review basic concepts, which are shown schematically in both reciprocal space [Fig. 2(a)] and in real space [Figs. 2(b) and 2(c)].

The solid black line in Fig. 2(a) represents the frequency (ω) or energy ($\hbar\omega$) of harmonic vibrational states at different wave-vectors ($\mathbf{q}$). This $\omega(\mathbf{q})$ relationship is commonly referred to as a dispersion relation, and the individual states (labeled by the black dot) are referred to as plane-wave eigenstates. Details on how one obtains $\omega(\mathbf{q})$ from interatomic force constants[12] are given in Appendix A 1. The harmonic vibrational state (eigenstate) refers to the mode energy (eigenvalue) and mode polarization (eigenvector). A collection of these plane-wave eigenstates (spanning $\Delta\mathbf{q}$ about $\mathbf{q}$) linearly combine to form a wave-packet [Fig. 2(b)]. In this way, plane-wave eigenstates that have an infinite spatial extent are used to describe quasi-particle wave-packets that have a finite spatial extent. This wave-packet has classically been referred to as a phonon. However, the phonon can be defined more generally as a harmonic vibration regardless of character, as discussed in Sec. II C. The spatial extent over which atomic vibrations are correlated is termed the coherence length, not to be confused with the mean free path or wavelength. Coherence length considerations are critically important when exploring phononic properties of materials and meta-materials.[23] Latour and Chalopin[24] provide a nice discussion regarding coherence length, where they distinguish the "spatial" coherence length (simply called the coherence length here) and the "temporal" coherence length (i.e., the mean free path $\Lambda = \mathbf{v}_g\tau$ stemming from the relaxation time τ). The speed at which the wave packet travels is its group velocity and is simply the slope of the dispersion relation ($\mathbf{v}_g = d\omega/d\mathbf{q}$) at $\mathbf{q}$.

When perturbations are considered (e.g., anharmonicity of the interatomic potential or crystal defects), there is a broadening of this dispersion relation. The broadening in energy is inversely proportional to the phonon lifetime and relaxation time (τ). This is depicted in real space Fig. 2(c) as the time the wave-packet may travel before being

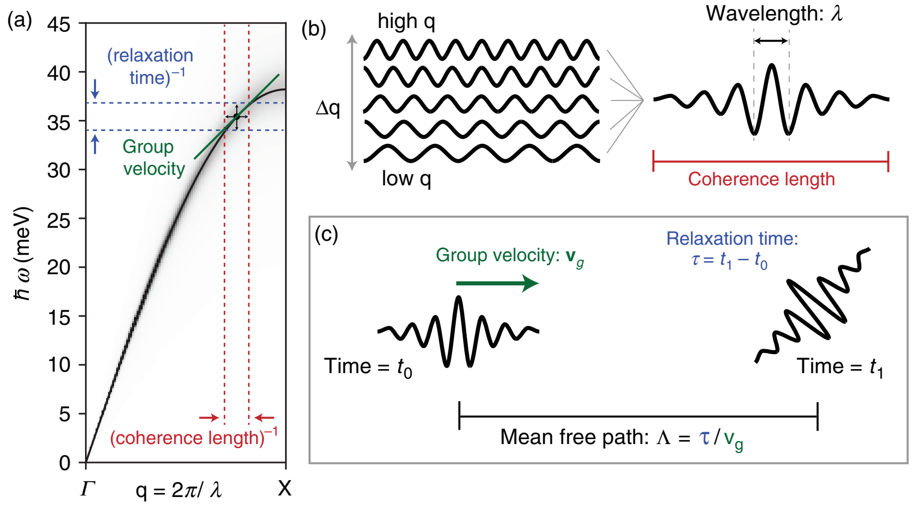

FIG. 2. Schematic diagram defining and differentiating, wavelength, coherence length, mean free path, relaxation time, and group velocity. (a) Harmonic non-interacting vibrational states that together form the phonon dispersion relation are expressed as the black curve. Broadening occurs when perturbations are considered due to phonon-phonon interactions and/or crystal defects. The phonon linewidth along the energy axis is inversely related to the relaxation time. The linewidth along the wave-vector axis is inversely related to the coherence length. (b) The linear combination of a collection of plane-wave states $\Delta\mathbf{q}$ about $\mathbf{q}$ constructs a phonon wave-packet at $\mathbf{q}$. (c) An illustration of the phonon group velocity, relaxation time, and mean free path. The phonon wave-packet could be scattered by other phonons or a defect (not pictured).

scattered by either other phonons or a crystal defect (not pictured). This relaxation time multiplied by the group velocity gives the distance the wave-packet traveled before scattering, or the mean free path (Λ).

The mean free path of a wave-packet will determine how "closely spaced" additional crystal defects will need to be in order to significantly influence its contribution to thermal conductivity. Note that a wide range of mean free paths exist in single material, making the problem inherently multiscale. The wavelength (λ) will determine the "physical size" of defects that will most strongly scatter the wave-packet [Eq. (12)].

B. Molecular dynamics and lattice dynamics

Two of the most common methods for simulating atomic dynamics and vibrational thermal conductivity are molecular dynamics (see recent reviews by DeAngelis *et al.*[11] and Seyf *et al.*[25]) and lattice dynamics (see recent review by McGaughey *et al.*[4]).

Molecular dynamics (MD) is a real space method where the position and velocity of every atom is tracked as a function of time. Thermal transport can be computed directly from this information using Hardy's heat current operator[26] along with the Green-Kubo method [see Eqs. (1) and (2) of DeAngelis *et al.*[11]] Lattice dynamics (LD) is, in a sense, a subset of molecular dynamics that asserts harmonic interatomic forces and periodic boundary conditions allowing a Fourier plane wave decomposition of the atomic motion to be used that completely describes the atomic dynamics. This Fourier decomposition inverts the problem, making lattice dynamics a reciprocal space method. The resulting plane waves (normal modes) can be identified by a wavevector ($\mathbf{q}$), which defines the plane wave direction and wavelength (λ, where $\mathbf{q} = 2\pi/\lambda$). These plane waves are the so-called phonon eigenstates, and each has an associated eigenvector (mode shape) and eigenvalue (energy). These plane waves can transport thermal energy in wave packets (reviewed in Sec. II A). The mechanism of propagating wave packets conducting thermal energy is described by the common phonon-gas model. Since MD computes thermal transport directly from atomic positions and velocities, it is agnostic to the nature in which vibrational energy is transported and to the character of the vibrational modes participating. Traditionally, LD approaches have asserted the phonon-gas model, thereby only capturing the heat carried by propagating phonon wave packets. Recently, generalized, two-channel LD approaches have emerged that capture diffuson channel transport as well, an effect that extends beyond the phonon-gas model. Two-channel LD is discussed further in Sec. II D.

C. Phonon and diffuson taxonomy

The necessity to describe vibrational states that do not exhibit propagating character, yet still conduct thermal energy, has sparked a taxonomy for classifying vibrations based on their character[27] (i.e., propagons, diffusons, locons). Consequently, there has been some debate on the definition of a phonon. DeAngelis *et al.* provide a discussion regarding this topic, which we briefly summarize here.[11] Some consider a phonon as a quasi-particle that must exhibit propagating wave-packet behavior, which consist of attributes that fit into the phonon-gas model. We will refer to this as the "strict" viewpoint. Since it has been shown that, even in the harmonic limit (where the phonon normal mode decomposition is defined), vibrational modes can arise that do not exhibit propagating behavior,[11,27] some authors consider the strict viewpoint to be too stringent. Taking a broader definition, a phonon is simply a quanta of normal mode vibrational energy, regardless of its character. We will refer to this as the "generalized" viewpoint. From the generalized viewpoint propagons and diffusons are not necessarily new quasi-particles, but can be considered types of phonons. A phonon that transports energy as a propagating wave-packet is succinctly denoted a propagon. A phonon that is not propagating but transports its heat diffusely is called a diffuson. A phonon that has its vibrational energy completely localized is a locon.

Additionally, a phonon that crosses below the Ioffe-Regal limit is not considered to be destroyed but, rather, loses its propagating character. This is similar to how electrons that cross below the Ioffe-Regal limit are not considered to be destroyed but can no longer be described as a nearly free electron that travels with a mean free path before scattering. Another benefit of the generalized viewpoint that it is naturally consistent with the observation that the transition from propagating to non-propagating character is a gradual process.[28] Furthermore, localized rattling modes in crystals, as well as interfacial modes, have consistently been considered to be phonons, but they are indeed non-propagating. The generalized viewpoint will be taken in this review.

D. Two-channel lattice dynamics

Lattice dynamics based approaches rely on idealized, non-interacting, harmonic vibrational states as a starting basis for the heat conduction model (Appendix A 1). Using these harmonic states as a basis, vibrational heat conduction can be thought of as occurring through two channels,[15,16,26,29,30] the phonon-gas channel (κ_{pg}) and the diffuson channel (κ_{diff}). These two channels contribute additively to the vibrational thermal conductivity

$$\kappa_{vib} = \kappa_{pg} + \kappa_{diff}. \tag{3}$$

Physical results, meaning a non-infinite κ_{pg} and non-zero κ_{diff}, are only obtained after considering perturbations to these harmonic vibrational states (e.g., phonon-phonon interactions). It's important to recognize that since the magnitudes of κ_{pg} and κ_{diff} are both set by the energy and broadening of the phonon states (Fig. 3), they are not as independent as Eq. (3) makes them seem.

The two channels have fundamentally different temperature dependencies [Fig. 3(c)]. At very low temperatures, κ_{pg} increases with temperature and its magnitude is strongly dependent on sample size and microstructure. κ_{pg} reaches a peak around roughly $\theta_D/3$ (where θ_D is the Debye temperature); however, the temperature and magnitude of the peak strongly depends on scattering from point defects, isotopes, and microstructure. At $T > \theta_D$, $\kappa_{pg} \propto T^{-1}$ when phonon-phonon scattering dominates. κ_{diff} tends to increase with temperature and approach a constant value at high temperature.[31]

The two channels can be understood through the concept of band folding, shown for one dimension in Fig. 3(a).[29] As the size of the unit cell is increased, e.g., by modulating the interatomic force constants, the maximum **q**-vector decreases and more phonon branches can be found at the same **q** point, which is due to the creation of optical modes. As these modes are broadened due to anharmonicity and/or crystal defects, some of them may begin to overlap, making them quasi-degenerate.[16] This is highlighted in red in Fig. 3(a).

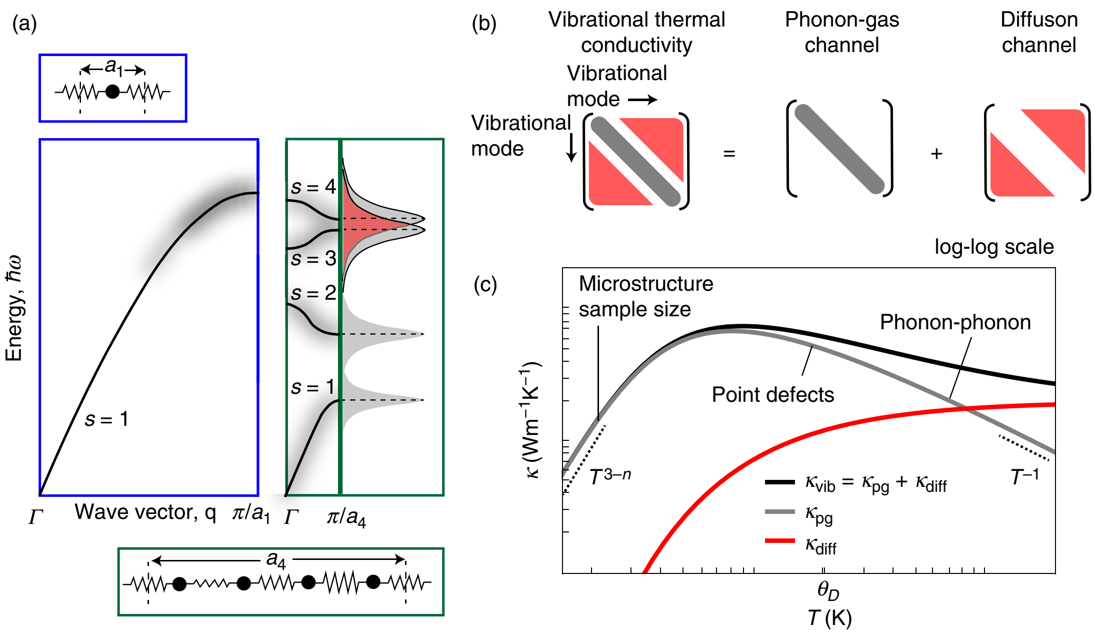

FIG. 3. Vibrational heat conduction through two channels. (a) Understanding of the two channels through the concept of phonon band folding. The vibrational heat conduction of amorphous materials can be studied by considering the limiting case of many atoms per unit cell (i.e., greater than 100). (b) The thermal conductivity can be viewed as a matrix within this framework. The diagonal components are simply the phonon-gas channel. The off-diagonal components describe the diffusion of heat through normal mode mixing and is termed the diffuson channel. (c) Schematic of the temperature dependence of the two channels. Scattering mechanisms are labeled in the region where they most strongly influence the *T*-dependence of κ_{vib}. However, since a wide range of wavelengths and mean free paths contribute to κ_{pg}, microstructure and point effects still influence the magnitude of κ_{pg} at high temperatures even though the temperature dependence is often dominated by phonon-phonon scattering. The *T*-dependence at low temperature is set by the frequency dependence of the micro-structure/boundary scattering rate *n* where $\tau^{-1} \propto \omega^n$, which is influenced by the defect dimensionality. Reproduced with permission from Hanus *et al.*, Mater. Today Phys. **18**, 100344 (2021).[29] Copyright 2021 Elsevier.

The thermal conductivity within the two-channel lattice dynamics framework can be thought of as a square matrix, with rows and columns designating normal modes [Fig. 3(b)]. The diagonal and off-diagonal elements of this matrix have distinctly different physical interpretations. The diagonal components ($s = s'$) give the phonon-gas channel [κ_{pg}, Eq. (B1)], and the off-diagonal components ($s \neq s'$) give the diffuson channel [κ_{diff}, Eq. (56)]. The physical picture of the phonon-gas channel involves propagating wave packets. The physical picture of the diffuson channel involves non-propagating oscillators, which can be defined across many atoms, exchanging energy with each other.

The diffuson channel is, in principle, present in all solids, but tends to become important in amorphous materials,[16,27] crystalline materials that are very anharmonic,[15] and/or structurally complex crystals that have many atoms per unit cell.[29,32] As defects are introduced, it is expected that the phonon-gas channel will be suppressed and the diffuson channel will be promoted due to increasing mode overlap.[11] At the highest temperatures, the diffuson channel is expected to dominate.[31] The transition between κ_{pg}- and κ_{diff}-dominated heat conduction with increasing crystal complexity, anharmonicity, defect concentration, and temperature is an important avenue of ongoing research. The historical paradigm is that the phonon-gas channel is so large in crystals that $\kappa_{vib} \approx \kappa_{pg}$. It is now becoming clear that this approximation is likely not valid for many technologically relevant materials, particularly those with low κ.

E. Ballistic and diffuse transport regimes

It is important not to confuse the diffusive transport regime for the phonon-gas channel with the diffuson channel. Within the diffusive transport regime of the phonon-gas channel, phonon wave packets are still thought to be propagating a length equal to their mean free path at the micro-scale. This is precisely the reason ballistic effects can become important when considering the phonon-gas channel. In contrast, vibrational modes conducting through the diffuson channel do not exhibit propagating character and are not expected to exhibit any ballistic transport effects, no matter how small the length scale considered.

When considering propagating phonons in the phonon-gas channel, one must be mindful of ballistic transport effects. Fourier's law, given in Eq. (2), assumes diffusive transport and predicts that the thermal energy flux (j^i) will continue to increase no matter how large the temperature gradient ($\nabla^j T$) becomes. In reality, a limit exists where all phonon wave packets are traveling ballistically through the sample unperturbed. It can be helpful to consider the analogous, and perhaps more familiar, propagation of light. A photon propagating through clear air unperturbed is traveling ballistically. A photon traveling in hazy air scatters frequently and transports diffusely. Fourier's law describes diffuse propagation. When a phonon's mean free path [defined in Fig. 2(c)] is larger than (or approximately equal to) the characteristic length scale of ∇T, then a ballistic phonon transport regime is entered. When a phonon's mean free path is smaller than the characteristic length scale of ∇T, there is diffusive transport and Fourier's law holds. The importance of ballistic effects depends on the material system and the length and time scale of temperature gradients being considered. When considering experimental error in the measurement of κ_{vib} (commonly 3% via laser flash analysis) and temperature (commonly 5% at a 0.5 μm resolution via thermoreflectance imaging), Fourier's law and the relaxation time approximation tend be sufficient for materials such as Si and GaN (see Fig. 5 of Carrete *et al.*[33]) and the accuracy of these approximations is expected to increase as κ_{vib} of the material decreases.

Open source computational packages such as almaBTE provide tools for examining ballistic transport effects,[33] which can become important in high thermal conductivity materials. The work of Hua and Minnich[34] provides a framework to experimentally probe and simulate the transition between transport regimes based on a frequency dependent Boltzmann transport equation (BTE) approach. Other methods for capturing ballistic effects include the McKelvey-Shockley flux method[35] and phonon hydrodynamics.[36]

In systems with very large thermal gradients, such as power electronics, a model based on Fourier's law may over predict thermal conduction, due to the presence of ballistic effects. For example, Donmezer and Graham showed that spatially localized ($<$1 μm) hot spots in electronic devices reach higher temperatures than is predicted from a model based solely on Fourier's law.[37] However, this effect is expected to be difficult to measure given that the spatial resolution of temperature measurements is commonly $\sim$0.5 μm (e.g., thermoreflectance imaging).

In general, models based on Fourier's law (such as finite element analysis, FEA) are more versatile in terms of system geometry and the different materials that can be considered, but neglect ballistic transport effects. While a mode specific BTE simulation of an entire device remains intractable, FEA models can be modified to artificially capture ballistic effects (e.g., by modifying κ based on various conditions), or by creating a multi-scale transport model. However, the development of these approaches is still an active area of research.

III. PHONONS IN PERFECT CRYSTALS

Before examining how crystalline defects will influence heat conduction by phonons, we first review phonons in perfect crystals. κ_{vib} is often dominated by κ_{pg} in perfect crystals. We refer the reader to the review provided by McGaughey *et al.* for a detailed tutorial of κ_{pg} computed via DFT based lattice dynamics.[4] Here, we focus on aspects that are critical for multi-scale modeling considerations (such as the long-wavelength limit) and for building intuition regarding the influence of defects and disorder.

A. Phonon-gas thermal conductivity

The computation of the phonon-gas channel of perfect crystals via DFT based lattice dynamics, where phonon properties are computed mode-specifically [Eq. (B1)], has become common in the field. However, in systems containing crystal defects (particularly extended defects), which is a main focus of this review, this procedure may become prohibitively difficult or even impossible. In these cases, spectral treatments, where phonon properties are characterized as a function of frequency (ω), may be required. Additionally, a spectral decomposition of a mode specific model may be desired for purposes of multi-scale modeling and/or interpreting results. In Appendix B we provide a spectral decomposition of the mode specific model given in Eq. (B1), resulting in

$$\kappa_{pg} = \frac{1}{3} \int_0^{\omega_{max}} C(\omega)\, v_g(\omega)^2\, \tau(\omega)\, d\omega. \tag{4}$$

The spectral phonon-gas thermal conductivity is then given by $\kappa_{pg}(\omega) = C(\omega)v_g(\omega)^2\tau(\omega)/3$. Alternative to computing $C(\omega)$, $v_g(\omega)$, and $\tau(\omega)$ using mode specific quantities as in Eqs. (B4) and (B5), it is common to define them analytically using semi-empirical expressions for the phonon dispersion relation and relaxation time (Appendix B 3). This procedure is commonly called Callaway-Klemens type modeling and can be useful when interpreting emergent phenomena in the thermal transport of complex, defective systems where a mode resolved treatment [Eq. (B1)] is not warranted, prohibitively difficult, and/or not possible.

Figure 4 shows the spectral decomposition of a mode specific model for Si at 300 K. Harmonic interatomic forces are used to compute the dispersion relation [Fig. 4(a)], heat capacity [Fig. 4(b)], and group velocity [Fig. 4(c)]. Three-phonon scattering, built from anharmonic 3rd order interatomic force constants, broadens the phonon modes in energy [Fig. 4(d)] and thus gives finite relaxation times (Fig. 4). The solid black curves in Figs. 4(b), 4(c) and 4(e) are computed using the spectral decompositions given in Eqs. (B3), (B4), and (B5), respectively. These phonon properties combine to give the spectral thermal conductivity due to the phonon-gas channel (Fig. 4). It can be seen that the majority of the heat is carried by acoustic phonons, below 25 meV, due primarily to their very long relaxation times. While optical phonons indeed have a lower $v_g(\omega)$, they carry much less heat primarily due to their very low τ, due to strong phonon-phonon scattering.

B. The low-ω challenge

Here we take a closer look at the behavior of low-ω phonons in perfect crystals. Understanding the expected behavior of $\kappa_{pg}(\omega)$ as $\omega \to 0$ is particularly important when approximating Brillouin zone integration via **q**-meshing procedures, when implementing multi-scale models, and when considering the impact of microstructure, grain boundaries, interfaces (Sec. V), and dislocation strain fields (Sec. IV). First we review the analytical aspects of the problem and then discuss how the analytical conclusions compare to results obtained using uniform **q**-meshing procedures. Our discussion is constrained to 3D systems. Low-dimensional materials exhibit different ω-dependencies in their density of vibrational states, so conclusions may not directly translate from 3D to 2D or 1D systems.[38]

We start by considering a question that has been debated historically:[39–42] Will a defect-free, infinitely large crystal have infinite thermal conductivity? In such a case, the only phonon scattering mechanism would be scattering with other phonons due to natural anharmonicity of the crystal potential. While this question may seem academic, a conclusive answer would bring with it more accurate predictions of how extended defects such as interfaces will influence the thermal conductivity, which is a topic of technological importance.

One can understand this problem by examining the spectral decomposition of the phonon-gas thermal conductivity [$\kappa_{pg}(\omega)$]. To see where the proposed question arises, we examine the lower bound of the integral over ω. First, we assign $\tau(\omega)$ the general form

$$\tau(\omega) = A(T)\omega^{-n}, \tag{5}$$

which contains a temperature dependent constant $A(T)$ (to be discussed later) and an arbitrary frequency dependence n. As $\omega \to 0$, $v_g(\omega)$ converges to the speed of sound v_S, and the spectral

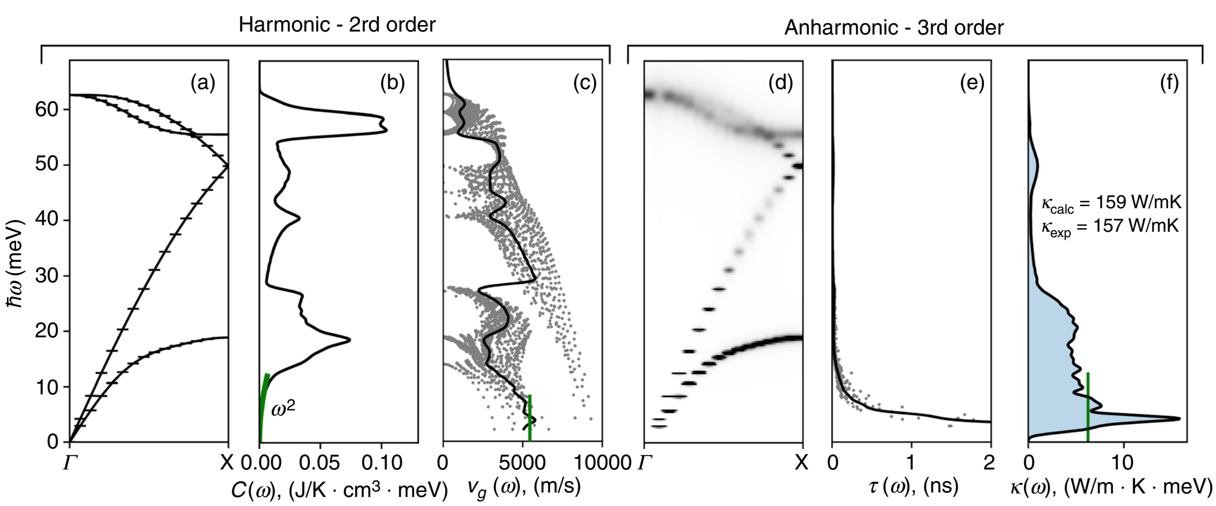

FIG. 4. Phonons and phonon thermal conductivity of perfect, single crystalline Si computed using DFT-based lattice dynamics and the phonon Boltzmann transport equation at 300K. The green lines show analytical expressions that hold at low-ω, and highlight numerical artifacts that can accompany this type of mode specific simulation. (a) The phonon dispersion relation along $\Gamma - X$ calculated from second order interatomic force constants (Appendix A). (b) The spectral heat capacity [Eq. (B3)]. (c) Mode dependent phonon group velocity, $v_s(\mathbf{q})$ (dots) and the isotropic average group velocity at a given frequency $v_g(\omega)$ [curve, Eq. (B4)]. (d) The phonon dispersion relation with phonon line broadening defined by the phonon-phonon scattering relaxation time. The discrete behavior in **q** reflects the resolution of the finite uniform **q**-mesh used, a relatively dense $30 \times 30 \times 30$ mesh. (e) The mode dependent relaxation time due to phonon-phonon scattering $\tau_s(\mathbf{q})$ (dots), and the isotropic average relaxation time at a given frequency $\tau(\omega)$ [curve, Eq. (B5)]. Figure 5 shows a $\tau \propto \omega^{-2}$ fit to this computational data at low-ω. (f) The spectral thermal conductivity computed using the data shown in panels (a), (c), and (e). The peak at 5 meV is artificial and is due to poor sampling of **q**-space below 10 meV. From analytical consideration (green lines), $\kappa(\omega)$ should converge to a constant value as $\omega \to 0$ rather than go to zero.

heat capacity becomes $C(\omega) = 3k_B\omega^2/(2\pi^2 v_S^3)$. Asserting this low-$\omega$ limiting behavior Eq. (4) becomes

$$\kappa_{pg} = \frac{k_B}{2\pi^2}\frac{A(T)}{v_S}\int_0^{\omega_{max}} \omega^{2-n}\, d\omega. \tag{6}$$

From this representation one can easily see that the exponent in the power law dependence of the lifetime, n, is the critical parameter. If phonons exhibit a power law dependence with $n \geq 3$, then κ_{pg} will diverge to infinity (at any temperature) if there are no other phonon scattering mechanisms. Only 3-phonon scattering processes are considered. Other effects contributing to τ can be important at very low frequency (e.g., MHz), such as thermoelastic and Akhieser damping.[43] The phonon spectrum extends up to the THz scale; therefore, in the context of the thermal transport of phonons we only consider 3-phonon processes. Consequently, the power law dependence of the phonon lifetime at low-ω is critical for determining the strength at which extended defects, such as interfaces and dislocations, will reduce κ_{pg}. Early theories predicted phonon lifetimes at low ω would exhibit $n = 4$; therefore, several theories have indeed predicted that the thermal conductivity would diverge to infinity if the material was infinitely large and defect free.[42] There are several consequences of phonons exhibiting $n \geq 3$. First, the thermal conductivity of very clean crystals would continue to increase as crystal size increases. Second, the thermal conductivity determined computationally would not converge with increasing **q**-mesh density. It seems that these attributes are not typically observed, suggesting that in most cases $n < 3$.

Figure 5 shows the lifetimes from Fig. 4(e) on a log-log scale. The lines show a $\tau \propto \omega^{-2}$ dependence, showing that in Si, phonons below 10 meV show an $n \approx 2$ phonon-phonon scattering power law dependence. This example agrees with the results presented by Ward and Broido, and the reader is referred to their work for more discussion on low-ω behavior of τ in Si and Ge.[44] We examine results within the relaxation time approximation that do not distinguish between Umklapp and Normal processes. As Maznev and Wright pointed out, since no rigid line can be drawn between Umklapp and Normal processes, distinguishing them in a model can create difficulties.[45] In this review, the term "phonon-phonon scattering" embodies both Umklapp and Normal processes.

By recognizing the low-ω frequency dependence of $C(\omega) \propto \omega^2$, $v(\omega) = v_S$, and $\tau(\omega) \propto \omega^{-2}$, we expect $\kappa_{pg}(\omega)$ to approach a constant value as $\omega \to 0$ [green line in Fig. 4(f)] and not go to zero (black line). If $2 < n < 3$ then $\kappa(\omega)$ increases as ω decreases, but the integration converges.

Computing measurable properties such as heat capacity, diffusivity, and thermal conductivity requires integration of the Brillouin zone. Standard **q**-meshing procedures used to approximate this integration can lead to misinterpretation of the importance of low-ω acoustic phonons, seeming to predict $\lim_{\omega\to 0}\kappa_{pg}(\omega) = 0$ rather than $\lim_{\omega\to 0}\kappa_{pg}(\omega) = \text{constant}$ (as expected analytically).

The computational results in Fig. 4(f) make it seem as if phonons below $\sim$2 meV do not carry heat. This conclusion may even seem intuitive since there are very few phonon modes at this low energy; i.e., the pDOS and $C(\omega)$ go to 0 as $\omega \to 0$. However, this attribute is simply an artifact of the uniform **q**-meshing procedure and, through the analytical considerations discussed herein, low-ω phonons are indeed important for thermal conductivity.

To reiterate this important point, we define the amount of heat carried by phonons within a small band of frequencies $d\omega$ centered around ω as $\kappa_{pg}(\omega)\, d\omega$. When $\tau(\omega) \propto \omega^{-n}$ with $n = 2$, $\kappa_{pg}(\omega)$ is expected to approach a constant value as $\omega \to 0$. In this case, phonons approaching the Γ-point ($\hbar\omega < 1$ meV) carry as much heat as phonons at higher frequencies (10 s of meV). If $n > 2$, these low-ω phonons are expected to be even more important.

1. Accumulation curves and q-meshing

The analysis shown in Fig. 4(f) highlights that it is important to ensure that the spectral thermal conductivity $\kappa_{pg}(\omega)$ is converged with

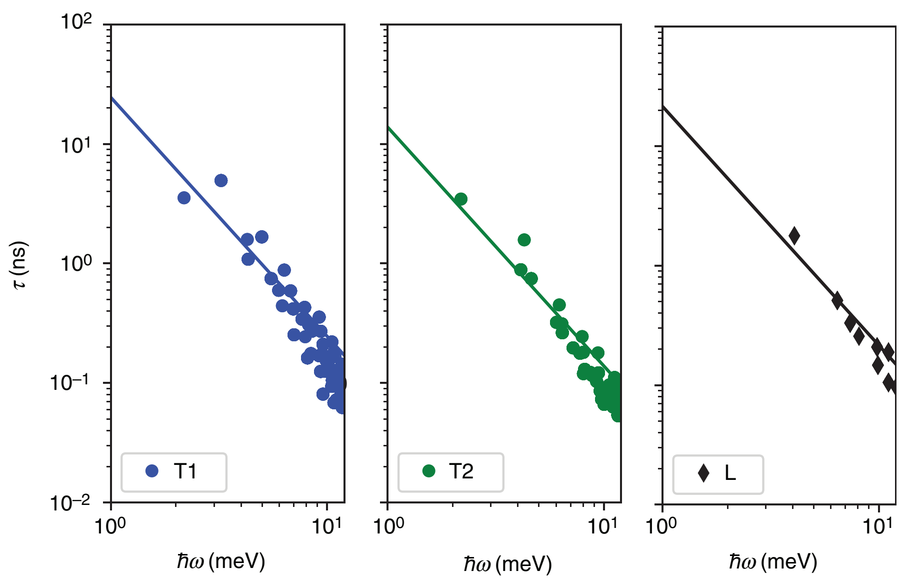

FIG. 5. The low frequency limit of phonon-phonon relaxation time in Si at 300 K [re-plotted from Fig. 4(e)]. The lines indicate a $\tau \propto \omega^{-2}$ frequency dependence. T1 and T2 indicate the two transverse polarizations and L indicates the longitudinal polarization.

respect to **q**-mesh density, in addition to its integrated value (κ_{pg}), especially when phonon properties near the Γ-point are important. Figure 6 demonstrates that while the magnitude of κ_{pg} can approach convergence, the low-ω, long wavelength properties can still be significantly changing with mesh size. This is reflected in the shifting peak in $\kappa_{pg}(\omega)$ with increasing mesh density in Fig. 6(b).

It is often instructive to examine computational results using accumulation curves. The frequency accumulation of κ_{pg} is given by

$$\kappa_{acc}(\omega) = \int_0^\omega \kappa_{pg}(\omega')\, d\omega'. \tag{7}$$

The common mean free path accumulation is presented well by Yang and Dames [see Eqs. (2)–(5) of Ref. 46]. The low-ω form of $\kappa_{pg}(\omega)$ can be obtained from Eq. (6) with $n=2$ as $\kappa_{pg}(\omega) = k_B A(T)/(2\pi^2 v_S)$. From this we have an analytical form of $\kappa_{acc}(\omega)$ at low-ω,

$$\kappa_{acc}(\omega) = \frac{k_B A(T)}{2\pi^2 v_S}\omega. \tag{8}$$

Figure 6(c) shows κ_{acc} for Si using Gaussian quadrature in Cartesian coordinates for the **q**-mesh sampling compared with a **q**-mesh with similar number of sampled points but in spherical coordinates, which allows for better sampling at long wavelengths. Increasing the mesh density, in order to sample longer wavelengths, scales as N^3 for a uniform mesh; whereas it scales as N for a spherical mesh. The green line shows a linear fit based on Eq. (8) where the slope essentially gives $A(T)$. The poor long wavelength sampling is reflected in the sharp steps seen in the red line. While the magnitude of κ_{pg} has converged and agrees between the uniform and spherical **q**-mesh, the spectral properties at low-ω and long wavelength are represented differently.

Extended crystal defects, such as dislocations and interfaces, are known to influence low-frequency, long-wavelength phonons, as we discuss in Sec. IV. Therefore, **q**-meshing techniques that sample near

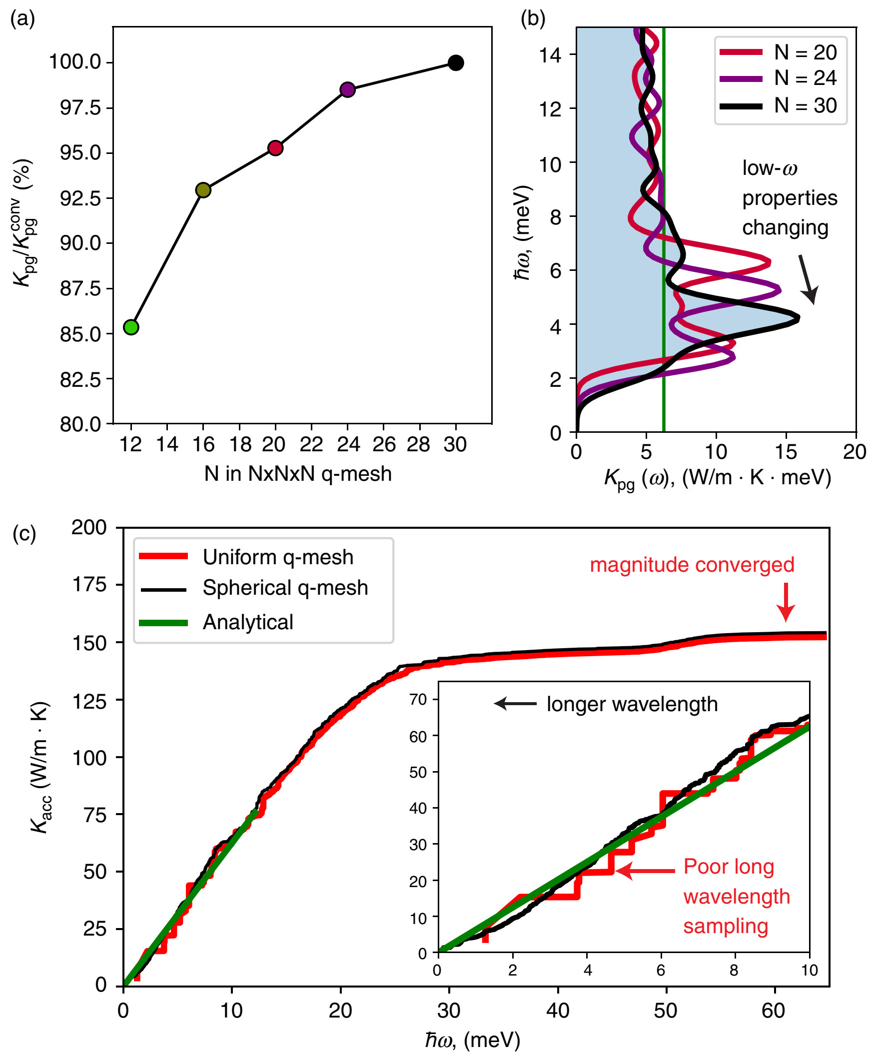

FIG. 6. Examination of **q**-meshing techniques and the resulting spectral representation of κ_{pg}. (a) κ_{pg} with increasing uniform **q**-mesh density. (b) The spectral thermal conductivity changes significantly with increasing N, while the magnitude is approaching convergence. (c) The ω-accumulation curve computed using Gaussian quadrature in Cartesian coordinates (uniform) for the **q**-mesh sampling, and using a spherical **q**-mesh with similar number of sampled points. The discrete steps in the uniform mesh show how even at very high mesh densities, the long wavelength behavior is still sampled relatively poorly.

Γ-point phonons will likely be critical when building *ab initio* based multi-scale models.

2. Lifetimes of low-ω phonons in GaN

Low-ω phonon lifetimes have been measured in GaN,[47,48] which provides an important experimental comparison with the computational and analytical considerations previously discussed in Sec. III B. These measurements utilize the attenuation of sub-THz and THz longitudinal acoustic waves to directly measure the intrinsic phonon relaxation times due to phonon-phonon interactions. Alternatively, phonon lifetimes can be extracted from the linewidths of inelastic x-ray and neutron scattering experiments.[48–51] However, low-frequency data is usually buried in the elastic scattering (diffraction) peaks and the accuracy of the extracted lifetimes can be limited by instrument resolution.

Figure 7 shows experimental lifetimes of longitudinal acoustic phonons from Liu *et al.*[47] (green squares) and Chou *et al.*[48] (blue squares), compared to DFT-based simulations[48] (orange circles) and an analytical model with a form provided by Slack[52] (black line),

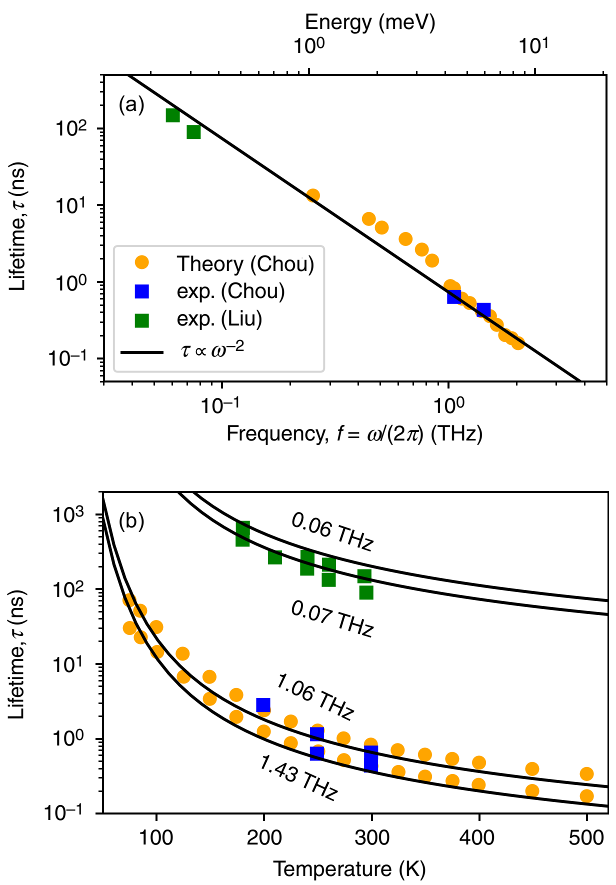

FIG. 7. Intrinsic phonon-phonon scattering lifetimes of longitudinal acoustic phonons in GaN propagating along the c-axis. The data points shown are reported by Liu *et al.*, Appl. Phys. Lett. **90**, 041902 (2007)[47] and Chou *et al.*[48] The solid black lines in panel (a) and (b) are an analytical model given in Eq. (9). (a) Lifetimes vs frequency at 300 K. (b) Lifetimes vs temperature at various frequencies.

$$\tau(\omega)^{-1} = C_1 T \omega^2 e^{-\frac{C_2}{T}}, \tag{9}$$

with $C_1 = 3.8 \times 10^{-19}$ s K^{-1} and $C_2 = 360$ K. Similar to the computational results for Si above 2 meV (Fig. 5), a $\tau \propto \omega^{-n}$ with $n \approx 2$ is observed. This is also in agreement with the theory provided by Herring,[42] which predicts $n = 2$ for materials in the C_{6v} (wurtzite) symmetry. The form of Eq. (9) is equivalent to Eq. (5) with $n = 2$ and $A(T) = (C_1 T e^{-C_2/T})^{-1}$.

Rather than extracting the coefficients C_1 and C_2 from attenuation data (which is limited in the literature) or simulation, as they were in Fig. 7, they may be computed via material properties. The exponential term increases with decreasing temperature and is meant to capture the increased proportion of momentum conserving phonon-phonon scattering processes (Normal) to momentum non-conserving (Umklapp) processes, resulting in decreased thermal resistance from phonon-phonon scattering. As such, $C_2 = \theta_D/3$ was proposed by Slack.[52] When $T > \theta_D/3$ then $\tau \propto T^{-1}$ is commonly observed and derives from the population of scattering phonons, which increases linearly with temperature when $T > \theta_D$. Therefore, the scattering probability and resulting scattering rates increase linearly with temperature, resulting in the $\kappa \propto T^{-1}$ high temperature behavior, which is characteristic of the phonon-gas channel. Several forms of the coefficient C_1 have been proposed.[52–54] The form given in Eq. (B19), is equivalent to Eq. (9) at $T > C_2$, with $C_1 = (V_{at}/(6\pi^2))^{1/3} (2k_B\gamma^2/(\bar{M} v_g v_p^2))$, where γ is the Grüneissen parameter [Eq. (26)], v_g is the group velocity, v_p is the phase velocity, $\bar{M}$ is the average atomic mass, and V_{at} is the volume per atom. C_1 is meant to capture both the phase space for phonon-phonon scattering and the phonon-phonon coupling strength.

Using Eq. (9) for τ, considering the limit as $\omega \to 0$ (Γ point) and using a longitudinal speed of sound of 7700 m/s, then the amount of heat carried below $f = 1.43$ THz (∼6 meV), which is 6% of the maximum phonon frequency in GaN, is approximately 8 Wm^{-1}K^{-1} at 300 K. DFT-based κ_{pg} simulations, which accurately represent the phonon lifetimes and magnitude of the overall thermal conductivity, show that the total amount of heat carried by longitudinal phonons in GaN at 300 K is 43 Wm^{-1}K^{-1}. Therefore, we conclude that approximately 19% of the total heat carried by longitudinal acoustic phonons is carried by phonons below 6 meV. These same phonons account for only ∼0.5% of the longitudinal acoustic branch pDOS (assuming a ω^2 pDOS and max LA frequency of 35 meV). This analysis indicates that low-ω phonons in GaN may be even more important than was estimated by Chou *et al.* using a power-law dependence of $n = 1.34$ [extracted from two experimental data points given by blue squares in Fig. 7(a)].[48]

IV. PHONONS IN DEFECTIVE CRYSTALS

Having reviewed heat conduction through the phonon-gas channel (κ_{pg}) in perfect crystals, we look at the influence of defects. We attempt to build physical intuition that can guide technologically relevant thermal design strategies using materials chemistry, nano/microstructure, and synthesis and fabrication procedures, as well as aid in the analysis of computational simulations. The foundational analytical treatment reviewed here illustrates behaviors expected from "first order" physics. Deviations from these analytical expectations may reveal novel physical behaviors, which may be observed experimentally or computationally. Furthermore, an understanding of analytical theories can be used to identify practical limitations of simulation methods where far-field effects can be difficult to capture.

Two fundamentally different mechanisms through which defects influence the vibrational thermal conductivity are phonon scattering and lattice softening. While these mechanisms influence both the phonon-gas and diffuson channels, we first focus on their impact on the phonon-gas channel, which to date has been more extensively studied. Both are illustrated in Fig. 8.

Within the phonon scattering picture, a defect is viewed as introducing a scattering potential $V(\mathbf{r})$, which can be used to compute a defect scattering probability ($W_{\mathbf{qq}'}$) and relaxation time due to particular defect type (τ_i, here i is a defect label). The influence of this defect scattering mechanism on the vibrational thermal conductivity is commonly incorporated with other scattering mechanisms via Mathiessen's rule, which combines the variety of potential scattering terms to define a total relaxation time

$$\tau^{-1} = \sum_i \tau_i^{-1}. \qquad (10)$$

Phonon-defect scattering broadens phonon linewidths beyond intrinsic linewidths due to phonon-phonon scattering [Figs. 8(b) and 8(c)]. The average phonon energies and interatomic forces in the solid are assumed to remain constant. Therefore, the elastic moduli, mode specific heats, and speeds of sound are also assumed unchanged.

Elastic softening (also referred to as lattice softening) refers to the mechanism by which defects modify the average elastic moduli, speeds of sound, and energy of the phonons in a material—as illustrated in Fig. 8. Since, elastic softening alters the phonon dispersion, the maximum acoustic phonon frequency ω_{max}, heat capacity $C(\omega)$, and phonon propagation (group) velocities v_g are also changed. Additionally, the intrinsic phonon-phonon scattering is modified since the phase space for scattering depends critically on the phonon density of states (pDOS), or more specifically the joint density of states [see Eqs. (20)–(24) of Togo *et al.*[12]).

Figures 8(b)–8(d) represent these effects in reciprocal space. Figure 8(a) schematically represents this in real space. The phonon scattering picture shows the phonon changing propagation direction while its frequency is unchanged. The lattice softening picture shows a decrease in phonon frequency and propagation speed. In Secs. IV A and IA B, we will examine the theoretical and experimental implications of these two distinct mechanisms.

A. Defect scattering

Defects in an otherwise perfect crystal perturb the phonon Hamiltonian, H [given in Eq. (A5)]. If this perturbation varies in space and/or time, it can induce phonon scattering. In this section, we discuss the effects of spatially varying perturbations by considering defect-induced scattering potentials, $V(\mathbf{r})$, and resulting phonon scattering processes computed in the context of Fermi's Golden Rule perturbation theory (i.e., in the Born approximation). We consider only elastic interactions, meaning the incident and outgoing phonons conserve energy.

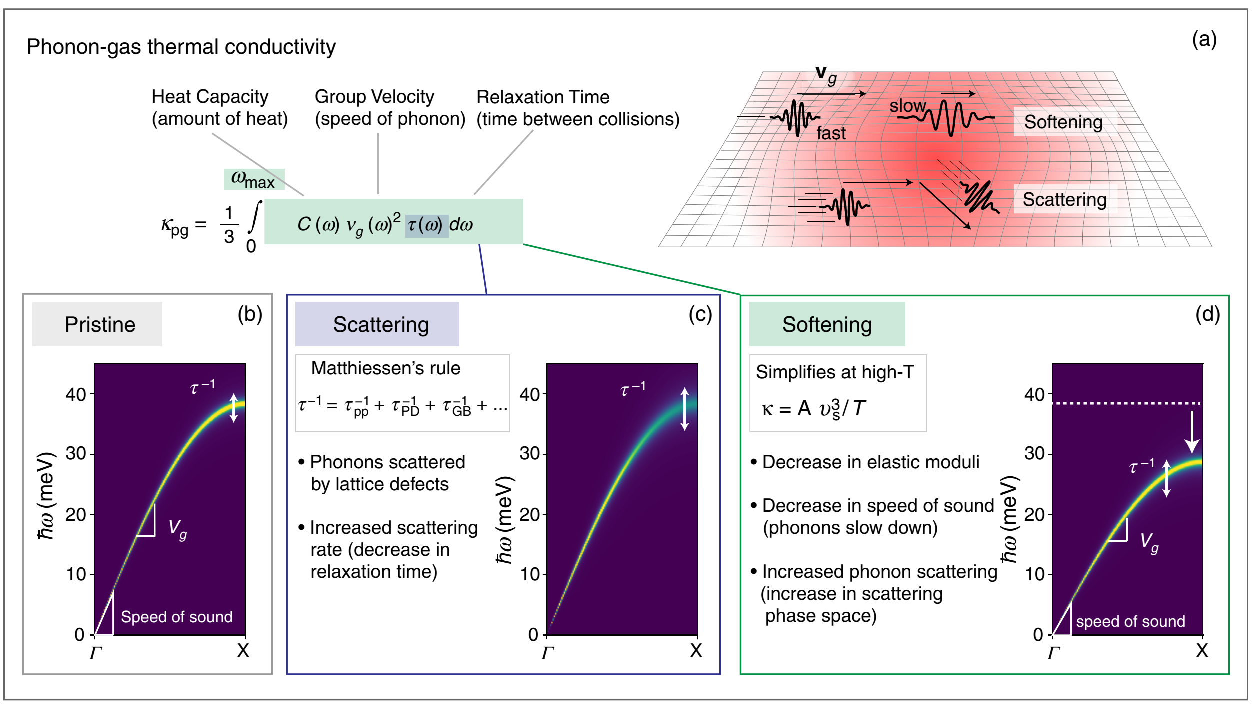

FIG. 8. Schematic representations of phonon scattering and lattice softening. (a) A real space depiction of phonon scattering and lattice softening. (b) Phonon dispersion and linewidths of a pristine crystal. (c) Phonon scattering due to defects. (d) Lattice softening and reduced elastic moduli and speed of sound due to defects. Reproduced with permission from Hanus *et al.*, Adv. Mater. **31**, 1900108 (2019).[95] Copyright 2019 Wiley.

1. Effect of defect dimensionality

We start by considering the relationship of the scattering defect dimensionality with the ω-dependence of the phonon lifetime. In doing so, we will find a deeper understanding of specular (the conservation of momentum in one or more directions) vs diffuse scattering. We attempt to capture first order physics and, therefore, make several approximations to achieve closed form expressions that help establish physical intuition. Specifically, we make the isotropic dispersion approximation and do not consider mode conversion (and therefore suppress the branch index, s). The conclusions made regarding defect dimensionality, specularity, phase space, and ω-dependence are expected to hold when these approximations are removed.

We follow the basic precepts of phonon scattering theory and its contribution to lattice thermal conductivity as laid out, for example, by Ziman.[55] By applying these precepts to elastic scattering from a defect with scattering potential $V(\mathbf{r})$ (described in detail in Appendix D), the scattering rate or inverse relaxation time ($\tau(\mathbf{q})^{-1}$) of a phonon with wavevector $\mathbf{q}$ and frequency $\omega(\mathbf{q})$ may be written as a product of three factors,

$$\tau(\mathbf{q})^{-1} = n_{\bar{n}\mathrm{d}}\, g_{\bar{n}\mathrm{d}}(\omega)\, \overline{|M_{\bar{n}\mathrm{d}}|^2}. \tag{11}$$

The three factors n, g, and $\overline{|M|^2}$ are, respectively, the spatial density of the defects in the crystal, the phonon density of states (pDOS), and a term containing the squared magnitude of a scattering matrix element [Eq. (6.4.4) of Ziman[55]],

$$\langle \mathbf{q}'|H'|\mathbf{q}\rangle = (L_x L_y L_z)^{-1} \int d^3\mathbf{r}\, V(\mathbf{r}) e^{-i\mathbf{Q}\cdot\mathbf{r}}, \tag{12}$$

where $V(\mathbf{r})$ is the scattering potential and $L_x L_y L_z$ is the volume of the crystal containing the defect. It can be seen in Eq. (12) that the matrix element can be thought of as the Fourier transform of the scattering potential $V(\mathbf{r})$, into a scattering vector space, $\mathbf{Q} = \mathbf{q}' - \mathbf{q}$. Note, that $\mathbf{Q} \propto 1/\lambda$, so a phonon wave-packet will be more strongly coupled to defects that are similar in size to its wavelength, as mentioned in Sec. II A. The bar in $|M|^2$ indicates that the magnitude of the matrix element squared has been weighted by the forward scattering parameter (which states that a $\mathbf{q} = \mathbf{q}'$ transition does not contribute to the scattering rate) and summed over possible final states $\mathbf{q}'$. The essential point, indicated by the subscript $\bar{n}\mathrm{d}$, is that all three factors depend on $\bar{n}$, the codimension of the defect. That is,

$$\bar{n} = 3 - d_\mathrm{d} \tag{13}$$

with d_d being the dimensionality of the defect. Thus, for a one-dimensional defect such as a dislocation line, $d_\mathrm{d} = 1$ and $\bar{n} = 2$, for a point defect $d_\mathrm{d} = 0$ and $\bar{n} = 3$, and so on.

We can understand Eq. (11) as follows. Consider a line defect ($\bar{n} = 2$) parallel to the z axis. In addition to the energy, the z component of the phonon wavevector must be conserved when scattering with this defect. In this case, "specular scattering" occurs in the z-direction, which results in the phonon scattering onto a circle in $\mathbf{q}$-space, and when summing over all possible final state wavevectors the density of accessible phonon states is effectively that of a system with two real spatial dimensions, written as $g_{2\mathrm{d}}$. At the same time, the matrix element of the perturbation reduces to an integral over the coordinates perpendicular to the defect, x and y, and since this is now a two-dimensional integral, we write it as $M_{2\mathrm{d}}$. Finally, the density of line defects $n_{2\mathrm{d}}$ is an areal density, or a number per unit area with dimensions $(length)^{-2}$.

The same reasoning applies to planar ($\bar{n} = 1$) and point ($\bar{n} = 3$) defects. All three cases are illustrated in Fig. 9 where the scattering diagram is shown on top (analogous to an Ewald sphere) and the corresponding density of final states, $g_{\bar{n}\mathrm{d}}$, is given on the bottom, which for acoustic phonons obeys the following relation:

$$g_{\bar{n}\mathrm{d}} \propto \omega^{\bar{n}-1}. \tag{14}$$

A phonon interacting with a point defect scatters onto a shell in $\mathbf{q}$-space, a phonon interacting with a line defect scatters onto a circle, and one interacting with a planar defect scatters onto two states (forward and backward scattering) on a line in $\mathbf{q}$-space.

The objective here in writing the rate as a product of $n_{\bar{n}\mathrm{d}}$, $g_{\bar{n}\mathrm{d}}$, and $\overline{|M_{\bar{n}\mathrm{d}}|^2}$ is to highlight aspects of scattering problems that are most important for practical purposes. It is useful to refer to the quantities $g_{\bar{n}\mathrm{d}}$ and $\overline{|M_{\bar{n}\mathrm{d}}|^2}$ as the "phase-space" and "matrix-element" contributions, respectively. It may also be useful to examine Eq. (11) by simple dimensional analysis. Denoting the dimensions of any quantity X by $[X]$, we have

$$[n_{\bar{n}\mathrm{d}}] = \frac{1}{(length)^{\bar{n}}}; \quad [g_{\bar{n}\mathrm{d}}] = \frac{time}{(length)^{\bar{n}}}; \quad \left[\overline{|M_{\bar{n}\mathrm{d}}|^2}\right] = \frac{(length)^{2\bar{n}}}{(time)^2}; \tag{15}$$

and $\tau(\mathbf{q})^{-1}$ correctly has dimensions of $(time)^{-1}$. It is important to note that, while the isotropic approximation is implied in Fig. 9, where a constant energy surface is represented as the shell of perfect sphere (no bumps or dimples), these dimensionality and phase space arguments hold even when anisotropy in the phonon dispersion is considered.

2. Mass contrast scattering

Now that we have established the kinematic and phase space effects that arise from considering a scattering potential's dimensionality, we consider the nature of the scattering potential itself. It is instructive to first consider the effect of a change in atomic mass. By examining the two terms in H [Eq. (A1)], it can be seen that a change in mass will perturb the phonon states through the lattice kinetic energy, T [Eq. (A2)]. Within the formalism provided in Appendix D, the scattering potential due to a change in atomic mass at point $\mathbf{r}$ in a crystal is

$$V(\mathbf{r}, \omega) = \frac{1}{2}\left(\frac{\Delta M}{M}\right) \hbar\omega\, V_0 \delta(\mathbf{r}). \tag{16}$$

This describes the scattering potential due to mass difference of a point defect or isotope, and is shown graphically in Fig. 9(a). $\delta(\mathbf{r})$ is the three-dimensional δ-function, and V_0 is the volume that the mass fluctuation occupies. Recall that $\delta(\mathbf{r})$ has units of $1/(volume)$, so the quantity $V_0\delta(\mathbf{r})$ is unitless. V, therefore, has the correct units of energy. Care must be taken to ensure that V_0 and the mass fluctuation parameter $\Delta M/M$ are defined consistently. A consistent method that translates well to multiatomic unit cells[56] is to define V_0 as the average

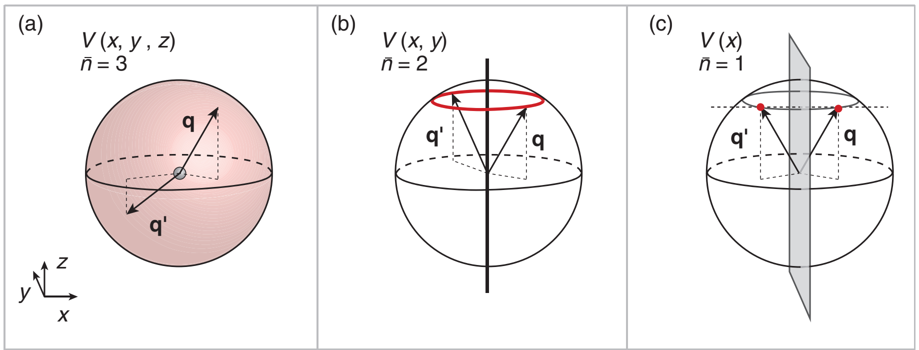

	(a)	(b)	(c)
Conserved quantities:	E	E, q_z	E, q_z, q_y
Phase space:	$g_{3d} = \frac{\omega^2}{2\pi^2 v_g v_P^2}$	$g_{2d} = \frac{\omega}{2\pi v_g v_P}$	$g_{1d} = \frac{1}{\pi v_g}$

Mass difference scattering potential

	(a)	(b)	(c)
Matrix element:	$\overline{\lvert M_{3d}\rvert^2} \propto \left(\frac{\Delta M}{M}\right)^2 \omega^2$	$\overline{\lvert M_{2d}\rvert^2} \propto \left(\frac{\Delta M}{M}\right)^2 \omega^2$	$\overline{\lvert M_{1d}\rvert^2} \propto \left(\frac{\Delta M}{M}\right)^2 \omega^2$
Scattering rate:	$\tau^{-1} \propto \omega^4$	$\tau^{-1} \propto \omega^3$	$\tau^{-1} \propto \omega^2$

FIG. 9. Phonon scattering diagrams for defects with different dimensionalities, with the available phase space indicated in red. (a) A phonon scattered elastically by a point defect scatters into the 3d phonon density of states (pDOS). (b) A phonon scattered by a linear defect [scattering potential, $V(x, y)$] conserves phonon momentum in the z-direction and thus scatters into the 2d pDOS, contributing ω to the phonon scattering rate. (c) A phonon scattered by planar defect [$V(x)$] conserves phonon momentum within the defect plane (yz-plane) and scatters into the 1d pDOS, which is ω-independent. v_g and v_p are the phonon group and phase velocities. The bottom panel shows this dimensionality argument for the ω power law applied to the scattering rate due to mass fluctuation scattering.

atomic volume, and $\Delta M = M_{\mathrm{def}} - \overline{M_s}$, where M_{def} is the mass of the defect species occupying a site on the s sublattice and $\overline{M_s}$ is the average mass of all atoms on that sublattice. In a multiatomic lattice, a final stoichiometric average over all sublattices must be performed on the matrix element, such that the scattering rate is proportional to the average atomic mass variance of the full crystal.[56,57] In the denominator, M is then the average mass of all atoms in the crystal.

Off-stoichiometric defects, such as vacancies and interstitial atoms, have a uniquely large scattering strength because the addition or removal of bonds at the defect site produces a large potential energy perturbation. A simple model developed by Ratsifaritana and Klemens invokes the virial theorem to relate the potential energy perturbation to the average atomic mass in the lattice (M).[58,59] In this case, $\Delta M = M_{\mathrm{def}} + 2M$, where M_{def} is the missing/added mass at the vacancy/interstitial defect. As a result, these off-stoichiometric defects have about 3 times the scattering strength of a simple, substitutional mass defect.[56]

The Fourier transform of Eq. (16) is trivial given the presence of $\delta(\mathbf{r})$, and with Eq. (D24) we can define the matrix element contribution to τ^{-1} as

$$\overline{|M_{3\mathrm{d}}|^2} = \frac{V_0^2 \pi}{2} \left(\frac{\Delta M}{M}\right)^2 \omega^2. \tag{17}$$

This, combined with the phase space contribution $g_{3\mathrm{d}} \propto \omega^2$, gives the familiar $\tau^{-1} \propto \omega^4$ dependence that is often referred to as Rayleigh scattering. The resulting expression [using Eqs. (D23), (17), and (D25)] is

$$\tau(\omega)^{-1} = \frac{n_{3\mathrm{d}} V_0^2}{4\pi v_{\mathrm{g}} v_{\mathrm{p}}^2} \left(\frac{\Delta M}{M}\right)^2 \omega^4. \tag{18}$$

When the Debye approximation is asserted, Eq. (18) is identical to the formula provided by Klemens,[60] and the analytical expression provided by Tamura [Eq. (23) of Ref. 61].

Now suppose the mass fluctuation is arranged as a line through the crystal at $x = y = 0$ [Fig. 9(b)] rather than localized at a point. For example, Klemens proposed that the dislocation core could be modeled as a line of vacancy defects. For such a case, we can define the mass scattering potential

$$V(x, y, \omega) = \frac{1}{2} \left(\frac{\Delta M}{M}\right) \hbar\omega A_0 \delta(x)\delta(y). \tag{19}$$

A_0 is the cross-sectional area the line defect occupies. Recognizing that the minimum Burgers vector is one primitive unit cell vector, one can define $A_0 = V_{\mathrm{PUC}}^{2/3}$. The matrix element contribution to τ^{-1} for this case is

$$\overline{|M_{2\mathrm{d}}|^2} = \frac{A_0^2 \pi}{2} \left(\frac{\Delta M}{M}\right)^2 \omega^2 \sin(\theta)^2, \tag{20}$$

which along with the phase space contribution, $g_{2\mathrm{d}} \propto \omega$ [Eq. (D14)], gives

$$\tau(\mathbf{q})^{-1} = \frac{n_{2\mathrm{d}} A_0^2}{4 v_{\mathrm{g}} v_{\mathrm{p}}} \left(\frac{\Delta M}{M}\right)^2 \omega^3 \sin(\theta)^2. \tag{21}$$

Note that, here, τ^{-1} depends on the direction of the incident phonon rather than just the frequency, contrary to the case of scattering by an isolated point defect. This equation is equivalent to that given by Klemens except for a numerical factor.[180] Once we choose which component of $\kappa_{\mathrm{ph},ij}$ we are interested in, the appropriate $\tau(\omega)$ for use in Eq. (4) can be defined. If we are interested in the direction perpendicular to the linear defect, then using Eqs. (21) and (B10): $\tau(\omega)^{-1} = (2/3)\tau(\mathbf{q})^{-1}$.

For a planar defect, where the atoms lying on a plane at $x=0$ are a different mass [Fig. 9(c)] in a similar fashion, the scattering potential can be defined as

$$V(x,\omega) = \frac{1}{2}\left(\frac{\Delta M}{M}\right)\hbar\omega\, L_0\delta(x). \tag{22}$$

Similarly, we find $\overline{|M_{1\mathrm{d}}|^2}$ [Eq. (D33)]. This along with $g_{1\mathrm{d}}$, which is independent of frequency [Eq. (D30)], gives

$$\tau(\mathbf{q})^{-1} = \frac{n_{1\mathrm{d}}L_0^2}{2v_{\mathrm{g}}}\left(\frac{\Delta M}{M}\right)^2\omega^2\,\frac{q_x^2}{q^2}. \tag{23}$$

Now for $\kappa_{\mathrm{ph},xx}$ we find $\tau(\omega)^{-1} = (1/3)\tau(\mathbf{q})^{-1}$. Equation (23) has the same form as the expression given by Turk and Klemens [Eq. (19) of Ref. 62], which was derived for platelet-like coherent precipitates.

The treatment described above for mass difference scattering demonstrates how defect dimensionality affects phonon scattering rates. In each case, the matrix elements contribute ω^2 to τ^{-1}. This stems from the fact that the mass fluctuations considered are localized in spatial extent and are therefore well described using δ-functions. This is illustrated and tabulated in the top portion of Fig. 9. When the dimensionality of the defect is changed from a point to a line to a plane, the phase space into which the phonon can scatter is altered. This changes the phase space contribution to τ^{-1}, which follows the expression provided in Eq. (14) and is tabulated in the bottom portion of Fig. 9. These phase space effects hold for all types of phonon-defect scattering. However, we will find in Sec. IV A 4 that when the scattering potential is a more complex function in real space, the matrix element contributions are more interesting.

3. Strain and anharmonicity

Internal strain fields can induce phonon scattering through anharmonicity of interatomic forces. The same dimensionality and phase space effects that were discussed in the context of mass contrast scattering are present in strain scattering. However, since the strain fields tend to have more complex behavior in real space, the matrix element contributions ($M_{\tilde{n}\mathrm{d}}$) to phonon scattering tend to be more interesting for phonon-strain field scattering. The matrix element contains the Fourier transform of the scattering potential; therefore, the real space behavior of the strain field will influence the ω-dependence of the matrix element contribution and by extension ω-dependence of the scattering rate. This will be discussed further in the context of dislocations in Sec. IV A 4.

When considering phonon–strain field interactions, it is important to clearly distinguish the concepts of anharmonicity and inelastic scattering. This distinction can be understood in the context of third order perturbation theory. Consider the third order contribution to the interatomic potential energy, $U_{3\mathrm{rd}}$ [Eqs. (A3) and (A4)]. Third order anharmonicity in the context of phonon-phonon interactions leads to inelastic scattering since each atomic displacement vector (u_i^α, u_j^β, and u_k^γ) in $U_{3\mathrm{rd}}$ corresponds to a phonon [Fig. 10(a)]. Phonon one (e.g., u_i^α) can be thought of as absorbing or emitting the energy of phonon two (u_j^β), which induces the transition into the phonon three (u_k^γ) of different energy. In contrast, when a phonon interacts with a static strain field [Fig. 10(b)], one of the atomic displacement vectors (e.g., u_j^β) can be thought of as representing the static strain field, which does not absorb or emit energy. Therefore, phonon one (u_i^α) and three (u_k^γ) must have the same energy. This concept is reflected in Eq. (19) of Carruthers, and the surrounding text,[63] and is illustrated here in Fig. 10.

The Grüneisen parameter (γ) is commonly used as a metric to quantify the anharmonicity of a material, which captures the change in phonon frequency [$\omega_s(\mathbf{q})$] with an applied strain (ε_{ij}). While the Grüneisen parameter is technically a tensor quantity mapping onto the strain tensor [see Eq. (11.74) of Wallace[64]],

$$\gamma_{ij}(\mathbf{q},s) = -\frac{\partial \ln \omega_s(\mathbf{q})}{\partial \varepsilon_{ij}}, \tag{24}$$

its trace, the hydrostatic Grüneisen parameter is commonly reported,

$$\gamma(\mathbf{q},s) = -\frac{\partial \ln \omega_s(\mathbf{q})}{\partial \ln V}, \tag{25}$$

in part because it does not require a breaking of symmetry to compute. The bulk, thermodynamic Grüneisen parameter (γ) is often measured using isothermal bulk modulus (B_{T}), isobaric thermal expansion (α_{P}), and heat capacity at constant volume (C_{V}),

$$\gamma = \frac{B_{\mathrm{T}}\alpha_{\mathrm{P}}}{C_{\mathrm{V}}}. \tag{26}$$

The bulk Grüneisen parameter [Eq. (26)] is related to the mode specific Grüneisen parameter [Eq. (25)] through a heat capacity weighted average

$$\gamma = \frac{\sum_{\mathbf{q}s} C_s(\mathbf{q})\gamma(\mathbf{q},s)}{\sum_{\mathbf{q}s} C_s(\mathbf{q})}. \tag{27}$$

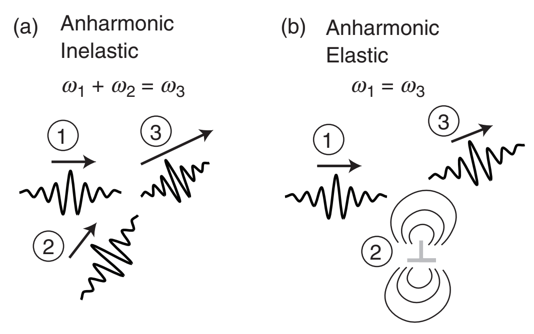

FIG. 10. (a) Conventional 3-phonon scattering during an absorption process (phonon 1 absorbs phonon 2 and transitions into phonon 3). This scattering is classified as anharmonic and inelastic since $\omega_1 \neq \omega_3$. (b) Phonon static strain field scattering. The static strain field does not contain the dynamical degrees of freedom to absorb or emit energy. Therefore, this process is classified as anharmonic and elastic since it is induced by the anharmonic term in the Hamiltonian and $\omega_1 = \omega_3$.

For analytical scattering theories, a scattering potential can be defined in terms of γ as (see Sec. 6.4.3 of Ziman[55])

$$V(\mathbf{r}) = \hbar\omega\gamma_{ij}\varepsilon_{ij}(\mathbf{r}). \quad (28)$$

It is common to apply Eq. (26) to this scattering potential and drop the tensor subscripts (*ij*).

4. Dislocations

The description of phonon-dislocation interactions is a complex topic with a long history.[60,63,65,66] It has been reviewed recently in the context of *ab initio* simulations (see Sec. III.2 in Lindsay *et al.*[10]). Here, we first discuss mechanisms for phonon-dislocation interactions (i.e., core, strain field, fluttering) and conceptualize the ω-dependence of the phonon scattering rate in the context of phase space and matrix element effects. We then review some recent cases where phonon-dislocation interactions have impacted technology. Finally, we highlight how dislocations behave as foundational defects, in that they provide a basis for describing more complex systems such as interfaces and even some aspects of amorphous materials (Fig. 11).

Dislocations are linear defects often described by two characteristic components, the dislocation core and the long-ranged strain field it induces. Early continuum-based models suggested that dislocation strain field scattering is generally larger than dislocation core scattering,[63,67] a conclusion that has since been supported in wurtzite GaN[68] using a Green's function approach based on DFT force constants.[69] However, dislocation cores are expected to couple to high frequency phonons,[70,71] and are shown to play a significant role in certain systems depending on dislocation density and type.

The dislocation strain field falls off as $\varepsilon \propto 1/r$, where r is the distance from the dislocation core. This results in a dislocation that resides in an infinite crystal exhibiting an infinite strain energy[72] and is often referred to as the "long-ranged" nature of dislocation strain. The strain energy and strength of phonon dislocation scattering is therefore expected to depend on the size of the crystallite the dislocation occupies, as well as the number and arrangement of other dislocations in the crystal due to interference between their individual strain fields. In simulations, dislocations are often arranged in configurations that cancel out this long-ranged strain field such that the defect can be contained within a simulation cell using periodic boundary conditions and a size that is not prohibitively large. In such configurations, the results of the simulation are expected to more heavily weight the dislocation core properties since much of the long range strain field is cancelled out.[73]

Dislocation strain scattering scales as $\tau^{-1} \propto \omega^1$. This ω-dependence can be rationalized by considering the strain field scattering potential, $V(\mathbf{r}) = \hbar\omega\gamma\varepsilon(\mathbf{r})$ [Eq. (28)]. The Fourier transform of this scattering potential is ω independent at low-ω, since the Fourier transform of $1/r$ contributes a $1/q$, and q is proportional to ω at low ω. This yields a ω-independent matrix element contribution ($|M_{2d}|^2$). Therefore the only ω dependence from dislocation strain scatter originates from phase space considerations, $g_{2D} \propto \omega^1$ for a linear defect. Dislocation strain scattering then takes the form

$$\tau^{-1} = \beta\gamma^2 b^2 n_{2D}\omega. \quad (29)$$

The value of β has been debated[60,63] and is expected to depend on the length scale of the strain field l (which is set by their arrangement and crystalline size) as well the local chemical environment.[74] A commonly used form is $\beta = \ln(l/b)^2/3$, which was originally suggested by Carruthers.[63]

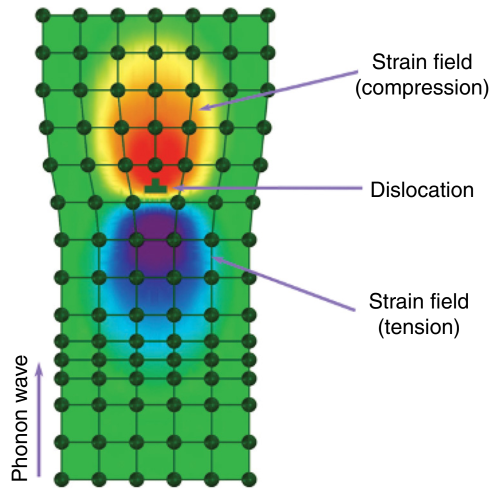

FIG. 11. Schematic illustration of a dislocation, the hydrostatic strain field it induces, and the phonon-dislocation interaction. The dynamic phonon displacement field couples to the static dislocation strain field and induces a scattering event.

Dislocation core scattering scales as $\tau^{-1} \propto \omega^3$ [Fig. 9(b)]. A ω^1 contribution comes from phase space effects. Analytical models treat the core as a localized (δ-function) scattering potential and therefore contribute ω^2 from the matrix element contribution.

Dislocations are also known to introduce vibrational states, which are not native to the pristine crystal.[75–77] It is important to distinguish dislocation "vibrational" motion (fluttering), from dislocation "glide" motion (often referred to simply as dislocation motion). Dislocation glide motion refers to the movement of the dislocation through the crystal and requires the breaking/making of bonds.

Early thermal conductivity measurements on LiF crystals containing dislocations at low temperatures by Anderson and coworkers,[65] indicated a dislocation scattering strength far larger than that predicted from phonons interacting with the static dislocation strain field. This led to the conclusion that the fluttering mechanism dominates in LiF at low temperatures. Later measurements by Zhu and Anderson[66] on Ge crystals containing dislocations showed much better agreement with static strain field scattering models. The conclusion that static strain field scattering dominates has been made in Si,[78] Ge,[66,79] Nb and Ta single crystals,[80] Cu-Al alloys,[81] and more recently in GaN.[68,82] MD simulations and dislon theory have the capacity to capture phonon interactions with vibrating dislocations.[76,83,183] By quantizing the dislocation field and defining a dislon Hamiltonian, the dislon formalism has the ability to treat the electron-phonon-dislocation on equal footing.[84] Additionally, it has the capacity to capture normal mode re-normalization and predicts significant lattice softening [Fig. 4(a) of Li *et al.*[76]]. Perturbation theory [Eq. (11)], which is commonly used to compute phonon-defect scattering rates, often neglects the presence of these dislocation induced vibrational states and only considers scattering due to the dislocation core and strain field.

Dislocations are a foundational lattice defect and the base unit for many other extended defects, such as grain boundaries and heterointerfaces.[85] Dislocation models for grain boundaries stem back to the classic Read-Schockley model,[86] which describes the structure of low-angle grain boundaries (misorientation angle less than about 15°). Since then the field of bicyrstallography has extended this concept to mathematically describe all crystalline grain boundaries as arrays of dislocations (see Sec. 2.3 of Priester[87]). Additionally, it is not uncommon to use dislocations and closely related disclinations[88] to describe the structural properties of amorphous materials.[89–91] Some have extended this concept to model the thermal conductivity of glasses at very low temperatures[92] where propagating phonons and the phonon-gas channel are expected to become important.

Phonon-dislocation interactions have gained attention recently in various technological fields. Many of the growth techniques for III-V compounds (e.g., GaN, InN) introduce a large number dislocations. Therefore, phonon-dislocation interactions can influence the thermal management of opto-electronic and power electronic devices.[82,93] A recent investigation even showed that directionally aligned dislocations could be used to engineer anisotropic thermal transport in otherwise fairly isotropic InN thin films for the purposes of directed heat dissipation.[93] Dislocations have also emerged as an effective means to decrease the vibrational thermal conductivity in thermoelectrics while maintaining a high electronic mobility.[94]

B. Softening

As discussed in Sec. IV A, crystal defects induce phonon scattering and reduce thermal conductivity by decreasing phonon lifetimes and mean free paths. From the common perturbation perspective, the bulk speed of sound and overall phonon dispersion is assumed to remain constant. This is to say that only phonon scattering is considered. Here, we review another important mechanism, which has received relatively less attention, where the average phonon velocities are altered directly.

In light of Eq. (4), phonon velocities are expected to play a significant role in the thermal transport of a phonon gas. Intuitively, to reduce thermal conductivity, it is desirable to reduce the average phonon velocity. This reduction can be referred to as elastic softening, lattice softening, or phonon softening. The average phonon velocity may be characterized by the bulk speed of sound[95] insomuch as it captures the average frequency of the phonon density of states.[96,97] Nevertheless, we consider measurements of the speed of sound to reflect changes to the bulk material in a thermodynamic sense. A measurement of defect induced elastic softening of a bulk material (such as ultrasound or heat capacity) indicates that the defects are present at a sufficient concentration to alter the bulk properties of the material. In this sense elastic softening goes beyond the classic perturbation approach since the average properties of the defective material are better described by a softened phonon dispersion and reduced elastic moduli.

The relative importance of elastic softening for tuning thermal transport (as compared to scattering) is expected to be larger in materials that have small intrinsic phonon mean free paths. In general, this pertains to materials at high temperature, having strong anharmonicity, and/or with high electronic charge carrier concentrations (Sec. IV B 2). Phonon softening expresses itself through several experimentally accessible material parameters, some of which are discussed in Sec. IV B 1.

Identifying and characterizing the physiochemical mechanisms that result in elastic softening is still an active area of research, as discussed in Sec. IV B 2.

1. Characterization methods

The acoustic phonon branches near the Γ-point can be characterized by bulk measurements such as the speed of sound and Debye temperature (see Appendix E for a detailed discussion), both of which relate directly to the elastic moduli.[98] As discussed in Sec. III, the acoustic branches are typically the dominant heat carriers, and their behavior at the Γ-point is expected to reflect the behavior of higher frequency phonon modes of similar polarization. Other experimental probes valuable to the study of lattice softening include:[99] Raman spectroscopy (which can measure energies of optical phonons at the Γ-point), Brillouin light scattering, and inelastic neutron and x-ray scattering (which can measure phonon dispersions and densities of states).

It is important to recognize that elastic softening is expected to significantly reduce thermal conductivity if the energy of acoustic modes is decreased. Tracking the energy of optical modes with Raman spectroscopy is not a direct measurement of the softening of acoustic branches, though it may be related.

2. Models and mechanisms

The mechanisms of elastic softening are, likely, not yet fully characterized. However, it has been shown that increased internal strain[95] (corresponding to residual stresses inside the dense material) and increased electronic carrier concentrations[100] are both correlated with elastic softening. The former is expected from the Grüneisen relation,[64] whereas the latter can be understood as a change in bond strength due to the population/de-population of bonding and anti-bonding orbitals as electrons are added or removed from the system. There are other reports of elastic softening without mention of an explicit mechanism.[101]

From a thermodynamic perspective, elastic softening corresponds to an increase in the vibrational entropy S_{vib} of a material. Since there is a general observation that entropy tends to increase when work is done to a system, softening may be expected to result due to changes in various thermodynamic variables. Considering a free energy function, such as the Helmholtz free energy

$$dF = -pdV - TdS + \sum_i X_i da_i, \tag{30}$$

an increase in entropy S is expected if the free energy is increased by pressure-volume (pdV) work and/or by the arbitrary conjugate variables X_i and a_i representing mechanism i. This effect has been coined the compensation law and has been demonstrated in free-energy-driven Arrhenius processes[102] and in the thermodynamics of solid-solutions.[103] Entropy in a system can contain several contributions such as vibrational and configurational entropy ($S = S_{vib} + S_{config} + \cdots$). The differential change in S_{vib} due to changing phonon frequencies, which contributes to the total change in entropy, can be characterized as[104]

$$dS_{vib} = -c_V d \ln \bar{\omega}, \tag{31}$$

where c_V is the heat capacity (in units of J K^{-1}) and $\bar{\omega}$ represents a characteristic (average) vibrational frequency that is related to the speed of sound ($v_S \propto \bar{\omega}$). As there may be other mechanisms by which the material can increase the total entropy, then the magnitude of softening depends on the specifics of the material system. It may be possible, however, to utilize Maxwell relations to relate the magnitude of softening to other material properties, which is the origin of the Grüneisen parameter[64] [Eq. (26)].

Nevertheless, even rather subtle changes in phonon velocities can have drastic consequences for thermal transport. Especially for phonon gas transport at high temperatures ($T > \theta_D$), when phonon-phonon scattering dominates (Appendix B 4),

$$\kappa_{pg} = A\frac{v_S^3}{T}. \tag{32}$$

The coefficient A can be computed using material properties [Eq. (B24)] to provide an estimation for the magnitude of κ_{pg}. However, for detailed analysis of a particular material system (including variations with synthesis and characterization procedures), A is commonly calibrated to a control sample. The $\kappa_{pg} \propto v_S^3$ relationship indicates that κ_{pg} can be very sensitive to elastic softening. While this assumes only phonon-phonon scattering is present, phonon-defect scattering effects are often present as well. In the limit of amorphous-like thermal transport, $\kappa_{vib} \propto v_S$ is expected[96,105] (see Sec. VI A). Thus, there is a general proportionality, $\kappa_{vib} \propto v_S^n$, with $1 \leq n \leq 3$.

V. THERMAL BOUNDARY RESISTANCE

Understanding the thermal effects of grain boundaries and interfaces is often critical to device performance, since these planar defects are often present in engineered materials. In power electronics, the objective is to minimize thermal resistances at boundary defects to improve device heat dissipation, which leads to an increase in power density, switching speeds, and device lifetime. In contrast, the increasingly common nanostructuring paradigm for thermoelectrics aims to suppress thermal transport by creating a high density of thermally resistive grain boundaries, which should not greatly perturb the electronic transport.

Fundamental questions about how thermal boundary resistance relates to the structure and composition at the boundary can be difficult to answer, since bulk thermal conductivity measurements typically probe the ensemble averaged interface scattering in a polycrystal. In addition, while isolating and characterizing a single interface is possible, it is currently time intensive and expensive. Nonetheless, recent progress has been made in measuring,[106,107] modeling,[108–110] and understanding the thermal boundary resistance (R_B) and its inverse, thermal boundary conductance ($h_B = 1/R_B$), defined as

$$j = -h_B \Delta T, \tag{33}$$

where j is the heat current normal to the interface, and ΔT is the temperature drop across the interface.

To realize an engineering strategy for interfacial thermal transport, several materials level questions must be addressed, including: When constituent materials are fixed, what chemistry and structure-related factors set R_B, and can they be controlled? If so, how much can R_B be tuned using chemistry and processing? If constituent materials are not fixed for a particular application, can materials be selected to intentionally increase or decrease R_B?

A. Measurement methods

Accurate measurements of thermal boundary resistance (R_B) are typically expensive and time intensive in part because of the difficulty in isolating a single interface. Additionally, the characterization of interfacial structure and vibrational properties is often required to interpret the measurements, which is also expensive. Two widely utilized methods for measuring the thermal boundary conductance (h_B) and resistance (R_B) are the 3ω method[111,112] and time domain thermoreflectance (TDTR).[107,113–116] The 3ω method uses a metal wire deposited on the sample surface to both apply the heat pulse and measure temperature through the temperature dependent resistivity of the wire. The TDTR method uses a pump-probe laser to both apply the heat pulse and measure temperature through the temperature dependent reflectively on the sample surface (or more commonly a metal transducer). Both methods rely on the measurement of temperature vs time after a thermal pulse is applied to the sample and a model is used to determine the thermal properties of interest such as the thermal conductivity or the R_B of interfaces within the sample. Samples often consist of layers of materials (transducer/sample/substrate) and the sensitivity to the R_B of a specific interface is highly dependent on the thermal conductivity and thickness of the layers, and thermal penetration depth of the measurement, which is tuned by changing the frequency of the heat pulse (in both 3ω and TDTR methods). Therefore, these types of measurements rely on careful sample design and models that predict the sensitivity of the measurement to various sample geometries and measurement conditions.

The 3ω method starts by applying an oscillating current through the heater wire at 1ω. This induces a localized Joule heating at 2ω. The increased temperature changes the resistivity of the wire also at 2ω. The measured voltage then oscillates at 3ω, since this signal contains both the 1ω applied current and the 2ω change in resistance. The thermal properties of the sample are contained within this 3ω voltage signal. Compared with TDTR method, 3ω is a relatively simple and low-cost method, since it requires the application of electrodes and standard electronics (i.e., voltmeters and a lock-in amplifier). However, when measuring R_B, care must be taken in sample design and preparation to ensure that the geometry and thermal properties of the electrode, sample layers, and substrate result in a measurement that is sensitive to the R_B of interest. Since 3ω method relies on the electrical voltage oscillation, there are complexities that arise when measuring metals and semiconductors. In these cases, an electrically insulating layer is needed between the sample and the metal sensor, which may decrease the sensitivity of the measurement to a buried interface of interest.

For metal/semiconductor interfaces, the metal (e.g., Al and Au) can sometimes be directly used as the transducer for TDTR measurement, which makes TDTR method suitable for metal-non-metal interfaces.[107] For efficient heat dissipation in devices, a high thermal boundary conductance (TBC) is usually preferred to improve the device thermal management, and h_B can be 100 MW/m^{2}K or higher. The sensitivity of TDTR to high TBC interfaces can be sufficient, and the sensitivity increases with substrate thermal conductivity.[14] However, because of the optical nature of TDTR method, it usually requires high quality of the sample surface (surface roughness within tens of nanometers), which is not necessary for 3ω measurement. The penetration depth of TDTR is usually from tens of nanometers to a few microns at room temperature and depends on the modulation frequency (usually about several MHz) and material thermal properties. Therefore, sensitivity limitations can make the measurement of deeply buried interfaces difficult. Recently, steady-state thermoreflectance (SSTR) with much lower modulation frequency (about 100 Hz) was shown to exhibit a much larger penetration depth making it a promising method for the measurement of TBC of buried interfaces moving forward.[117]

Models for R_B and h_B (TBC) often do not agree with measurements. However, a recent study of thermal transport across an atomically sharp and ultraclean Al-sapphire interface (confirmed by transmission electron microscopy) showed a good agreement between models for TBC and measurements made by TDTR.[107] This demonstrates the importance of coupling TBC measurement with detailed characterization of the interface in question. The structure and local chemistry of the interface is expected to significantly impact the value of the measured TBC, such that a model that assumes a perfect interface may not be appropriate. This also provides motivation for the development of methods that can capture the effects of nanoscale structure and chemistry at the interface, such as molecular dynamics and perturbation approaches, since interfaces are rarely perfect in real technology. For example, the interfacial strain scattering approach predicts that interfacial strain fields due to misfit dislocations at a Si-Ge interfaces increase R_B by a factor of two compared to the pristine interface.[110]

B. Physical mechanisms

Thermal boundary resistance can be induced by many scattering contributions across very different length scales, making phonon-interface scattering an inherently multiscale problem. Each of these scattering contributions influences the transmission probability of a phonon across the interface, which underpins the thermal boundary resistance. Scattering sources can be categorized into elastic and inelastic processes (Fig. 10) and include the following:

1. Elastic
   (a) Acoustic impedance mismatch
   (b) Interfacial strain fields (e.g., lattice misfit or dislocation arrays)
   (c) Mass density variance (e.g., dislocation cores, point defect mass contrast, alloy/amorphous layer with differing mass density)
   (d) Force constant variance (e.g., dislocation cores, bond strength variation due to point defects, alloy/amorphous layer with differing elastic moduli)
2. Inelastic
   (a) Phonon coupling to interfacial vibrational modes

While the acoustic mismatch is fixed for a given material and interface orientation, the other contributions can increase R_B and are related to the structure and chemistry of the interface. The interfacial mode coupling is the only scattering source that takes into consideration the dynamical properties of the interface, while all other phenomena can be defined from the standpoint of a static interface.

C. Specularity and length scale considerations

The scattering sources listed above are distinct in the scattering transitions they imply. As depicted in Fig. 13, the modeled phonon transitions range from purely specular to purely diffuse, as fewer components of the momentum are conserved. An analogy can be drawn between the scattering transitions discussed in the context of defect dimensionality (see Fig. 9) and the scattering transitions discussed here. The acoustic mismatch is typically treated as an abrupt, step-function change in acoustic impedance at the interface. The resulting scattering potential cannot impart momentum in the plane of the interface, and as such, the phonon transitions are limited to either specular reflection or transmission.[110,118] In other words, the acoustic mismatch scattering potential can be thought of as a planar defect, such that phonons are limited to the phase space depicted in Fig. 9(c). The classical acoustic mismatch model (AMM), an acoustic analog of Snell's law, captures this effect. The AMM evaluates a transmission probability determined by the ratio of acoustic impedances at the interface.[14] The other end of the spectrum is fully diffuse scattering, in which phonons lose all memory of their incoming polarization and direction and conserve only energy [see Fig. 9(a)], as assumed in the diffuse mismatch model (DMM). While the AMM assumes an atomically sharp and flat interface, the DMM is consistent with a highly disordered and rough interface. The physical origin of the interface scattering is typically not specified in the DMM. Instead, the scattering probability is set only by the available phase space on either side of the interface (from perturbation theory considerations[119]) captured by the 3D phonon density of states mismatched for the incoming phonon frequency ω. The AMM and DMM are thought to provide upper and lower bounds on the thermal boundary resistance, but these standard models tend to neglect the structure and properties of the interface itself.[120]

The scattering from interfacial dislocation arrays, present at many low-energy grain boundaries and interfaces, sits between these limits of specular and diffuse scattering.[110,121] The periodic strain fields induced by the dislocation arrays act as a diffraction grating for phonons, leading to a finite set of allowed transitions.[60,63] The dislocation strain field can impart momentum in the direction of periodicity quantized in units of $2\pi/D$, where D is the dislocation spacing.[110,118,122] Since dislocation density can vary with grain boundary type, models that include this form of diffractive scattering capture experimentally and computationally observed trends between thermal boundary resistance and grain boundary angle.[109,110,118,123]

In reality, different energies and wavelengths of the phonon spectrum are expected to couple to different levels of structure at the boundary. Short-wavelengths phonons will interact with dislocation cores and point defects decorating the boundary,[70] while mid-wavelength phonons with wavelengths on the order of the interfacial dislocation spacing D will couple to dislocation strain.[124] Finally, very long wavelength phonons will remain agnostic to features local to the boundary and will experience specular scattering due to the acoustic mismatch. In Sec. III we highlight how mid to low frequency acoustic phonons carry a significant amount of energy, indicating the importance of capturing nanoscale structure at the interface as well as far-field effects.

D. Low-T thermal conductivity of polycrystals

The thermal conductivity at low temperatures ($T \leq \theta_D$) contains more information regarding phonon-microstructure scattering than high temperatures ($T > \theta_D$). At low-T, the mean free path and relaxation time are limited by interactions with microstructural defects rather than other phonons. From Eqs. (4) and (B3), one can find that $\kappa \propto T^3$ is consistent with an ω-independent τ^{-1}, and $\kappa \propto T^2$ is consistent with $\tau^{-1} \propto \omega$, at low-T. Experimentally, when phonon propagation is limited by crystal surfaces at the edge of single crystals, T^3 is commonly observed. When phonon propagation is limited by grain boundaries in polycrystals, T^2 is commonly observed (Fig. 12).

Wang *et al.* demonstrated this effect in nanocrystalline Si and identified that this T^2 behavior is best explained by a frequency dependent relaxation time, mean free path, and transmissivity.[125] This is in contrast with the highly common "gray model" assumption, which asserts that the mean free path is limited to the grain size and is therefore ω-independent. Hua *et al.* measured a frequency-dependent transmissivity at Al-Si interfaces,[126] demonstrating that this behavior is not limited to homointerfaces (such as grain boundaries). Hua *et al.* additionally emphasized the importance of non-gray scattering on thermal conductivity through Monte Carlo simulations, showing that the gray model severely underestimates the contribution of long-wavelength phonons to the overall thermal conductivity.[127] In original reports the origin of the ω-dependent τ was unknown in detail, and it was suggested that it is related to interfacial roughness.[125] Since then, models which treat the interfacial structure in more detail suggest that the ω-dependence arises from the roughness induced by interfacial dislocations (which are well described using bi-crystallography), and that heat carrying phonons most strongly couple to the interfacial strain fields they induce. Kim *et al.* originally suggested that frequency dependence stemming from dislocation strain scattering provides a likely explanation for the T^2 behavior.[67] By applying an interfacial perturbation approach to the Read-Shockley dislocation-array model for grain boundaries, this conclusion was found to hold for scattering off a grain boundary defect.[118] However, a sharp change in the ω-dependence of the phonon transmissivity is predicted, similar in nature to that measured by Hua *et al.*,[126] when the full dislocation array is considered. This change in ω-dependence stems from a dimensionality crossover effect. Below the crossover frequency, the phonon scatters off of the long range (step-function like) change in elastic properties, and τ^{-1} is frequency independent [planar defect scattering, Fig. 9(c)]. Above the crossover frequency, the phonon scatters off of the interfacial strain field, which arises from the nanoscale features of the interfacial dislocation array, resulting in $\tau^{-1} \propto \omega$ from phase space considerations[110] [linear defect scattering, Fig. 9(c)].

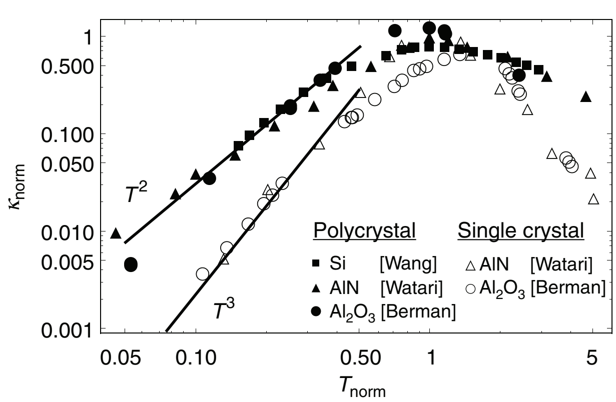

FIG. 12. Low temperature vibrational thermal conductivity of polycrystals compared to single crystals revealing fundamental differences between phonons scattering on external crystal surfaces and internal grain boundaries. A T^3 temperature dependence is consistent with frequency independent phonon scattering, which is in line with the legacy acoustic and diffuse mismatch models, as well as the simple "grey" scattering model. A T^2 temperature dependence is consistent with $\tau^{-1} \propto \omega$ scattering, which is missed by legacy models. Data are from Wang,[125] Berman,[128] and Watari.[129] Figure modified from Hanus *et al.*, Commun. Phys. **1**, 78 (2018).[118]

E. Thermal boundary resistance models

There exist several general approaches for modeling thermal resistance at an interface. Certain approaches can, by design, omit potentially important physical mechanisms discussed (e.g., nanostructure, strain fields, atomic segregation, disorder). We will first introduce theoretical approaches in increasing level of detail. Then, in Sec. V E 2, we will show how these seemingly separate frameworks can be related.[130]

The Landauer-type approach captures all details regarding phonon-interface interactions in a probability of transmission $t(\omega)$ [or $t(\mathbf{q}s)$]. Therefore, any details such as the presence of an amorphous interfacial layer, misfit dislocation strain fields, and the associated interfacial vibrational modes are buried within $t(\omega)$.

Another common method is an application of the Peierls-Boltzmann transport equation, which treats the material as a homogeneous solid with a relaxation time that is modified by the additional interfacial scattering through Mattheissen's rule. This approach allows one to treat the interface as a perturbation, which is described by introducing a scattering potential, which is seen by an incoming wave-packet and induces a scattering probability and relaxation time through quantum perturbation theory [Eq. (D1)]. This method assigns a physical mechanism for phonon-interface coupling through the definition of a scattering potential (V), and the modeling results can then be compared to experiment or computational simulation. We call this the interfacial perturbation approach, which can naturally capture nano-scale structural features and transitions from specular to diffuse scattering (i.e., the conservation of phonon momentum within the plane of the interface). This approach has been applied to tilt and twist grain boundaries, semi-coherent interfaces,[110] and ferroelectric domain walls.[131]

1. Landauer-type models

In both the Landuaer and interfacial perturbation treatments, each frequency ω is considered an independent conduction channel. The thermal conductivity of the bulk, interface free system is given by Eq. (4) with only phonon-phonon scattering $\tau(\omega) = \tau_{pp}(\omega)$. Here we will focus on the thermal conductivity of one channel with frequency ω,

$$\kappa_{bulk}(\omega) = \frac{1}{3} C(\omega) v_g(\omega)^2 \tau_{pp}(\omega), \tag{34}$$

and its corresponding thermal resistivity $\kappa_{bulk}(\omega)^{-1}$.

The first method we examine is based on the Landauer method, which simply computes the conductance of particles encountering an interface when each particle is assigned a transmissivity $t(\omega)$.[132] When the Landauer approach is applied to phonons, each channel carries a heat capacity $C(\omega)$, at a speed equal to the group velocity $v_g(\omega)$. Within this formulation the thermal boundary conductance is given by

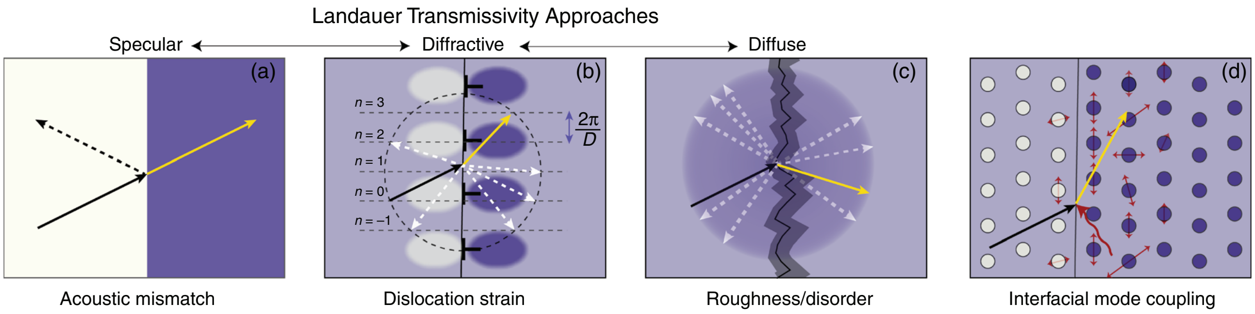

FIG. 13. Schematic illustrations of major scattering sources at an interface. Each scattering mechanism implies different scattering phase spaces and can be compared to the defect phase space diagrams in Fig. 9: (a) The acoustic impedance mismatch across the interface can lead to a reflection or transmission probability in analogy to Snell's law [see planar defect scattering Fig. 9(c)]. (b) Many low-energy interfaces can be decomposed into periodic arrays of dislocations, which act as a diffraction grating for phonons. The dislocation array can impart quantized momentum in units of $2\pi/D$, where D is the dislocation spacing [see linear defect scattering Fig. 9(b)]. (c) Interfaces serve as a sink for point defects, leading to additional roughness and compositional disorder. These effects are often modeled as a source of diffuse phonon scattering, in which the only conserved quantity is phonon energy [see point defect scattering Fig. 9(a)]. (d) Finally, if the basis set includes the interfacial vibrational modes, such as the localized mode portrayed here, coupling to interfacial modes can also enhance or diminish the interfacial thermal conductance through inelastic processes.

$$h_{\mathrm{B}} = \int h_{\mathrm{B}}(\omega)d\omega\,, \tag{35}$$

$$h_{\mathrm{B}}(\omega) = \frac{1}{4}C(\omega)v_{\mathrm{g}}(\omega)\frac{t(\omega)}{1-t(\omega)}. \tag{36}$$

Additionally, it will be convenient to define the thermal boundary resistivity $(L_z\,h_{\mathrm{B}}(\omega))^{-1}$ where L_z is the linear spacing between boundaries as shown in Fig. 14. Since the bulk material and interfaces are in series in this model, the total thermal resistivity of the conduction channel ω is given by the sum of the resistivities

$$\kappa_{\mathrm{pg}}(\omega)^{-1} = \kappa_{\mathrm{bulk}}(\omega)^{-1} + (L_z\,h_{\mathrm{B}}(\omega))^{-1}. \tag{37}$$

If the spectral properties, or mode specific properties of the thermal boundary resistance and bulk thermal conductivity are neglected, one can write the total thermal conductivity simply as

$$\kappa_{\mathrm{pg}}^{-1} = \kappa_{\mathrm{bulk}}^{-1} + (L_z\,h_{\mathrm{B}})^{-1}. \tag{38}$$

In practice, Eq. (38) can be useful when characterizing the grain size dependence of thermal conductivity[133–135] for material systems where a bulk series resistance model has strong physical significance, such as the presence of a thick grain boundary phase. However, this picture is not expected to hold for phonons that have a wavelength comparable to or longer than the interfacial thickness. Equation (37) recognizes that an interface can be less resistive to low-ω phonons

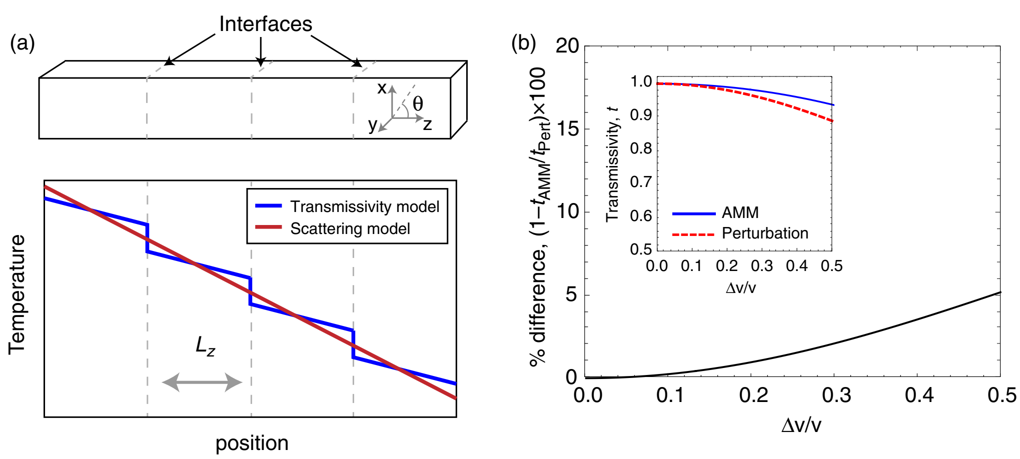

FIG. 14. (a) A schematic illustration of two common models used to describe heat conduction in materials with interfaces. The vertical can be interpreted as temperature of a specific conduction channel, which can be either a specific phonon mode $\mathbf{q}s$ or frequency ω depending on the level of detail of the model. The blue line depicts the Landauer based model where a thermal boundary resistance arising from the conduction channel having an interfacial transmission probability, $t(\mathbf{q}s) > 1$ (or $t(\omega) > 0$), induces an instantaneous drop in temperature. The red line depicts a model based on phonon scattering theory and Matthiessen's rule, where each scattering mechanism contributes a scattering rate $[\tau(\mathbf{q}s)^{-1}$ or $\tau(\omega)^{-1}]$ and thermal resistance to the conduction channel. (b) A comparison between the transmissivity calculated using classical acoustic mismatch (AMM) theory and quantum perturbation theory [Eqs. (43) and (42)]. The two differ no more than 5% across the entire range. Reproduced from Ramya Gurunathan *et al.* Phys. Rev. B **103**, 144302 (2021),[110] with permission of AIP Publishing.

than to high-ω phonons,[110] and that phonons at the longest wavelengths (i.e., ultrasound) pass through the interface unperturbed (mean free path larger than L_z).

2. Interfacial perturbation models

The second method introduces the interface as an additional scattering mechanism that can reduce the phonon lifetime. The relaxation time due to this scattering mechanism can be calculated using the scattering theory presented in Sec. IV A. The total thermal resistivity is calculated as the sum of the resistivity due to phonon-phonon scattering and the resistivity due to boundary scattering, $\kappa_{\mathrm{B}}(\omega) = C(\omega)v_{\mathrm{g}}(\omega)^2\tau_{\mathrm{B}}(\omega)/3$,

$$\kappa_{\mathrm{pg}}(\omega)^{-1} = \kappa_{\mathrm{bulk}}(\omega)^{-1} + \kappa_{\mathrm{B}}(\omega)^{-1}, \tag{39}$$

or equivalently

$$\kappa_{\mathrm{pg}}(\omega) = \frac{1}{3}C(\omega)v_{\mathrm{g}}(\omega)^2\tau(\omega), \tag{40}$$

with $\tau(\omega)$ having the familiar form [Eq. (10)]

$$\tau(\omega)^{-1} = \tau_{\mathrm{ph}}(\omega)^{-1} + \tau_{\mathrm{B}}(\omega)^{-1}. \tag{41}$$

Since this relaxation time is derived by considering perturbations to the crystal Hamiltonian, this method has the capacity to capture materials physics, which may be missed by the classic definitions of transmissivity (e.g., AMM and DMM). In the perturbation theory approach, the effects of defect dimensionality and spatial extent of the scattering potential, as well as the physical origin of the phonon scattering are naturally built into the theoretical framework (e.g., anharmonicity, elastic anisotropy, local changes in atomic mass or interatomic force constants, etc.).

However, the two approaches can be related by equating Eqs. (38) and (39),

$$t(\omega) = \frac{\tau_{\mathrm{B}}(\omega)}{\frac{3}{4}\frac{L_z}{v_{\mathrm{g}}(\omega)} + \tau_{\mathrm{B}}(\omega)}. \tag{42}$$

Here, we will define τ_{B} using the perturbation due to an acoustic mismatch at the boundary between two Debye solids. The mass density on side 1 and side 2 of the interface will be assumed equal ($\rho_1 = \rho_2$), and the phonon velocities will be defined as $v_1 = v + \Delta v/2$ and $v_2 = v - \Delta v/2$. Therefore, an acoustic mismatch perturbation can be defined $V_{\mathrm{AM}}(z) = \hbar\Delta v q\Theta(z)$ where $\Theta(z)$ is the Heaviside step function. Following Gurunathan *et al.*,[110] the following acoustic mismatch relaxation time can be derived:

$$\tau_{\mathrm{B}}(\mathbf{q})^{-1} = \frac{\Delta v^2}{2L_z v_1|\sin\theta\cos\phi|}. \tag{43}$$

Using this equation with the acoustic mismatch perturbation theory given in Eq. (43), we obtain

$$t_{\mathrm{Pert}} = \frac{1}{\frac{1}{2}\left(\frac{\Delta v_{\mathrm{S}}}{v_{\mathrm{S}}}\right)^2 + 1}. \tag{44}$$

In the classical 1D AMM theory, the transmissivity is given by[119]

$$t_{\mathrm{AMM}} = \frac{4Z_1Z_2}{(Z_1+Z_2)^2}, \tag{45}$$

where $Z_i = \rho_i v_{\mathrm{s},i}$ is the acoustic impedance of side i, and ρ_i is its mass density. For direct comparison with the perturbation theory approach derived here, we set $v_{\mathrm{s},1} = v_{\mathrm{S}} + \Delta v_{\mathrm{S}}/2$, $v_{\mathrm{s},2} = v_{\mathrm{S}} - \Delta v_{\mathrm{S}}/2$, and $\rho_1 = \rho_2$. The two are compared in Fig. 14(b), where Eq. (43) is converted to a transmissivity using Eq. (42). The two are identical at $\Delta v/v < 0.2$ and differ no more than 5% across the entire range, which captures most solid-solid interfaces. While intuition might suggest that perturbation theory cannot capture the significant changes in the acoustic medium at grain boundaries and interfaces, the close correspondence shown here suggests that perturbation theory is still predictive.

3. Interfacial modes and MD

Thus far, our discussion of scattering sources has largely assumed that the interface is a static defect. A static interface would lack the dynamical degrees of freedom to absorb or emit energy, and so the scattering processes described so far are elastic. However, atomistic simulations, like the ones described in this section, have revealed that inelastic interactions can play a significant role in thermal boundary conductance h_{B} predictions.[136] Inelastic processes occur when bulk vibrational modes couple to interfacial vibrational modes, defined as eigenmodes with large displacements for interfacial atoms, which form due to the higher degree of anharmonicity at the interface relative to the bulk.[136–139,181] Their role in interface conductance problems has thus far largely been discerned through molecular dynamics simulations.

Molecular dynamics (MD) simulations, as mentioned in Sec. II B, use classical mechanics to update atom positions and velocities in each time step of the simulation. Unlike the scattering frameworks described previously, individual scattering contributions do not have to be separately modeled or understood in an MD simulation, as they will be naturally captured as long as the harmonic and anharmonic properties of the lattice are well-described by the MD interatomic potentials. Molecular dynamics (MD) simulations can be used to compute a Kapitza conductance h_{B} directly from the simulation temperature profile once steady state has been established. Much of the currently available data used to understand h_{B} trends between grain boundary type, angle, and orientation stem from MD investigations. Several similar strategies exist for extracting the Kapitza resistance from MD simulations.[108,140] One common approach described by Schelling *et al.*[108] involves adding and subtracting energy $\Delta\varepsilon$ from a thin slab of atoms on either side of the boundary, which fixes the thermal current [j in Eq. (33)]. Then, the temperature discontinuity at the interface is computed from the temperature profile (ΔT) such that the h_{B} can be solved by using Eq. (33).

MD simulations offer many advantages through being a real-space, time-domain technique. For example, using the Green-Kubo modal analysis method, the modal contributions to the atom positions and velocities can be determined, allowing one to then evaluate the modal contributions to the Hardy heat flux operator $\mathbf{j}$.[11,26,141] The Green-Kubo formalism can then be applied to evaluate the thermal conductivity from the time correlation of the heat fluxes as

$$\kappa = \frac{1}{Vk_{\mathrm{B}}T}\int_0^{\infty}\langle \mathbf{j}(0)\cdot\mathbf{j}(t)\rangle dt. \tag{46}$$

This time-correlation approach can have major benefits over the phonon gas model when phonon velocities are ill-defined, which tends to occur in highly disordered materials and complex unit cell materials, common in the field of thermoelectrics.[141] However, interpreting these simulations can become a challenge since post processing or controlled wave packet simulations[142] must be performed to extract mode specific properties.

A similar modal analysis technique has been developed by Gordiz and Henry specifically for interface conductance and is referred to as interface conductance modal analysis (ICMA).[136–138] This technique has revealed that, in certain cases, a new set of vibrational eigenmodes, unique to the interface, must be included in the analysis to fully describe the heat flow across the interface. In the case of a Si-Ge heterointerface, the interfacial modes were shown to contribute to heat transfer, increasing the h_B relative to the model that excluded these modes.[138] A more comprehensive survey of interfaces between different materials has since suggested that interfacial mode coupling may be a unique feature of interfaces between certain structure types, like the diamond cubic lattices of Si and Ge.[139]

Finally, an increasingly popular alternative simulation approach is the atomistic Green's function (AGF). As with lattice dynamics (see Sec. II B), AGF is a reciprocal space approach and is useful for studying the spectral dependence of phonon transmission at an interface.[142] Physically, the Green's function represents the response of the lattice dynamical equations to an impulse perturbation. The AGF can be applied to the interface scattering problem in a straightforward way by re-framing the system as two contact materials, each described by a separate Green's function, which are then coupled at the interface. The system's dynamical response to the perturbation caused by this coupling is captured by this approach and used to compute a spectral phonon transmission coefficient.[143] While this approach is known to perform efficiently in the ballistic regime, anharmonic scattering effects have been notoriously difficult to implement, although developing anharmonic extensions to the AGF is a rapidly progressing initiative.[144,182]

VI. DISORDERED MATERIALS

In disordered materials, the phonon-gas model is expected to be an incomplete description of vibrational thermal transport.[11,28] The broadening and eventual disappearance of diffraction peaks is often used as a structural characterization of disorder. In terms of vibrational properties and thermal conductivity, a key characteristic of disordered or glass-like behavior is the loss of a measurable dispersion relation. However, recent inelastic x-ray scattering and simulation work by Moon *et al.*[145,146] demonstrates that amorphous silicon, a material with no crystal diffraction peaks, supports an acoustic dispersion relation up to 40 meV (well into the thermal phonon energy range), corresponding to wavelengths as short as 6 Å. In contrast, crystalline $Yb_{14}MnSb_{11}$, which does show diffraction peaks, exhibits no clear acoustic branches above 3 meV, and simulations indicate it conducts primarily through the diffuson channel above room temperature.[29] Therefore, in terms of vibrational properties and thermal transport, a material can exhibit characteristics of a glass while structurally exhibiting characteristics of a crystal, and vice versa. These counter-intuitive findings highlight the potential for discovery in disordered materials and how modern experimental and computational techniques are poised to unlock new understanding.

Molecular dynamics has been applied extensively to study disordered materials. The reader is referred to the recent review by DeAngelis *et al.*[11] for an overview. Here, we review analytical models for the glassy/minimum/diffuson-mediated thermal conductivity. Then the history, current work, and future implications of two-channel lattice dynamics and diffuson-channel are discussed. The relationship between these topics is discussed throughout.

A. The "minimum" thermal conductivity

The concept of a minimum thermal conductivity has important implications, since it provides practical limits for technological design. There are several analytical models[96,105,147] that attempt to compute the minimum thermal conductivity. Their similarities and differences can be observed by viewing them within a consistent framework

$$\kappa_{\mathrm{vib}} = \frac{1}{3}\int C(\omega)D(\omega)d\omega, \tag{47}$$

where $C(\omega)$ is the heat capacity given in Eq. (B14), and $D(\omega)$ is the frequency dependent diffusivity. From random walk theory, the diffusivity is defined as

$$D(\omega) = \alpha^2 \frac{N}{t}, \tag{48}$$

where α is the jump distance (i.e., the length-scale of diffusion) and N/t is the number of jumps per unit time. Analytical models[96,105] commonly follow Einstein[148] in their definition of

$$\frac{N}{t} = \frac{2\omega}{2\pi}P, \tag{49}$$

assuming that vibrational energy attempts a jump every half period of oscillation and completes the jump every attempt (probability $P = 1$).

The differences in analytical models typically arise in the treatment of the jump distance α. The jump distance defined by Cahill and Pohl[105] is set to half the vibration wavelength

$$\alpha_{\mathrm{CP}} = \frac{1}{2}\lambda = \frac{1}{2}\left(\frac{2\pi v_{\mathrm{S}}}{\omega}\right), \tag{50}$$

where λ is obtained by using the low-frequency speed of sound v_S. Equations. (47)–(50) lead to an expression for the temperature-dependent minimum thermal conductivity as

$$\kappa_{\mathrm{CP}} = \frac{k_B T^2}{2\pi v_S \hbar^2}\int_0^{x_D} \frac{x^3 e^x}{(e^x - 1)^2}dx, \tag{51}$$

where $x = \hbar\omega/(k_B T)$, $x_D = \hbar\omega_D/(k_B T)$, and ω_D is given in Eq. (E1). Equation (51) is equivalent to Eq. (3) of Cahill and Pohl.[105] In the high temperature limit, Eq. (51) simplifies to[96]

$$\kappa_{\mathrm{CP}} = 1.21 k_B n^{2/3} v_S, \tag{52}$$

since the number density of atoms n and speed of sound v_S define ω_D.

Since the jump distance (α_{CP}) is defined using the speed of sound, the Cahill-Pohl model is consistent with the maximum phonon scattering picture where $D = v_g\Lambda$ and the mean free path is half of the wavelength, i.e., $\Lambda = \lambda/2$.

The diffuson-mediated model presented by Agne, Hanus, and Snyder[96] does not rely on a well-defined E-q relation like that needed to describe phonon gas transport. Instead, they start from a vibrational density of states picture where a well-defined wavevector is not needed. The model is then developed by supposing all vibrations in the density of states behave as diffusons with a jump distance equal to a characteristic interatomic distance,

$$\alpha_{\rm AHS} = n^{-1/3}, \tag{53}$$

where n is the number density of atoms in the solid. This leads to an estimate for the minimum thermal conductivity,

$$\kappa_{\rm AHS} = \frac{n^{1/3}k_{\rm B}}{\pi}\omega_{\rm avg}(T), \tag{54}$$

that is proportional to the (temperature dependent) average frequency of vibration in the solid.

Through a heuristic correlation of the average frequency of the vibrational density of states with the Debye frequency, $\omega_{\rm avg} \approx 0.61\omega_{\rm D}$, then $\kappa_{\rm AHS}$ can be recast in the same form as Eq. (51) [see Eq. (18) in Agne *et al.*[96]], which has a high temperature limit defined by the speed of sound as

$$\kappa_{\rm AHS} \approx 0.76 k_{\rm B} n^{2/3} v_{\rm S}. \tag{55}$$

Comparison of the high temperature limits of the Cahill-Pohl and Agne-Hanus-Snyder models [Eqs. (52) and (55)] leads to the conclusion that $\kappa_{\rm AHS}$ is about 37% lower than $\kappa_{\rm CP}$ on average. This is consistent with the fact that the average oscillator jump distance in the Cahill-Pohl model is ~20% larger than that used by Agne-Hanus-Snyder. As an estimate of the minimum thermal conductivity, it makes sense to consider the smallest possible jump distance, i.e., the interatomic distance as first noted by Kittel[149] and used by Clarke.[147] The fact that $\kappa_{\rm CP}$ is a good predictor of the magnitude of the thermal conductivity of glasses[150] is in agreement with the idea that the average length-scale of thermal diffusion should be somewhat higher than the interatomic distance.[27]

We note in passing that these minimum thermal conductivity models are for isotropic bulk materials and that thin films and layered or highly anisotropic materials may have additional considerations.[151,152]

B. The diffuson channel

It is widely accepted that the phonon-gas model is an incomplete description of vibrational thermal conduction, even when considering the harmonic phonon decomposition.[26,153] This was first identified by Hardy in 1963, where through definition of the energy-flux operator and its application to the harmonic phonon decomposition the thermal energy flux is represented by a matrix containing diagonal and non-diagonal terms [see Eqs. (3.29)–(3.31) in Hardy[26]] Before Hardy's work, the phonon-gas model was obtained by considering the phonon modes of a monatomic linear chain, which results in a single acoustic branch shown in the blue box of Fig. 3(a). This 1D lattice naturally misses any effects that may arise due to quasi-degeneracy[16] [shown as red shading in Fig. 3(a)], since only one branch exists. When Hardy derived the thermal energy flux operator in 3D, even a monatomic lattice exhibited three branches at any given **q**-point (one longitudinal and two transverse modes), and therefore, it became apparent that there is a contribution to thermal conduction due to normal mode mixing (off-diagonal components). Mathematically this is expressed by considering the heat flux and thermal conductivity as a matrix [Fig. 3(b)] with diagonal elements describing phonon modes conducting heat as propagating wave packets (phonon-gas channel) and the non-diagonal elements describing phonons conducting energy diffusely through normal mode mixing (diffuson channel). In relatively simple crystals that are not significantly anharmonic, Hardy correctly argued that the non-diagonal contributions will be negligible compared to the diagonal contributions.

Decades later, Allen and Feldman[153,154] studied amorphous Si and $\mathrm{Si_xGe_{1-x}}$, by considering the harmonic interatomic forces of a relaxed amorphous-like unit cell structure that obeyed periodic boundary conditions. Therefore, phonon mode decomposition could be applied. However, their structure contained up to 1000 atoms per unit cell and so the phonon band structure can be considered an extreme case of band folding [green box in Fig. 3(a)], such that the Brillouin zone integration could be performed by sampling a single **q**-point (Γ).

The extension of Allen and Feldman's methodology to explore the vibrational character of crystalline solids has been a development over the last decade.[155,156] The ability to quantify the vibrational character of a particular phonon mode has seen marked improvements from the simple participation ratio metric used by Allen and Feldman.[11] The basic classification scheme is to use the spatial correlation of phonon eigenvectors for each vibrational mode. Propagaons, which correspond to the typical picture of a cyclic spatial displacement field defined by the wavevector, have eigenvectors that are highly correlated throughout all atoms in the solid. Diffusons represent phonon modes that are also extended across many atoms, but each atom vibrates in a different direction (defined by the eigenvector) that may even appear random. This is why the wavevector is no longer a reasonable descriptor for these vibrations. Locons are phonons that are spatially localized, which is to say that these are movements of an atom (or a few atoms) that are essentially uncorrelated with the movement of its neighbors.

From both molecular dynamics simulations (e.g., using Green-Kubo modal analysis[25]) and lattice dynamics calculations[15,16,157,158] it has been possible to quantify the relative contributions of the phonon gas and diffuson channels to thermal conductivity. There have also been various constructions of two-channel thermal transport models from analytical theories.[30,53,159–162]

In the lattice dynamics formalism, the diffuson thermal conductivity can be written as

$$\kappa_{\rm diff} = \sum_{\mathbf{q}ss'}^{s\neq s'} C_{ss'}(\mathbf{q}) v_{ss'}(\mathbf{q}) v_{s's}(\mathbf{q}) \tau_{ss'}(\mathbf{q}), \tag{56}$$

which describes the transfer of thermal energy C between two vibrational modes s and s' at a specific $\mathbf{q}$. In general, however, coupling between modes at different $\mathbf{q}$ may also be considered.[29] The velocity matrices v determine the rate of energy transfer and depend on the eigenvectors of the two modes such that $v_{ss'} = 0$ if s and s' are perfectly orthogonal [Eq. (A11)]. The lifetime matrix $\tau_{ss'}$ determines the extent to which the modes overlap in phase space and energy, and depends on the phonon lifetime of each mode and the energetic difference between the two modes [Eq. (A14)]. Intuitively, it makes sense for modal interactions to be stronger when they have similar mode shapes (eigenvectors) and energies, and this is reflected in the form of $v_{ss'}$ and $\tau_{ss'}$.

There is tremendous potential to leverage MD and two-channel LD techniques in materials design. However, more experimental and computational experiments are required to guide intuition and uncovered design principles. Currently the predictive design of vibrational character through composition, defects, and materials processing is in its infancy. Mechanisms to reduce thermal conductivity often result in a larger proportion of diffuson-channel conduction. It is known that this can be accomplished by disordering the atomic structure (e.g., amorphous materials[27]) and is also expected for materials with high anharmonicity.[15] To further reduce thermal conductivity, however, it is desirable to reduce transport within the diffuson channel itself. This may be accomplished by increasing the spectral distribution of modes and isolating them energetically as identified in a recent study on $Yb_{14}(Mn,Mg)Sb_{11}$.[29] The development of other design paradigms for the diffuson channel will be crucial for next generation ultralow thermal conductivity materials. Additionally, the impact of vibrational character, and its relationship with ionic transport in solids, is mostly unexplored and is an entirely new direction of research.[163,164]

AUTHORS' CONTRIBUTIONS

R.H. led authorship and drafted the initial version of the manuscript. Authorship of Sec. V was led by R.G. All authors provided valuable feedback when revising the manuscript. Each section will be listed with ordered contributions from the authors. Sec. I: R.H. and S.G.; Sec. II: R.H., L.L., and G.J.S.; Sec. III: R.H., L.L., and G.J.S.; Sec. IV: R.H., R.G., and M.T.A.; Sec. V: R.G., R.H., J.S., G.J.S., and S.G.; Sec. VI: M.T.A., R.H., and G.J.S. Appendixes: R.H., R.G., M.T.A., and L.L.

ACKNOWLEDGMENTS

R.H., J.S., and S.G. acknowledge the Air Force Office of Scientific Research MURI program (Grant No. FA9550-18-1-0479). R.G. and G.J.S. acknowledge the support of award 70NANB19H005 from the U.S. Department of Commerce, National Institute of Standards and Technology as part of the Center for Hierarchical Materials Design (CHiMaD). L.L. acknowledges support from the U.S. Department of Energy, Office of Science, Office of Basic Energy Sciences, Material Sciences and Engineering Division for thermal transport calculations and manuscript development. Computational resources were provided by the National Energy Research Scientific Computing Center (NERSC), a DOE Office of Science User Facility supported by the Office of Science of the U.S. Department of Energy under Contract No. DE-AC02-05CH11231.

APPENDIX A: LATTICE DYNAMICS

The basis of lattice dynamics starts with the crystal Hamiltonian H, which describes the energy of the system as the sum of the kinetic energy T and the potential energy U of all of the atoms in the crystal,

$$H = T + U. \tag{A1}$$

The kinetic energy of a single atom in a crystal on lattice site α moving in the Cartesian direction i is given by $m_\alpha(\dot{u}_i^\alpha)^2/2$. Here, m_α is the mass of the atom, u_i^α is the time varying atomic displacement vector, and $\dot{u}_i^\alpha$ is its velocity (the dot denotes the derivative with respect to time). The total kinetic energy is then given by summing over all lattice sites and directions,

$$T = \frac{1}{2}\sum_\alpha \sum_i m_\alpha (\dot{u}_i^\alpha)^2. \tag{A2}$$

The potential energy is treated as a Taylor expansion about the equilibrium atomic position ($u_i^\alpha = 0$) where the first non-trivial term is the harmonic potential energy

$$U = \frac{1}{2!}\sum_{\alpha\beta}\sum_{ij}\Phi_{ij}^{\alpha\beta}u_i^\alpha u_j^\beta + \frac{1}{3!}\sum_{\alpha\beta\gamma}\sum_{ijk}\Phi_{ijk}^{\alpha\beta\gamma}u_i^\alpha u_j^\beta u_k^\gamma + \cdots, \tag{A3}$$

or simply

$$U = U_{2\mathrm{nd}} + U_{3\mathrm{rd}} + \cdots. \tag{A4}$$

$\Phi_{ij}^{\alpha\beta}$ and $\Phi_{ijk}^{\alpha\beta\gamma}$ are second and third order derivatives of the potential energy with respect to atomic displacements and are often referred to as the second and third order interatomic force constants (IFCs). $\Phi_{ij}^{\alpha\beta}$ can be read as the force on atom α in the i direction when atom β is displaced in the j direction. $\Phi_{ijk}^{\alpha\beta\gamma}$ can be read as the force on atom α in the i direction when atoms β and γ are displaced in the j and k directions, respectively. These constants can be calculated using density functional theory (DFT) with various computational suites (VASP,[165] QuantumEspresso,[166] Phonopy[167]). Additionally, there are databases containing IFCs of many compounds to second and even third order.[168] It seems that for many materials treating U to 3rd order is sufficient.[4] In some very anharmonic materials and at high temperatures, fourth order IFCs can become important and play the role of renormalizing the phonon dispersion relation and opening up additional scattering phase space.[169–171]

For lowest order perturbation, the lattice Hamiltonian is

$$H = T + U_{2\mathrm{nd}} + U_{3\mathrm{rd}}. \tag{A5}$$

This expression, together with Eqs. (A2) and (A3), is useful when determining how a given defect will perturb phonons, and we will return to this when discussing phonon-defect scattering.

1. Harmonic vibrational states

Harmonic vibrational eigenstates (phonons) can be mathematically defined by solving the atomic equations of motion, assuming harmonic coupling between all atoms (read $F = m\ddot{x}$). These solutions are often visualized in a phonon dispersion relation [Fig. 4(a)], inverse wavelength or wavevector, q, vs energy, $\hbar\omega$ ($\hbar$ is the reduced Plank constant and ω is the phonon angular frequency). The phonon dispersion relation is, in essence, a Fourier transform of the interatomic force constants weighted by the atomic masses, and naturally contains information of lattice symmetries.

When H is taken to second order in U, the equation of motion can be written

$$-\sum_{j\beta}\Phi_{ij}^{\alpha\beta}u_j^\beta = \ddot{u}_i^\alpha m_\alpha, \tag{A6}$$

where the left-hand side is the force on atom α in the ith direction due to all atoms β being displaced in various directions j. The right-hand side is the mass of atom α times its acceleration in the ith direction. Equation (A6) can be solved by expressing u_i^α as a Fourier series in $\mathbf{q}$ space, obtaining plane wave solutions

$$u_i^\alpha = \frac{1}{\sqrt{m_\alpha}} \sum_{\mathbf{q}} A_{\mathbf{q}} \varepsilon_{i,\mathbf{q}}^\alpha e^{i(\mathbf{q}\cdot\mathbf{R}_\alpha - \omega t)}, \tag{A7}$$

and exploiting the translational symmetry of $\Phi_{ij}^{\alpha\beta}$. $A_{\mathbf{q}}$ is the amplitude of the atomic displacement and depends on temperature. $\mathbf{R}_\alpha$ is the vector pointing to the unit cell in which atom α resides. $\varepsilon_{i,\mathbf{q}}^\alpha$ is the 3×1 normalized displacement vector of atom α in the ith direction due to the mode $\mathbf{q}$. Later this information is repackaged into a $3N\times1$ normalized eigenvector (where N is the number of atoms in the unit cell), $\varepsilon_s(\mathbf{q})$. Plugging this into Eq. (A6) results in the so-called "dynamical matrix"

$$D_{ij}^{\alpha\beta}(\mathbf{q}) = \sum_{\mathbf{R}} \frac{\Phi_{ij}^{\alpha\beta}}{\sqrt{m_\alpha m_\beta}} e^{i\mathbf{q}\cdot\mathbf{R}}, \tag{A8}$$

where $\mathbf{R}$ the vector connecting the unit cells in which atom α and β reside. The diagonalization of $D_{ij}^{\alpha\beta}(\mathbf{q})$ can be expressed as

$$D(\mathbf{q})\varepsilon_s(\mathbf{q}) = \omega_s(\mathbf{q})^2 \varepsilon_s(\mathbf{q}), \tag{A9}$$

where $\omega_s(\mathbf{q})^2$ are the eigenvalues (mode energies), $\varepsilon_s(\mathbf{q})$ are the $3N \times 1$ eigenvectors (mode shapes), and $D(\mathbf{q})$ is the $3N \times 3N$ dynamical matrix with specific elements designated by a compound index αi and βj.

2. κ_{vib} from two-channel lattice dynamics

Here we describe computation of κ_{vib} via two-channel lattice dynamics, within a mode-specific DFT based approach. The two recently developed expressions, one derived by Isavea *et al.*[16] and one derived by Simoncelli *et al.*,[15] can both be expressed in the form

$$\kappa_{\text{vib}}^{ij} = \sum_{\mathbf{q}ss'} C_{ss'}(\mathbf{q}) v_{ss'}^i(\mathbf{q}) v_{s's}^j(\mathbf{q}) \tau_{ss'}(\mathbf{q}). \tag{A10}$$

Isaeva *et al.* define terms explicitly in this form, and the reader is referred to Eq. 9 of Ref. 16. Here, we cast the theory provided by Simoncelli *et al.* into the same form as Eq. (A10). The quantity contained within the sum can be thought of as a matrix with rows and columns designating the mode index, s and s' [Fig. 3(b)] at a given $\mathbf{q}$. The diagonal elements sum together giving the phonon-gas channel κ_{pg} [Eq. (B1)].

The velocity matrix can be written as a matrix element containing the gradient of the dynamical matrix, which is commonly used to compute the phonon-gas channel group velocity

$$v_{ss'}^i(\mathbf{q}) = \frac{1}{\omega_s(\mathbf{q}) + \omega_{s'}(\mathbf{q})} \langle \mathbf{q}s | \nabla_{\mathbf{q}}^i D(\mathbf{q}) | \mathbf{q}s' \rangle, \tag{A11}$$

by using Eqs. (8) and (30) of Simoncelli *et al.*[15] and Eq. (4) of Auerbach and Allen.[31] $v_{ss'}^i(\mathbf{q})$ is a complex matrix that obeys the relationship $v_{ss'}(\mathbf{q}) = v_{s's}(\mathbf{q})^*$. For the diagonal elements, $s = s'$, this reduces to the common group velocity $v_{ss}^i(\mathbf{q}) = v_s^i(\mathbf{q}) = \frac{\partial \omega_s(\mathbf{q})}{\partial k_i}$.

The matrix element can be written explicitly as

$$\langle \mathbf{q}s | \nabla_{\mathbf{q}}^i D(\mathbf{q}) | \mathbf{q}s' \rangle = \varepsilon_s^*(\mathbf{q}) \frac{\partial D(\mathbf{q})}{\partial k_i} \varepsilon_{s'}(\mathbf{q}), \tag{A12}$$

where $\varepsilon_s(\mathbf{q})$ is the eigenvector of normal mode at $\mathbf{q}$ in branch s. The star indicates a complex conjugate.

The heat capacity matrix, in units of J m^{-3}K^{-1} is given as[15]

$$C_{ss'}(\mathbf{q}) = \frac{\hbar^2(\omega_s(\mathbf{q}) + \omega_{s'}(\mathbf{q}))}{4V_{\text{UC}}N_{\mathbf{q}}k_{\text{B}}T^2} \left[\omega_s(\mathbf{q}) n_s^{\text{o}}(\mathbf{q})(n_s^{\text{o}}(\mathbf{q}) + 1) + \omega_{s'}(\mathbf{q}) n_{s'}^{\text{o}}(\mathbf{q})(n_{s'}^{\text{o}}(\mathbf{q}) + 1)\right], \tag{A13}$$

where $n_s^{\text{o}}(\mathbf{q}) = (\exp(\hbar\omega/k_{\text{B}}T) - 1)^{-1}$ is the Bose-Einstein distribution function of mode $\mathbf{q}s$ at temperature T, $\omega_s(\mathbf{q})$ is the phonon angular frequency of a phonon at wave vector $\mathbf{q}$ in branch s, V_{UC} is the volume of the unit cell, and $N_{\mathbf{q}}$ is the number of $\mathbf{q}$-points considered on a discrete, uniform $\mathbf{q}$-mesh.

The lifetime matrix is given by[15]

$$\tau_{ss'}(\mathbf{q}) = \frac{2(\Gamma_s(\mathbf{q}) + \Gamma_{s'}(\mathbf{q}))}{4(\omega_s(\mathbf{q}) - \omega_{s'}(\mathbf{q}))^2 + (\Gamma_s(\mathbf{q}) + \Gamma_{s'}(\mathbf{q}))^2}, \tag{A14}$$

where $\Gamma_s(\mathbf{q})$ is the scattering rate or the inverse of phonon lifetime for a phonon at q in branch s. For off-diagonal elements, this equation resembles a Lorentzian function. For the diagonal components, it reduces to the phonon relaxation time

$$\tau_{ss}(\mathbf{q}) = \Gamma_s(\mathbf{q})^{-1} = \tau_s(\mathbf{q}). \tag{A15}$$

APPENDIX B: MODELS FOR κ_{pg}

1. Mode specific

The phonon-gas channel is given as the sum of the diagonal components of the vibrational thermal conductivity matrix [Eq. (A10), with $s = s'$]

$$\kappa_{\text{pg}}^{ij} = \sum_{\mathbf{q}s} C_s(\mathbf{q})\, v_s^i(\mathbf{q})\, v_s^j(\mathbf{q})\, \tau_s(\mathbf{q}). \tag{B1}$$

$C_s(\mathbf{q})$ is the heat capacity of the phonon mode $\mathbf{q}s$, dropping the redundant branch subscript in Eq. (A13) [$C_s(\mathbf{q}) = C_{ss}(\mathbf{q})$],

$$C_s(\mathbf{q}) = \frac{\hbar^2 \omega_s^2(\mathbf{q})}{V_{\text{UC}} N_{\mathbf{q}} k_{\text{B}} T^2} \left[n_s^{\text{o}}(\mathbf{q})(n_s^{\text{o}}(\mathbf{q}) + 1)\right]. \tag{B2}$$

$v_s^i(\mathbf{q}) = d\omega_s(\mathbf{q})/dq_i$ is the component of the phonon group velocity vector pointing in the i direction. $\tau_s(\mathbf{q})$ is the lifetime of the phonon, or its time between collisions.

2. Spectral

Depending on the complexity of the system of interest, it may be desirable or necessary to work with spectral models for κ_{pg} where each phonon property is expressed as a function of frequency, ω, rather than mode-specific models where each mode $\mathbf{q}s$ in the Brillouin zone is considered independently. However, it is important to understand how mode-specific and spectral models are related, particularly when constructing multi-scale thermal transport models. In this section, we start with a mode-specific treatment [Eq. (B1)] and demonstrate how it can be reduced to a spectral model [Eq. (4)]. Additionally, we summarize common analytical expressions for the dispersion relation, heat capacity, and phonon-phonon relaxation time.

a. From mode-specific data

The quantities present in Eq. (B1) can be readily computed using *ab initio* based lattice dynamics, and the results for a perfect, infinite (i.e., no crystal boundary scattering) Si crystal are shown in Figs. 4(a), 4(c), and 4(e).

In Eq. (B1), we define the spectral phonon heat capacity as

$$C(\omega) = \sum_{\mathbf{q}s} C_s(\mathbf{q})\delta(\omega - \omega_s(\mathbf{q})), \tag{B3}$$

and the average group velocity and relaxation time at a given frequency

$$v_g(\omega) = \frac{\sum_{\mathbf{q}s} v_s(\mathbf{q})\delta(\omega - \omega_s(\mathbf{q}))}{\sum_{\mathbf{q}s} \delta(\omega - \omega_s(\mathbf{q}))}, \tag{B4}$$

$$\tau(\omega) = \frac{\sum_{\mathbf{q}s} \tau_s(\mathbf{q})\delta(\omega - \omega_s(\mathbf{q}))}{\sum_{\mathbf{q}s} \delta(\omega - \omega_s(\mathbf{q}))}. \tag{B5}$$

Note that by omitting the Cartesian index in $v_s(\mathbf{q})$ we are implicitly referring to the magnitude of the group velocity of phonon mode $\mathbf{q}s$. Since

$$\sum_{\mathbf{q}s} \delta(\omega - \omega(\mathbf{q}s)) = g(\omega), \tag{B6}$$

is the phonon density of states (pDOS), Eqs. (B4) and (B5) are simply pDOS weighted averages of $v_s(\mathbf{q})$ and $\tau_s(\mathbf{q})$. There are several ways to execute Eqs. (B4) and (B5) computationally. In Fig. (4) the δ-functions are approximated as Gaussian distributions using uniform Brillouin zone mesh sampling.

b. From dispersion relation approximations

We now wish to reduce the mode-specific model given in Eq. (B1) into a spectral model given in Eq. (4), which can be computed using dispersion relations and semi-empirical expressions for τ.

We will examine the $ij = zz$ component and for brevity consider three degenerate branches. Therefore, we introduce a factor of 3 and drop the s subscript. We start by converting the sum over $\mathbf{q}$ into an integral

$$\kappa_{\text{pg}}^{zz} = \iiint 3c(\mathbf{q})\, v_g^z(\mathbf{q})^2\, \tau(\mathbf{q}) \frac{d^3\mathbf{q}}{(2\pi)^3}, \tag{B7}$$

where $c(\mathbf{q}) = k_B x^2[n(n+1)], n = (\exp(x) - 1)^{-1}$, and $x = \hbar\omega/(k_B T)$. The lower case $c(\mathbf{q})$ is essentially the same as $C_s(\mathbf{q})$ in Eq. (B2) except that has units of J/K instead of $\text{J/(Km}^3)$ since the reciprocal space volume element is now carried by $d^3\mathbf{q}/(2\pi)^3$ instead of the factor $1/(V_{\text{UC}} N_{\mathbf{q}})$. The integral is then converted to spherical coordinates

$$\kappa_{\text{pg}}^{zz} = \int_0^{q_{\max}(\theta,\phi)} \int_0^{2\pi}\int_0^{\pi} \frac{3c(\mathbf{q})}{(2\pi)^3} v_g^z(\mathbf{q})^2\, \tau(\mathbf{q}) q^2 \sin(\theta) d\theta d\phi dq. \tag{B8}$$

To reduce this down to a single integral over ω, the θ and ϕ dependence of frequency and the group velocity at a given $q = |\mathbf{q}|$ are averaged into a single isotropic value. The maximum wavevector $q_{\max} = (6\pi^2/(NV_{\text{UC}}))^{1/3}$ is obtained by defining a sphere with the same volume as the FBZ. This results in a simplification of Eq. (B8) as

$$\kappa_{\text{pg}}^{zz} = \int_0^{q_{\max}} \frac{3c(\mathbf{q})q^2}{(2\pi)^3} v_g(q)^2 \left[\int_0^{2\pi}\int_0^{\pi} \tau(\mathbf{q}) \cos(\theta)^2 \sin(\theta) d\theta d\phi\right] dq. \tag{B9}$$

We have represented $v_g^z(\mathbf{q})$ as $v_g(q)\cos\theta$, where by dropping the Cartesian index superscript we imply that $v_g(q)$ is the average magnitude of the group velocity vector at q. It is convenient to define a weighted orientational average of $\tau(\mathbf{q})$ as (ij correspond to the Cartesian indices in κ_{pg}^{ij})

$$\tau(q) = \frac{\iint \tau(\mathbf{q}) \frac{q_i q_j}{q^2} \sin(\theta) d\theta d\phi}{\iint \frac{q_i q_j}{q^2} \sin(\theta) d\theta d\phi}, \tag{B10}$$

which for the zz direction is

$$\tau(q) = \frac{\iint \tau(\mathbf{q}) \cos(\theta)^2 \sin(\theta) d\theta d\phi}{\iint \cos(\theta)^2 \sin(\theta) d\theta d\phi}, \tag{B11}$$

giving

$$\int_0^{2\pi}\int_0^{\pi} \tau(\mathbf{q}) \cos(\theta)^2 \sin(\theta) d\theta d\phi = \frac{4\pi}{3}\tau(q). \tag{B12}$$

Plugging this into Eq. (B9) gives

$$\kappa_{\text{pg}}^{zz} = \frac{1}{3}\int_0^{q_{\max}} \frac{3c(\mathbf{q})q^2}{2\pi^2} v_g(q)^2\, \tau(q) dq. \tag{B13}$$

Using the definitions of group velocity $v_g = d\omega/dq$ and phase velocity $v_p = \omega/q$, and defining the spectral heat capacity [in units of $\text{Js/(Km}^3)$]

$$C(\omega) = \frac{3}{2\pi^2} \frac{\omega^4}{v_g(\omega) v_p(\omega)^2} \frac{\hbar^2}{k_B T^2} \frac{e^{\hbar\omega/k_B T}}{(e^{\hbar\omega/k_B T} - 1)^2}, \tag{B14}$$

we can convert the variable of integration from q to ω,

$$\kappa_{\text{pg}}^{zz} = \frac{1}{3}\int_0^{\omega_{\max}} C(\omega)\, v_g(\omega)^2\, \tau(\omega) d\omega. \tag{B15}$$

The Cartesian superscripts are omitted in Eq. (4).

3. Dispersion relation approximations

The Debye approximation simply assumes all phonons have a group velocity equal to the material's speed of sound v_S. It is common to also make the isotropic approximation, such that the speed of sound used is the isotropic speed of sound and ω is therefore only a function of the magnitude of $\mathbf{q}$,

$$\omega(q) = v_S q, \quad \text{for } 0 < q < q_{\max}, \tag{B16}$$

where $q_{\max} = (6\pi^2/(NV_{\text{at}}))^{1/3}$ and $\omega_{\max} = 2v_S q_{\max}/\pi$. Another common dispersion approximation is the Born-von Karman dispersion relation

$$\omega(q) = \omega_{\max} \sin\left(\frac{\pi q}{2q_{\max}}\right). \tag{B17}$$

Here, V_{at} is the volume per atom, and N is the number of atoms in the primitive unit cell. Since $q_{\max}$ is determined using the volume of the primitive unit cell ($V_{\text{at}}N$), this thermal transport model only considers acoustic phonons. If V_{at} is substituted for $V_{\text{at}}N$ in the equation for $q_{\max}$, the number of modes considered in the model equals total number of vibrational modes, acoustic plus optical. Equations (B16) and (B17) can be used to compute the group velocity ($v_g = d\omega/dq$) and phase velocity $v_p = \omega/q$.

4. Phonon-gas thermal conductivity at high-T

Here we solve for an analytical expression for the phonon thermal conductivity at high-T. The spectral heat capacity given in Eq. (B14), at high temperatures ($T > \theta_D$) becomes

$$C(\omega) = \frac{3k_B\omega^2}{2\pi^2 v_g v_p^2}. \tag{B18}$$

A widely used expression for phonon-phonon scattering at high temperatures is[52–54,172]

$$\tau_{\text{pp}} = \left(\frac{6\pi^2}{V}\right)^{1/3} \frac{\bar{M} v_g v_p^2}{2k_B\gamma^2\omega^2 T}, \tag{B19}$$

where $\bar{M}$ and V are the average atomic mass and volume, and γ is the Grüneisen parameter. With Eqs. (B18) and (B19), assuming phonon-phonon scattering dominates ($\tau = \tau_{\text{pp}}$), Eq. (4) becomes

$$\kappa_{\text{ph}} = \left(\frac{6\pi^2}{V}\right)^{1/3} \frac{\bar{M}}{4\pi^2\gamma^2 T} \int_0^{\omega_{\max}} v_g^2\, d\omega. \tag{B20}$$

Notice that the factors of $v_g v_p^2$ in Eqs. (B18) and (B19) cancel, leaving only v_g^2 in the integral over ω. By switching the variable of integration from ω to q, we can observe the cubic dependence of κ_{ph} on the phonon velocity

$$\int_0^{\omega_{\max}} v_g^2\, d\omega = \int_0^{q_{\max}} v_g^3\, dq. \tag{B21}$$

Therefore, it is useful to define an average v_g^3 throughout the Brillouin zone

$$\langle v_g^3 \rangle = \frac{1}{q_{\max}} \int_0^{q_{\max}} v_g^3\, dq, \tag{B22}$$

where $q_{\max} = (6\pi^2/V_{\text{UC}})^{1/3}$. With this definition, Eq. (B20) becomes

$$\kappa_{\text{ph}} = \left(\frac{6\pi^2}{V_{\text{UC}}}\right)^{2/3} \frac{\bar{M}}{4\pi^2\gamma^2} \frac{\langle v_g^3 \rangle}{T}. \tag{B23}$$

In exploring the possibility of softening effects, it is commonly asserted that $\langle v_g^3 \rangle \propto v_S^3$ for acoustic branches, which is rigorously true in the Debye and Born von Karman approximations. The prefactors are then combined into the parameter

$$A = \left(\frac{6\pi^2}{V_{\text{UC}}}\right)^{2/3} \frac{\bar{M}}{4\pi^2\gamma^2}, \tag{B24}$$

which is commonly calibrated to a given material system using a control sample, giving

$$\kappa_{\text{ph}} = A\frac{v_S^3}{T}. \tag{B25}$$

APPENDIX C: DETAILS FOR SI PERFECT CRYSTAL EXAMPLE

The phonon energy, group velocity, and relaxation times in Figs. 4(d) and 4(e) were sampled on a dense $30 \times 30 \times 30$ uniform q-mesh throughout the Brillouin zone. The length of the horizontal dash-type data points in Fig. 4(a) visually represent the resolution of q-meshing. Keep in mind that $\tau_s(\mathbf{q})$ is not defined at the Γ-point ($\mathbf{q} = 0$) and is set to zero. Therefore, the Brillouin zone integration is approximated by a q-mesh sampling procedure where the lower bound is not computed. The interatomic force constants (IFCs) used for Fig. 4 and Figs. 6(a) and 6(b) were obtained from the almaBTE database.[168] Thermal conductivity accumulation calculations presented in Fig. 6(c) used Si harmonic IFCs from Ref. 173 with Gaussian quadrature sampling of the Brillouin zone in Cartesian coordinates and separately in spherical coordinates with similar number of integration sampling points.

APPENDIX D: ELASTIC DEFECT SCATTERING

In this section, we derive analytical expressions for phonon scattering off of a perturbation H' to the harmonic lattice Hamiltonian $H^0 = T + U_{\text{2nd}}$, where the total Hamiltonian is given as $H = H^0 + H'$. For intrinsic phonon-phonon scattering, H' comes from anharmonic terms in the interatomic potential (e.g., U_{3rd}). For phonon defect scattering, it is common to represent the perturbation as a spatially varying scattering potential function $V(\mathbf{r})$, which can be understood as perturbing H through T (atomic mass or density fluctuations), U_{2nd} (fluctuations in elastic constants or IFCs), and/or U_{3rd} (strain fields). The probability of scattering per unit time of a phonon is given by Fermi's Golden Rule as[174]

$$W_{\mathbf{q},\mathbf{q}'} = \frac{2\pi}{\hbar}|\langle f|H'|i\rangle|^2\delta(\Delta E). \tag{D1}$$

For elastic defect scattering, an incident phonon $\mathbf{q}$ interacts with the defect and scatters into $\mathbf{q}'$ of the same energy. Therefore, the initial state in Eq. (D1) is simply a phonon in state $\mathbf{q}$, $|i\rangle = |\mathbf{q}\rangle$, and the final is one in state $\mathbf{q}'$, $|f\rangle = |\mathbf{q}'\rangle$. The change in energy of the system is then given by $\Delta E = E_{\mathbf{q}} - E_{\mathbf{q}'}$, where $E_{\mathbf{q}} = \hbar\omega_{\mathbf{q}}$ is the energy of a phonon with wavevector $\mathbf{q}$. For simplicity, we suppress phonon branch index, since that does not affect the central point of our argument, which can be seen by thinking of the perturbation in terms of a scattering potential $V(\mathbf{r})$. In Appendices A 1–A 3, we will derive $V(\mathbf{r})$ from the real-space lattice perturbation induced by point, line, and planar defects. For these examples, it is convenient to think of the crystal as a rectilinear brick with sides L_x, L_y, L_z in the x, y, and z directions with volume $L_xL_yL_z$. The matrix element can then be calculated from $V(\mathbf{r})$ by performing a Fourier transform [see Eq. (12)]. Prior to discussing these elastic scattering processes, it is also convenient to introduce the scattering vector

$$\mathbf{Q} = \mathbf{q}' - \mathbf{q}. \tag{D2}$$

The object of ultimately greater interest than the scattering probability is the phonon relaxation time, $\tau(\mathbf{q})$, and its inverse the phonon scattering rate, $\Gamma(\mathbf{q}) = \tau(\mathbf{q})^{-1}$. To find these, we must integrate $W_{\mathbf{q},\mathbf{q}'}$ over all possible final phonon wavevectors. In the definition of the relaxation time, a forward scattering suppression factor $(1 - \hat{\mathbf{q}}\cdot\hat{\mathbf{q}}')$ is introduced into the integral over $\mathbf{q}'$, with $\hat{\mathbf{q}}$ and $\hat{\mathbf{q}}'$ being unit vectors parallel to $\mathbf{q}$ and $\mathbf{q}'$. Its presence can be appreciated by considering the forward scattering process where $\mathbf{q} = \mathbf{q}'$. Such a transition has no consequence to the system, so forward scattering contributions to $\Gamma(\mathbf{q})$ are suppressed via the presence of $(1 - \hat{\mathbf{q}}\cdot\hat{\mathbf{q}}')$. (See page 326 of Ashcroft and Mermin[174] for more details on the forward scattering suppression factor.) Therefore, we have

$$\Gamma(\mathbf{q}) = L_xL_yL_z \iiint \frac{d^3\mathbf{q}'}{(2\pi)^3} W_{\mathbf{q},\mathbf{q}'}(1 - \hat{\mathbf{q}}\cdot\hat{\mathbf{q}}'). \tag{D3}$$

The role of the dimensionality of the scattering defect can now be addressed. It is useful to discuss the different dimensionalities separately and begin in the middle with a linear defect, $d_{\mathrm{d}} = 1$.

1. One-dimensional defects

Suppose the defect is a linear object parallel to the z direction, so that

$$V(\mathbf{r}) = V(x, y) \tag{D4}$$

is a function only of x and y. The position integral in the matrix element then simplifies to

$$\iiint d^3\mathbf{r}\, V(x,y)e^{-i\mathbf{Q}\cdot\mathbf{r}} = 2\pi\delta(Q_z)\iint dx\,dy\, V(x,y)e^{-i(Q_xx+Q_yy)}, \tag{D5}$$

and invoking well established rules for interpreting the square of a δ-function

$$\delta^2(Q_i) = \frac{L_i\delta(Q_i)}{2\pi}, \tag{D6}$$

we find a scattering probability

$$W_{\mathbf{q},\mathbf{q}'} = \frac{2\pi}{\hbar}\frac{L_z}{(L_xL_yL_z)^2}|M_{2\mathrm{d}}|^2 \times (2\pi)\delta(Q_z)\delta(E_{\mathbf{q}'} - E_{\mathbf{q}}), \tag{D7}$$

where we have defined a reduced matrix element,

$$M_{2\mathrm{d}} = \iint dx\,dy\, V(x,y)e^{-i(Q_xx+Q_yy)}, \tag{D8}$$

where the subscript "2d" indicates that the integral is two-dimensional. With $n_{2\mathrm{d}} = (L_xL_y)^{-1}$ defined as the areal density of non-interacting linear defects,

$$\Gamma(\mathbf{q}) = \frac{n_{2\mathrm{d}}}{2\pi\hbar}\iiint d^3\mathbf{q}'\,|M_{2\mathrm{d}}(Q_x,Q_y)|^2(1 - \hat{\mathbf{q}}\cdot\hat{\mathbf{q}}')\delta(Q_z)\delta(E_{\mathbf{q}'} - E_{\mathbf{q}}). \tag{D9}$$

The two δ-functions in the integral now represent conservation of energy and wavevector parallel to the defect. Therefore, scattering from a defect of this type is specular in the z-direction, $Q_z = q_z' - q_z = 0$. We can see this by assuming an isotropic phonon spectrum, $E_{\mathbf{q}} = E_q = \hbar\omega_q$, in which the energy $E_{\mathbf{q}}$ depends on $q = |\mathbf{q}|$ only. With the phonon group and phase velocities defined as

$$v_{\mathrm{g}}(q) = \frac{\partial\omega_q}{\partial q}, \quad v_{\mathrm{p}}(q) = \frac{\omega_q}{q}, \tag{D10}$$

we get

$$\delta(E_{q'} - E_q) = \frac{1}{\hbar|v_{\mathrm{g}}(q)|}\delta(q - q'). \tag{D11}$$

Beginning here, we will omit the absolute value sign around v_{g} as the group velocity is always positive for our treatment. However, real phonon dispersion relations can have a negative v_{g} and in this case the absolute value is required. We stress that the assumption of isotropy in no way diminishes the generality of the dimensional arguments, and is made so as to not encumber the analysis with inessential detail. In spherical polar coordinates, the second δ-function [in conjunction with $\delta(q - q')$] reads

$$\delta(Q_z) = \delta(q\cos\vartheta - q'\cos\vartheta') = \frac{1}{q}\delta(\cos\vartheta - \cos\vartheta'). \tag{D12}$$

The conservation laws are equivalent to $q' = q$ and $\vartheta' = \vartheta$. Further, $d^3\mathbf{q}' = q'^2\sin\theta' dq'\,d\theta'd\phi'$. The integrals over q' and ϑ' can be done trivially because of the δ-functions, and we obtain

$$\Gamma(\mathbf{q}) = \frac{n_{2\mathrm{d}}\omega_q}{2\pi v_{\mathrm{g}}v_{\mathrm{p}}\hbar^2}\int_0^{2\pi} d\varphi'\,|M_{2\mathrm{d}}(Q_x,Q_y)|^2(1 - \hat{\mathbf{q}}\cdot\hat{\mathbf{q}}'). \tag{D13}$$

The two-dimensional phonon density of states is

$$g_{2\mathrm{d}}(\omega) = \frac{\omega}{2\pi v_{\mathrm{g}}(\omega)v_{\mathrm{p}}(\omega)}, \tag{D14}$$

and if we define the average squared matrix element as

$$\overline{|M_{2\mathrm{d}}|^2} = \frac{1}{\hbar^2}\int_0^{2\pi} d\varphi'\,|M_{2\mathrm{d}}(Q_x,Q_y)|^2(1 - \hat{\mathbf{q}}\cdot\hat{\mathbf{q}}'), \tag{D15}$$

we get the result quoted in Eq. (1), i.e.,

$$\Gamma(\mathbf{q}) = n_{2\mathrm{d}}g_{2\mathrm{d}}(\omega_k)\overline{|M_{2\mathrm{d}}|^2} \quad \text{(linear defect)}. \tag{D16}$$

For the evaluation of $\overline{|M_{2\mathrm{d}}|^2}$ it is useful to keep in mind that

$$\begin{aligned} Q_x &= q\sin\vartheta(\cos\varphi' - \cos\varphi),\\ Q_y &= q\sin\vartheta(\sin\varphi' - \sin\varphi),\\ (1-\hat{\mathbf{q}}\cdot\hat{\mathbf{q}}') &= 2\sin^2\vartheta\sin^2\frac{1}{2}(\varphi'-\varphi). \end{aligned} \tag{D17}$$

2. Zero-dimensional defects

For a zero-dimensional or point defect, the potential

$$V(\mathbf{r}) = V(x,y,z) \tag{D18}$$

depends on all three coordinates, and there is no simplification in the matrix element. We write this matrix element as

$$M_{3\mathrm{d}}(\mathbf{Q}) = \iiint d^3r\, V(\mathbf{r})e^{-i\mathbf{Q}\cdot\mathbf{r}}, \tag{D19}$$

where the subscript indicates a three-dimensional integral. Then,

$$W_{\mathbf{q},\mathbf{q}'} = \frac{2\pi}{\hbar}\frac{1}{(L_xL_yL_z)^2}|M_{3\mathrm{d}}|^2\delta(E_{\mathbf{q}'}-E_{\mathbf{q}}), \tag{D20}$$

and, with $n_{3\mathrm{d}} = (L_xL_yL_z)^{-1}$ defined as the (volumetric) density of point defects,

$$\Gamma(\mathbf{q}) = \frac{n_{3\mathrm{d}}}{(2\pi)^2\hbar}\iiint d^3\mathbf{q}'\,|M_{3\mathrm{d}}(\mathbf{Q})|^2(1-\hat{\mathbf{q}}\cdot\hat{\mathbf{q}}')\delta(E_{\mathbf{q}'}-E_{\mathbf{q}}). \tag{D21}$$

If we once again take an isotropic phonon spectrum, and employ spherical polar coordinates, the integral over the magnitude $q = |\mathbf{q}|$ can be done,

$$\Gamma(\mathbf{q}) = \frac{n_{3\mathrm{d}}\omega_k^2}{4\pi^2 v_{\mathrm{g}}v_{\mathrm{p}}^2\hbar^2}\int d\Omega'\,|M_{3\mathrm{d}}(\mathbf{Q})|^2(1-\hat{\mathbf{q}}\cdot\hat{\mathbf{q}}'), \tag{D22}$$

where $d\Omega' = \sin\vartheta' d\vartheta'\,d\varphi'$. The three-dimensional phonon density of states is

$$g_{3\mathrm{d}}(\omega) = \frac{\omega^2}{2\pi^2 v_{\mathrm{g}}(\omega)v_{\mathrm{p}}^2(\omega)}, \tag{D23}$$

and if we define the average squared matrix element as

$$\overline{|M_{3\mathrm{d}}|^2} = \frac{1}{2\hbar^2}\int d\Omega'\,|M_{3\mathrm{d}}(\mathbf{Q})|^2(1-\hat{\mathbf{q}}\cdot\hat{\mathbf{q}}'), \tag{D24}$$

we get the result cast into the form of Eq. (11),

$$\Gamma(\mathbf{q}) = n_{3\mathrm{d}}g_{3\mathrm{d}}(\omega_k)\overline{|M_{3\mathrm{d}}|^2} \quad \text{(point defect)}. \tag{D25}$$

This time, there is no useful simplification for the arguments of the functions in the integrand for $|M_{3\mathrm{d}}|^2$, and

$$\begin{aligned} \mathbf{Q} &= \mathbf{q}' - \mathbf{q},\\ \mathbf{q} &= q(\sin\vartheta\cos\varphi,\ \sin\vartheta\sin\varphi,\ \cos\vartheta),\\ \mathbf{q}' &= q(\sin\vartheta'\cos\varphi',\ \sin\vartheta'\sin\varphi',\ \cos\vartheta'). \end{aligned} \tag{D26}$$

3. Two-dimensional defects

We now consider a two-dimensional or planar defect parallel to the yz plane. Then

$$V(\mathbf{r}) = V(x) \tag{D27}$$

depends on x only. As a result, both q_y and q_z are conserved in addition to E_q, and there are only two possibilities for the final state wavevector:

$$q'_x = \pm q_x, \quad q'_y = q_y, \quad q'_z = q_z, \tag{D28}$$

corresponding to forward scattering and specular reflection. Only the latter contributes to limiting the life time, and we get

$$\Gamma(\mathbf{q}) = \frac{n_{1\mathrm{d}}}{\hbar^2 v_{\mathrm{g}}}\left[|M_{1\mathrm{d}}(Q_x)|^2(1-\hat{\mathbf{q}}\cdot\hat{\mathbf{q}}')\right]_{Q_x=-2q_x}. \tag{D29}$$

Here $n_{1\mathrm{d}} = L_x^{-1}$ is the density of planar defects,

$$g_{1\mathrm{d}} = \frac{1}{\pi v_{\mathrm{g}}} \tag{D30}$$

is the one-dimensional phonon density of states, and

$$M_{1\mathrm{d}}(Q_x) = \int dx\, V(x)e^{-iQ_x x}. \tag{D31}$$

To cast the answer into the form of Eq. (11),

$$\Gamma(\mathbf{q}) = n_{1\mathrm{d}}g_{1\mathrm{d}}(\omega_q)\overline{|M_{1\mathrm{d}}|^2} \quad \text{(planar defect)} \tag{D32}$$

we define

$$\overline{|M_{1\mathrm{d}}|^2} = \frac{\pi}{\hbar^2}\left[|M_{1\mathrm{d}}(Q_x)|^2(1-\hat{\mathbf{q}}\cdot\hat{\mathbf{q}}')\right]_{Q_x=-2q_x}. \tag{D33}$$

In this equation, one can also write the forward scattering suppression factor as

$$(1-\hat{\mathbf{q}}\cdot\hat{\mathbf{q}}') = \frac{2q_x^2}{q^2}. \tag{D34}$$

APPENDIX E: MEASUREMENTS OF THE SPEED OF SOUND AND DEBYE TEMPERATURE

1. Debye temperature

It is important to note the energy scale of phonons in a system. For reference, the maximum phonon frequency of Si is approximately 65 meV, where $k_{\mathrm{B}}T = 25$ meV at room temperature ($T = 300$ K). Therefore, all the phonons in Si will be significantly thermally populated at around 2.5 times room temperature. This is one intrinsic material property that the Debye temperature (θ_{D}) strives to quantify: the temperature at which all vibrations in a material are active ($\theta_{\mathrm{D}} = 660$ K in Si). There are many ways to measure and compute θ_{D}, and one should only directly compare the magnitude of θ_{D} values, which are determined by a consistent method. Several methods for quantifying θ_{D} are reviewed here. Important relations are

$$k_{\mathrm{B}}\theta_{\mathrm{D}} = \hbar\omega_{\mathrm{D}} = \hbar v_{\mathrm{S}}\left(\frac{6\pi^2}{V}\right)^{1/3}, \tag{E1}$$

where ω_{D} is the Debye frequency, v_{S} is the average speed of sound [Eq. (E2)], and V is the volume per atom. If the volume per unit cell

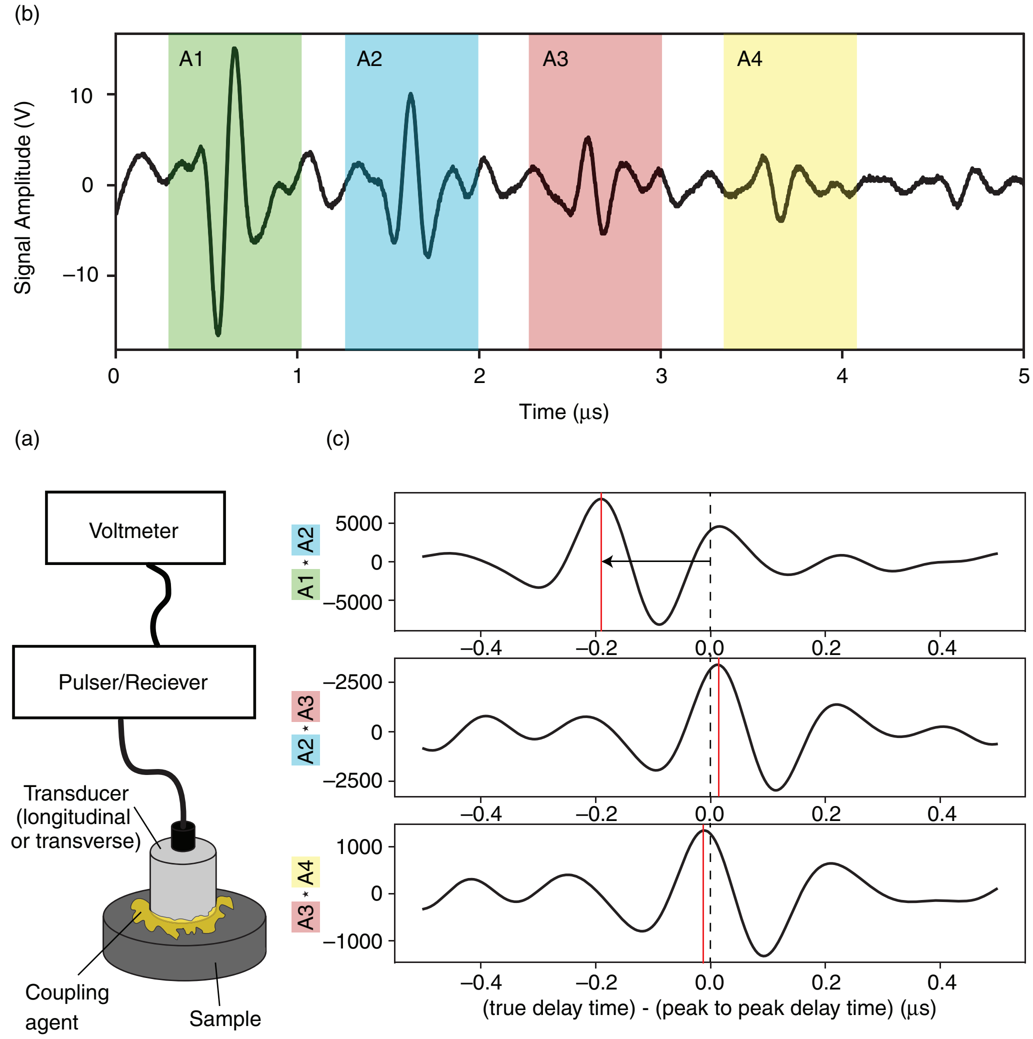

FIG. 15. Overview of pulse-echo ultrasound. (a) The experimental setup. (b) Example waveform. (c) Cross-correlation between successive reflections in the waveform.

is used for V instead, one might call this an "acoustic Debye temperature/frequency" since only acoustic modes are considered.

2. Pulse-echo ultrasound

The speed of sound in a material can be readily and accurately measured by a pulse-echo method where a piezoelectric transducer coupled to a sample sends an initial stress-wave pulse, and then acts as receiver measuring the echoed ultrasound reflection from the other side of the sample (Fig. 15).[175] When no preferred orientation is observed, say by X-ray analysis, randomly oriented polycrystals can be treated as elastically isotropic, particularly for dense samples with grain sizes sufficiently smaller than the ultrasonic wavelength. The time-delay, t_d, between subsequent reflections must be determined by maximizing the cross-correlation [Fig. 15(c)] of the two reflections as follows. If $A_n(t)$ is the amplitude of reflection n, then $\sum_t A_n(t)A_{n+1}(t-t_d)$ is maximized by varying t_d. This corresponding value of t_d along with the sample thickness, h, is then used to calculate the speed of sound, $v_{L,T} = 2h/t_d$. Table honey with low water content acts as a nice coupling agent for both longitudinal and transverse acoustic waves. Its viscoelastic properties make it surprisingly effective at transferring acoustic energy. Crystalbond or superglue can also be used. A typical waveform should contain over four reflections (3 time-delay measurements), and the measurements from a minimum of three waveforms (corresponding to 9 individual speed of sound measurements) can be averaged. Measurements having a standard deviation of less than 1% of the mean are common. The largest error in this technique is the measurement of the sample thickness, and if care is taken to ensure the sample faces are parallel and a micrometer is used to measure the sample thickness, <1% characterization related error is achievable. The average speed of sound that is commonly used for transport modeling is calculated as[98]

$$v_S = \left(\frac{1}{3}\left[\frac{1}{v_L^3} + \frac{2}{v_T^3}\right]\right)^{-1/3}. \quad \text{(E2)}$$

The Debye temperature can be calculated using v_S and the volume per atom V by Eq. (E1).

3. Low temperature heat capacity

To verify speed of sound measurements via pulse-echo ultrasound, low-T heat capacity can be used.

It is possible to determine the so-called Debye level, which is defined as $\beta \rightarrow C_p/T^3$ in the $T \rightarrow 0$ K limit, where C_p is the heat capacity at constant pressure. β is the horizontal plateau that is observed when the low frequency linear dispersion (i.e., speed of sound) makes up the vibrational density of states [i.e., $g(\omega) \propto \omega^2$] and is related to the Debye temperature through the relation

$$\theta_D = \left(\frac{12}{5}\pi^4 NR\right)^{1/3} \beta^{-1/3}, \quad \text{(E3)}$$

where β has units of J mol^{-1} K^{-4}, N is the number of atoms per formula unit, and R is the gas constant. The results of low-T heat capacity have provided excellent verification of the pulse-echo experiments in many systems including PbTe,[95] SnTe,[176] and the $Mg_2(Sb,Bi)_3$ system.[177]

4. High temperature heat capacity

The Debye temperature as obtained from speed of sound and low temperature heat capacity is really a probe of the low frequency acoustic phonons. Therefore, Debye frequency measured via those methods are not always a good estimate for the true maximum vibrational frequency of the solid.[96,178] Another interpretation of the Debye temperature is the temperature at which the heat capacity begins to saturate at high temperatures. In the Debye model for constant volume heat capacity, this corresponds to the temperature when the heat capacity reaches ~95% of the Dulong-Petit value of 3 k_B per atom. As an estimate for the true maximum of the phonon density of states, this definition of the Debye temperature holds even for constant pressure heat capacity. Alternatively, the Debye temperature could be used as a fitting parameter in the constant pressure heat capacity polynomial proposed by Agne *et al.*,[177]

$$c_p = \frac{3NR}{M_W}\left(1 + \frac{1}{10^4}\left(\frac{T}{\theta_D}\right) - \frac{1}{20}\left(\frac{T}{\theta_D}\right)^{-2}\right) + A\left(\frac{T}{\theta_D}\right), \quad \text{(E4)}$$

which captures the Debye-like saturation of heat capacity to the Dulong-Petit value (defined by the number of atoms per formula unit N, the ideal gas constant R, and the molar mass of the formula unit M_W) as well as linear deviations due to anharmonicity and/or electronic contributions.[179]

DATA AVAILABILITY

The data that support the findings of this study are available from the corresponding author upon reasonable request.

REFERENCES

1. K. E. Goodson, "Ordering up the minimum thermal conductivity of solids," Science **315**, 342–343 (2007).
2. K. Chen *et al.*, "Ultrahigh thermal conductivity in isotope-enriched cubic boron nitride," Science **367**, 555–559 (2020).
3. A. Giri *et al.*, "Ultralow thermal conductivity of two-dimensional metal halide perovskites," Nano Lett. **20**, 3331–3337 (2020).
4. A. J. H. McGaughey, A. Jain, and H.-y. Kim, "Phonon properties and thermal conductivity from first principles, lattice dynamics, and the Boltzmann transport equation," J. Appl. Phys. **125**, 011101 (2019).
5. M. F. Horstemeyer, *Integrated Computational Materials Engineering (ICME) for Metals* (John Wiley and Sons, Inc., Hoboken, NJ, 2012).
6. P. Mayer and R. Ram, "Optimization of heat sink-limited thermoelectric generators," Nanoscale Microscale Thermophys. Eng. **10**, 143–155 (2006).
7. R. Warzoha *et al.*, "Applications and impacts of nanoscale thermal transport in electronics packaging," J. Electron. Packag. **143**, 020804 (2020).
8. P. Basnet *et al.*, "Substrate dependent resistive switching in amorphous-HfO_x memristors: An experimental and computational investigation," J. Mater. Chem. C **8**, 5092–5101 (2020).
9. D. G. Pahinkar *et al.*, "Experimental and computational analysis of thermal environment in the operation of HfO_2 memristors," AIP Adv. **10**, 035127 (2020).
10. L. Lindsay, A. Katre, A. Cepellotti, and N. Mingo, "Perspective on *ab initio* phonon thermal transport," J. Appl. Phys. **126**, 050902 (2019).
11. F. DeAngelis *et al.*, "Thermal transport in disordered materials," Nanoscale Microscale Thermophys. Eng. **23**, 81–116 (2019).
12. A. Togo and I. Tanaka, "First principles phonon calculations in materials science," Scr. Mater. **108**, 1–5 (2015).
13. D. G. Cahill *et al.*, "Nanoscale thermal transport. II. 2003–2012," Appl. Phys. Rev. **1**, 011305 (2014).
14. C. Monachon, L. Weber, and C. Dames, "Thermal boundary conductance: A materials science perspective," Ann. Rev. Mater. Res. **46**, 433–463 (2016).
15. M. Simoncelli, N. Marzari, and F. Mauri, "Unified theory of thermal transport in crystals and glasses," Nat. Phys. **15**, 809–813 (2019).
16. L. Isaeva, G. Barbalinardo, D. Donadio, and S. Baroni, "Modeling heat transport in crystals and glasses from a unified lattice-dynamical approach," Nat. Commun. **10**, 3853 (2019).
17. R. W. McKinney, P. Gorai, V. Stevanović, and E. S. Toberer, "Search for new thermoelectric materials with low Lorenz number," J. Mater. Chem. A **5**, 17302–17311 (2017).
18. J. J. Kuo, M. Wood, T. J. Slade, M. G. Kanatzidis, and G. J. Snyder, "Systematic over-estimation of lattice thermal conductivity in materials with electrically-resistive grain boundaries," Energy Environ. Sci. **13**, 1250–1258 (2020).
19. S. Lee *et al.*, "Anomalously low electronic thermal conductivity in metallic vanadium dioxide," Science **355**, 371–374 (2017).
20. L. Jin *et al.*, "Disorder recovers the Wiedemann-Franz law in the metallic phase of VO_2," Phys. Rev. B **102**, 041120(R) (2020).
21. A. Weathers *et al.*, "Significant electronic thermal transport in the conducting polymer poly(3,4-ethylenedioxythiophene)," Adv. Mater. **27**, 2101–2106 (2015).
22. C. Yuan *et al.*, "Modeling and analysis for thermal management in gallium oxide field-effect transistors," J. Appl. Phys. **127**, 154502 (2020).
23. M. I. Hussein, M. J. Leamy, and M. Ruzzene, "Dynamics of phononic materials and structures: Historical origins, recent progress, and future outlook," Appl. Mech. Rev. **66**, 040802 (2014).
24. B. Latour and Y. Chalopin, "Distinguishing between spatial coherence and temporal coherence of phonons," Phys. Rev. B **95**, 214310 (2017).
25. H. R. Seyf, K. Gordiz, F. Deangelis, and A. Henry, "Using Green-Kubo modal analysis (GKMA) and interface conductance modal analysis (ICMA) to study phonon transport with molecular dynamics," J. Appl. Phys. **125**, 081101 (2019).
26. R. J. Hardy, "Energy-flux operator for a lattice," Phys. Rev. **132**, 168–177 (1963).
27. P. B. Allen, J. L. Feldman, J. Fabian, and F. Wooten, "Diffusons, locons and propagons: Character of atomic vibrations in amorphous Si," Philos. Mag. B **79**, 1715–1731 (1999).
28. H. R. Seyf *et al.*, "Rethinking phonons: The issue of disorder," npj Comput. Mater. **3**, 49 (2017).

[29]R. Hanus *et al.*, "Uncovering design principles for amorphous-like heat conduction using two-channel lattice dynamics," Mater. Today Phys. **18**, 100344 (2021).
[30]Y. Luo, X. Yang, T. Feng, J. Wang, and X. Ruan, "Vibrational hierarchy leads to dual-phonon transport in low thermal conductivity crystals," Nat. Commun. **11**, 2554 (2020).
[31]A. Auerbach and P. B. Allen, "Universal high-temperature saturation in phonon and electron transport," Phys. Rev. B **29**, 2884–2890 (1984).
[32]Y. Xia, V. Ozoliņš, and C. Wolverton, "Microscopic mechanisms of glasslike lattice thermal transport in cubic $Cu_{12}Sb_4S_{13}$ tetrahedrites," Phys. Rev. Lett. **125**, 085901 (2020).
[33]J. Carrete *et al.*, "almaBTE: A solver of the space-time dependent Boltzmann transport equation for phonons in structured materials," Comput. Phys. Commun. **220**, 351–362 (2017).
[34]C. Hua and A. J. Minnich, "Transport regimes in quasiballistic heat conduction," Phys. Rev. B **89**, 094302 (2014).
[35]J. Maassen and M. Lundstrom, "Steady-state heat transport: Ballistic-to-diffusive with Fourier's law," J. Appl. Phys. **117**, 035104 (2015).
[36]Y. Guo and M. Wang, "Phonon hydrodynamics and its applications in nanoscale heat transport," Phys. Rep. **595**, 1–44 (2015).
[37]N. Donmezer and S. Graham, "The impact of noncontinuum thermal transport on the temperature of AlGaN/GaN HFETs," IEEE Trans. Electron Dev. **61**, 2041–2048 (2014).
[38]N. Mingo and D. A. Broido, "Length dependence of carbon nanotube thermal conductivity and the 'Problem of Long Waves,'" Nano Lett. **5**, 1221–1225 (2005).
[39]I. Pomeranchuk, "On the thermal conductivity of dielectrics," Phys. Rev. **60**, 820–821 (1941).
[40]A. Herpin, "Contribution à l'ètude de la théorie cinétique des solides," Ann. Phys. **12**, 91–139 (1952).
[41]P. Klemens, "The thermal conductivity of dielectric solids at low temperatures (theoretical)," Proc. R. Soc. London A **208**, 108–133 (1951).
[42]C. Herring, "Role of low-energy phonons in thermal conduction," Phys. Rev. **95**, 954–965 (1954).
[43]B. C. Daly, K. Kang, Y. Wang, and D. G. Cahill, "Picosecond ultrasonic measurements of attenuation of longitudinal acoustic phonons in silicon," Phys. Rev. B **80**, 174112 (2009).
[44]A. Ward and D. a. Broido, "Intrinsic phonon relaxation times from first-principles studies of the thermal conductivities of Si and Ge," Phys. Rev. B **81**, 085205 (2010).
[45]A. A. Maznev and O. B. Wright, "Demystifying umklapp vs normal scattering in lattice thermal conductivity," Am. J. Phys. **82**, 1062–1066 (2014).
[46]F. Yang and C. Dames, "Mean free path spectra as a tool to understand thermal conductivity in bulk and nanostructures," Phys. Rev. B **87**, 035437 (2013).
[47]T.-M. Liu *et al.*, "Anharmonic decay of subterahertz coherent acoustic phonons in GaN," Appl. Phys. Lett. **90**, 041902 (2007).
[48]T.-H. Chou, L. Lindsay, A. A. Maznev, J. S. Gandhi, D. W. Stokes, R. L. Forrest, A. Bensaoula, K. A. Nelson, and C.-K. Sun, "Long mean free paths of room-temperature THz acoustic phonons in a high thermal conductivity material," Phys. Rev. B **100**(9), 094302 (2019).
[49]J. W. L. Pang *et al.*, "Phonon lifetime investigation of anharmonicity and thermal conductivity of UO_2 by neutron scattering and theory," Phys. Rev. Lett. **110**, 157401 (2013).
[50]Z. Tian *et al.*, "Inelastic x-ray scattering measurements of phonon dispersion and lifetimes in $PbTe_{1-x}Se_x$ alloys," J. Phys.: Condens. Mat. **27**, 375403 (2015).
[51]P.-F. Lory *et al.*, "Direct measurement of individual phonon lifetimes in the clathrate compound $Ba_{7.81}Ge_{40.67}Au_{5.33}$," Nat. Commun. **8**, 491 (2017).
[52]G. A. Slack and S. Galginaitis, "Thermal conductivity and phonon scattering by magnetic impurities in CdTe," Phys. Rev. **133**, A253 (1964).
[53]E. S. Toberer, A. Zevalkink, and G. J. Snyder, "Phonon engineering through crystal chemistry," J. Mater. Chem. **21**, 15843 (2011).
[54]M. Roufosse and P. G. Klemens, "Thermal conductivity of complex dielectric crystals," Phys. Rev. B **7**, 5379–5386 (1973).
[55]J. M. Ziman, *Electrons and Phonons: The Theory of Transport Phenomena in Solids* (Oxford University Press, Oxford, 1960).
[56]R. Gurunathan, R. Hanus, and G. J. Snyder, "Alloy scattering of phonons," Mater. Horiz. **7**, 1452–1456 (2020).
[57]R. Berman, E. Foster, and J. Ziman, "The thermal conductivity of dielectric crystals: The effect of isotopes," R. Soc. **237**, 344–354 (1956).
[58]C. A. Ratsifaritana and P. G. Klemens, "Scattering of phonons by vacancies," Intern. J. Thermophys. **8**, 737–750 (1987).
[59]P. G. Klemens, "Phonon scattering by oxygen vacancies in ceramics," Physica B **264**, 263–265 (1999).
[60]P. G. Klemens, "The scattering of low-frequency lattice waves by static imperfections," Proc. Phys. Soc. Sec. A **68**, 1113–1128 (1955).
[61]S.-i. Tamura, "Isotope scattering of dispersive phonons in Ge," Phys. Rev. B **27**, 858–866 (1983).
[62]L. A. Turk and P. G. Klemens, "Phonon scattering by impurity platelet precipitates in diamond," Phys. Rev. B **9**, 4422–4428 (1974).
[63]P. Carruthers, "Scattering of phonons by elastic strain fields and the thermal resistance of dislocations," Phys. Rev. **114**, 995 (1959).
[64]D. C. Wallace, *Thermodynamics of Crystals* (John Wiley and Sons, Inc., New York, 1972).
[65]I.-s. Yang, A. C. Anderson, Y. S. Kim, and E. J. Cotts, "Phonon-dislocation interaction in deformed lithium fluoride," Phys. Rev. B **40**, 1297–1300 (1989).
[66]D.-m. Zhu and A. C. Anderson, "Scattering of phonons by sessile dislocations in deformed germanium," J. Low Temp. Phys. **82**, 37–47 (1991).
[67]H.-S. Kim, S. D. Kang, Y. Tang, R. Hanus, and G. J. Snyder, "Dislocation strain as the mechanism of phonon scattering at grain boundaries," Mater. Horiz. **3**, 234–240 (2016).
[68]T. Wang, J. Carrete, N. Mingo, and G. K. Madsen, "Phonon scattering by dislocations in GaN," ACS Appl. Mater. Interfaces **11**, 8175–8181 (2019).
[69]T. Wang, J. Carrete, A. Van Roekeghem, N. Mingo, and G. K. H. Madsen, "*Ab initio* phonon scattering by dislocations," Phys. Rev. B **95**, 245304 (2017).
[70]Y. Sun *et al.*, "Probing the phonon mean free paths in dislocation core by molecular dynamics simulation," J. Appl. Phys. **129**, 055103 (2021).
[71]B. K. Singh, V. J. Menon, and K. C. Sood, "Phonon conductivity of plastically deformed crystals: Role of stacking faults and dislocations," Phys. Rev. B **74**, 184302 (2006).
[72]J. Hirth and J. Lothe, *Theory of Dislocations*, 2nd ed. (Wiley, New York, 1982).
[73]E. Clouet, "*Ab initio* models of dislocation," in *Handbook of Materials Modeling* (Springer International Publishing, Cham, 2018), pp. 1–22.
[74]P. G. Klemens, "Phonon scattering by Cottrell atmospheres surrounding dislocations," J. Appl. Phys. **39**, 5304–5305 (1968).
[75]T. Ninomiya, "Dislocation vibration and phonon scattering," J. Phys. Soc. Jap. **25**, 830–840 (1968).
[76]M. Li *et al.*, "Nonperturbative quantum nature of the dislocation–phonon interaction," Nano Lett. **17**, 1587–1594 (2017).
[77]M. Li, "Quantized dislocations," J. Phys.: Condens. Matt. **31**, 083001 (2019).
[78]Y. Kogure and Y. Hiki, "Lattice thermal conductivity of crystals containing dislocations," J. Phys. Soc. Jap. **38**, 471–479 (1975).
[79]M. Sato and K. Sumino, "Effect of dislocations on the low temperature thermal conductivity in germanium," J. Phys. Soc. Jpn. **36**, 1075–1083 (1974).
[80]W. Wasserbäch, "Long-range internal stresses and low temperature phonon scattering in plastically deformed niobium and tantalum single crystals," Mater. Sci. Eng. **96**, 167–183 (1987).
[81]Y. Kogure and Y. Hiki, "Effect of dislocations on low-temperature thermal conductivity and specific heat of copper-aluminum alloy crystals," J. Phys. Soc. Jpn. **39**, 698–707 (1975).
[82]H. Li *et al.*, "GaN thermal transport limited by the interplay of dislocations and size effects," Phys. Rev. B **102**, 014313 (2020).
[83]K. Termentzidis *et al.*, "Impact of screw and edge dislocations on the thermal conductivity of individual nanowires and bulk GaN: A molecular dynamics study," Phys. Chem. Chem. Phys. **20**, 5159–5172 (2018).
[84]M. Li *et al.*, "Theory of electron-phonon-dislon interacting system: Toward a quantized theory of dislocations," New J. Phys. **20**, 023010 (2018).
[85]W. Cai and W. Nix, *Imperfections in Crystalline Solids* (Cambridge University Press, Cambridge, 2016).
[86]W. T. Read and W. Shockley, "Dislocation models of crystal grain boundaries," Phys. Rev. **78**, 275–289 (1950).

[87] L. Priester, *Grain Boundaries from Theory to Engineering* (Springer, 2006).
[88] M. Kleman and J. Friedel, "Disclinations, dislocations, and continuous defects: A reappraisal," Rev. Mod. Phys. **80**, 61–115 (2008).
[89] M. Kléman, "Curved crystals, defects and disorder," Adv. Phys. **38**, 605–667 (1989).
[90] R. C. Morris, "Disclination-dislocation model of metallic glass structures," J. Appl. Phys. **50**, 3250–3257 (1979).
[91] R. M. J. Cotterill, W. D. Kristensen, and E. J. Jensen, "Molecular dynamics studies of melting: III. Spontaneous dislocation generation and the dynamics of melting," Philos. Mag. **30**, 245–263 (1974).
[92] V. Osipov and S. Krasavin, "Disclination dipoles as the basic structural elements of dielectric glasses," Phys. Lett. A **250**, 369–374 (1998).
[93] B. Sun *et al.*, "Dislocation-induced thermal transport anisotropy in single-crystal group-III nitride films," Nat. Mater. **18**, 136–141 (2018).
[94] Z. Chen *et al.*, "Lattice dislocations enhancing thermoelectric PbTe in addition to band convergence," Adv. Mater. **29**, 1606768 (2017).
[95] R. Hanus *et al.* "Lattice softening significantly reduces thermal conductivity and leads to high thermoelectric efficiency," Adv. Mater. **31**, 1900108 (2019).
[96] M. T. Agne, R. Hanus, and G. J. Snyder, "Minimum thermal conductivity in the context of diffuson-mediated thermal transport," Energy Environ. Sci. **11**, 609–616 (2018).
[97] T. Krauskopf *et al.*, "Comparing the descriptors for investigating the influence of lattice dynamics on ionic transport using the superionic conductor $Na_3PS_{4-x}Se_x$," J. Am. Chem. Soc. **140**, 14464–14473 (2018).
[98] O. L. Anderson, "A simplified method for calculating the Debye temperature from elastic constants," J. Phys. Chem. Solids **24**, 909–917 (1963).
[99] P. Brüesch, *Phonons: Theory and Experiments II: Experiments and Interpretation of Experimental Results* (Springer Science & Business Media, 2012), Vol. 65.
[100] T. J. Slade *et al.*, "Charge-carrier-mediated lattice softening contributes to high zT in thermoelectric semiconductors," Joule **5**, 1168–1182 (2021).
[101] F. Kargar *et al.*, "Acoustic phonon spectrum engineering in bulk crystals via incorporation of dopant atoms," Appl. Phys. Lett. **112**, 191902 (2018).
[102] A. Yelon, B. Movaghar, and H. Branz, "Origin and consequences of the compensation (Meyer-Neldel) law," Phys. Rev. B **46**, 12244 (1992).
[103] C. A. Geiger, *Solid Solutions in Silicate and Oxide Systems* (Mineralogical Society of Great Britain and Ireland, 2001), Vol. 3.
[104] C. Zener, "Relation between residual strain energy and elastic moduli," Acta Crystallogr. **2**, 163–166 (1949).
[105] D. G. Cahill and R. Pohl, "Heat flow and lattice vibrations in glasses," Solid State Commun. **70**, 927–930 (1989).
[106] D. Xu *et al.*, "Thermal boundary resistance correlated with strain energy in individual Si film-wafer twist boundaries," Mater. Today Phys. **6**, 53–59 (2018).
[107] Z. Cheng *et al.*, "Thermal conductance across harmonic-matched epitaxial Al-sapphire heterointerfaces," Commun. Phys. **3**, 115 (2020).
[108] P. K. Schelling, S. R. Phillpot, and P. Keblinski, "Kapitza conductance and phonon scattering at grain boundaries by simulation," J. Appl. Phys. **95**, 6082–6091 (2004).
[109] J. Hickman and Y. Mishin, "Thermal conductivity and its relation to atomic structure for symmetrical tilt grain boundaries in silicon," Phys. Rev. Mater. **4**, 033405 (2020).
[110] R. Gurunathan, R. Hanus, S. Graham, A. Garg, and G. J. Snyder, "Thermal resistance at a twist boundary and a semicoherent heterointerface," Phys. Rev. B **103**, 144302 (2021).
[111] D. G. Cahill and R. O. Pohl, "Thermal conductivity of amorphous solids above the plateau," Phys. Rev. B **35**, 4067–4073 (1987).
[112] Y. K. Koh *et al.*, "Comparison of the 3ω method and time-domain thermoreflectance for measurements of the cross-plane thermal conductivity of epitaxial semiconductors," J. Appl. Phys. **105**, 054303 (2009).
[113] Y. K. Koh, C. J. Vineis, S. D. Calawa, M. P. Walsh, and D. G. Cahill, "Lattice thermal conductivity of nanostructured thermoelectric materials based on PbTe," Appl. Phys. Lett. **94**, 153101 (2009).
[114] D. G. Cahill, "Analysis of heat flow in layered structures for time-domain thermoreflectance," Rev. Sci. Instrum. **75**, 5119–5122 (2004).
[115] A. J. Schmidt, "Pump-probe thermoreflectance," Ann. Rev. Heat Transfer **16**, 159–181 (2013).
[116] P. Jiang, X. Qian, and R. Yang, "Tutorial: Time-domain thermoreflectance (TDTR) for thermal property characterization of bulk and thin film materials," J. Appl. Phys. **124**, 161103 (2018).
[117] M. S. B. Hoque *et al.*, "Thermal conductivity measurements of sub-surface buried substrates by steady-state thermoreflectance," (2021) arXiv:2102.12954.
[118] R. Hanus, A. Garg, and G. J. Snyder, "Phonon diffraction and dimensionality crossover in phonon-interface scattering," Commun. Phys. **1**, 78 (2018).
[119] E. T. Swartz and R. O. Pohl, "Thermal boundary resistance," Rev. Mod. Phys. **61**, 605–668 (1989).
[120] Q. Meng, L. Wu, and Y. Zhu, "Phonon scattering of interfacial strain field between dissimilar lattices," Phys. Rev. B **87**, 064102 (2013).
[121] G. Varnavides, A. S. Jermyn, P. Anikeeva, and P. Narang, "Nonequilibrium phonon transport across nanoscale interfaces," Phys. Rev. B **100**, 115402 (2019).
[122] E. Y. Chen, R. Dingreville, and C. Deo, "Misfit dislocation networks in semi-coherent miscible phase boundaries: An example for U-Zr interfaces," Comput. Mater. Sci. **154**, 194–203 (2018).
[123] K. Tai, A. Lawrence, M. P. Harmer, and S. J. Dillon, "Misorientation dependence of Al_2O_3 grain boundary thermal resistance," Appl. Phys. Lett. **102**, 034101 (2013).
[124] Y. Sun *et al.*, "Phonon scattering in the complex strain field of a dislocation," J. Mater. Chem. C. **9**, 8506–8514 (2021).
[125] Z. Wang, J. E. Alaniz, W. Jang, J. E. Garay, and C. Dames, "Thermal conductivity of nanocrystalline silicon: Importance of grain size and frequency-dependent mean free paths," Nano Lett. **11**, 2206–2213 (2011).
[126] C. Hua, X. Chen, N. K. Ravichandran, and A. J. Minnich, "Experimental metrology to obtain thermal phonon transmission coefficients at solid interfaces," Phys. Rev. B **95**, 205423 (2017).
[127] C. Hua and A. J. Minnich, "Importance of frequency-dependent grain boundary scattering in nanocrystalline silicon and silicon-germanium thermoelectrics," Semicond. Sci. Technol. **29**, 124004 (2014).
[128] R. Berman, "The thermal conductivity of some polycrystalline solids at low temperatures," Proc. Phys. Soc. Sec. A **65**, 1029–1040 (1952).
[129] K. Watari *et al.*, "Thermal conductivity of AlN ceramic with a very low amount of grain boundary phase at 4 to 1000 K," J. Mater. Res. **17**, 2940–2944 (2002).
[130] C. Dames and G. Chen, "Theoretical phonon thermal conductivity of Si/Ge superlattice nanowires," J. Appl. Phys. **95**, 682–693 (2004).
[131] D. Dangić, É. D. Murray, S. Fahy, and I. Savić, "Structural and thermal transport properties of ferroelectric domain walls in GeTe from first principles," Phys. Rev. B **101**, 184110 (2020).
[132] R. Landauer, "Spatial variation of currents and fields due to localized scatterers," IBM J. **1**, 223–231 (1957).
[133] P.-a. Zong *et al.*, "Skutterudite with graphene-modified grain-boundary complexion enhances zT enabling high-efficiency thermoelectric device," Energy Environ. Sci. **10**, 183–191 (2017).
[134] Q. Zhang *et al.*, "Realizing high-performance thermoelectric power generation through grain boundary engineering of skutterudite-based nanocomposites," Nano Energy **41**, 501–510 (2017).
[135] Z. Zhou *et al.*, "Microstructure and composition engineering Yb single-filled $CoSb_3$ for high thermoelectric and mechanical performances," J. Materiom. **5**, 702–710 (2019).
[136] K. Gordiz and A. Henry, "Phonon transport at interfaces: Determining the correct modes of vibration," J. Appl. Phys. **119**, 015101 (2016).
[137] K. Gordiz and A. Henry, "A formalism for calculating the modal contributions to thermal interface conductance," New J. Phys. **17**, 103002 (2015).
[138] K. Gordiz and A. Henry, "Phonon transport at crystalline Si/Ge interfaces: The role of interfacial modes of vibration," Sci. Rep. **6**, 23139 (2016).
[139] A. Giri and P. E. Hopkins, "Role of interfacial mode coupling of optical phonons on thermal boundary conductance," Sci. Rep. **7**, 11011 (2017).
[140] A. Maiti, G. D. Mahan, and S. T. Pantelides, "Dynamical simulations of non-equilibrium processes — Heat flow and the Kapitza resistance across grain boundaries," Solid State Commun. **102**, 517–521 (1997).
[141] W. Lv and A. S. Henry, "Examining the validity of the phonon gas model in amorphous materials," Sci. Rep. **6**, 37675 (2016).
[142] S. Sadasivam *et al.*, "The atomistic Green's function method for interfacial phonon transport," Ann. Rev. Heat Transfer **17**, 89–145 (2014).

[143]W. Zhang, T. S. Fisher, and N. Mingo, "Simulation of interfacial phonon transport in Si-Ge heterostructures using an atomistic Green's function method," J. Heat Transfer **129**, 483–491 (2007).
[144]J. Dai and Z. Tian, "Rigorous formalism of anharmonic atomistic Green's function for three-dimensional interfaces," Phys. Rev. B **101**, 041301 (2020).
[145]J. Moon, B. Latour, and A. J. Minnich, "Propagating elastic vibrations dominate thermal conduction in amorphous silicon," Phys. Rev. B **97**, 024201 (2018).
[146]J. Moon *et al.*, "Thermal acoustic excitations with atomic-scale wavelengths in amorphous silicon," Phys. Rev. Mater. **3**, 065601 (2019).
[147]D. R. Clarke, "Materials selection guidelines for low thermal conductivity thermal barrier coatings," Surf. Coat. Technol. **163–164**, 67–74 (2003).
[148]A. Einstein, "Elementare betrachtungen über die thermische molekularbewegung in festen körpern," Ann. Phys. **340**, 679–694 (1911).
[149]C. Kittel, "Interpretation of the thermal conductivity of glasses," Phys. Rev. **75**, 972 (1949).
[150]R. Pohl, "Lattice vibrations of glasses," J. Non-Cryst. Solids **352**, 3363–3367 (2006).
[151]M. Simkin and G. Mahan, "Minimum thermal conductivity of superlattices," Phys. Rev. Lett. **84**, 927 (2000).
[152]Z. Chen and C. Dames, "An anisotropic model for the minimum thermal conductivity," Appl. Phys. Lett. **107**, 193104 (2015).
[153]J. L. Feldman, M. D. Kluge, P. B. Allen, and F. Wooten, "Thermal conductivity and localization in glasses: Numerical study of a model of amorphous silicon," Phys. Rev. B **48**, 12589–12602 (1993).
[154]P. B. Allen and J. L. Feldman, "Thermal conductivity of glasses: Theory and application to amorphous Si," Phys. Rev. Lett. **62**, 645–648 (1989).
[155]T. Watanabe *et al.*, "Thermal transport in off-stoichiometric uranium dioxide by atomic level simulation," J. Am. Ceram. Soc. **92**, 850–856 (2009).
[156]H. R. Seyf and A. Henry, "A method for distinguishing between propagons, diffusions, and locons," J. Appl. Phys. **120**, 025101 (2016).
[157]G. Barbalinardo, Z. Chen, N. W. Lundgren, and D. Donadio, "Efficient anharmonic lattice dynamics calculations of thermal transport in crystalline and disordered solid," J. Appl. Phys. **128**, 135104 (2020).
[158]Y. Xia, K. Pal, J. He, V. Ozoliņš, and C. Wolverton, "Particlelike phonon propagation dominates ultralow lattice thermal conductivity in crystalline Tl_3VSe_4," Phys. Rev. Lett. **124**, 065901 (2020).
[159]G. A. Slack, "The thermal conductivity of nonmetallic crystals," Solid State Phys. **34**, 1–71 (1979).
[160]X. Chen *et al.*, "Twisting phonons in complex crystals with quasi-one-dimensional substructures," Nat. Commun. **6**, 6723 (2015).
[161]S. Mukhopadhyay *et al.*, "Two-channel model for ultralow thermal conductivity of crystalline Tl_3VSe_4," Science **360**, 1455–1458 (2018).
[162]Z. Chen, X. Zhang, S. Lin, L. Chen, and Y. Pei, "Rationalizing phonon dispersion for lattice thermal conductivity of solids," Nat. Sci. Rev. **5**, 888–894 (2018).
[163]S. Muy *et al.*, "Tuning mobility and stability of lithium ion conductors based on lattice dynamics," Energy Environ. Sci. **11**, 850–859 (2018).
[164]J. Ding *et al.*, "Anharmonic lattice dynamics and superionic transition in $AgCrSe_2$," Proc. Natl. Acad. Sci. **117**, 3930–3937 (2020).
[165]*VASP*, https://www.vasp.at/.
[166]*QuantumEspresso*, https://www.quantum-espresso.org/.
[167]Phonopy, https://atztogo.github.io/phonopy/index.html.
[168]almaBTE database, http://www.almabte.eu/index.php/database/.
[169]N. K. Ravichandran and D. Broido, "Unified first-principles theory of thermal properties of insulators," Phys. Rev. B **98**, 085205 (2018).
[170]Y. Xia, "Revisiting lattice thermal transport in PbTe: The crucial role of quartic anharmonicity," Appl. Phys. Lett. **113**, 073901 (2018).
[171]T. Feng, L. Lindsay, and X. Ruan, "Four-phonon scattering significantly reduces intrinsic thermal conductivity of solids," Phys. Rev. B **96**, 161201(R) (2017).
[172]P. Klemens, "Thermal conductivity and lattice vibrational modes," J. Phys. C **7**, 1–98 (1958).
[173]L. Lindsay, D. A. Broido, and T. L. Reinecke, "*Ab initio* thermal transport in compound semiconductors," Phys. Rev. B **87**, 165201 (2013).
[174]N. W. Ashcroft and N. D. Mermin, *Solid State Physics* (Thomson Learning, Inc., Boston, 1976).
[175]R. Truell, C. Elbaum, and B. B. Chick, *Ultrasonic Methods in Solid State Physics* (Academic Press Inc., New York, 1969).
[176]G. Tan *et al.*, "High thermoelectric performance in SnTe-$AgSbTe_2$ alloys from lattice softening, giant phonon-vacancy scattering, and valence band convergence," ACS Energy Lett. **3**, 705–712 (2018).
[177]M. T. Agne *et al.*, "Heat capacity of Mg_3Sb_2, Mg_3Bi_2 and their alloys at high temperature," Mater. Today Phys. **6**, 83–88 (2018).
[178]R. Pässler, "Moments of phonon density of states spectra and characteristic phonon temperatures of wide band gap materials," Phys. Status Solidi B **243**, 2719–2727 (2006).
[179]M. T. Agne, "Thermodynamic insights and microscopic models for characterizing vibrations in solids," Ph.D. thesis, Northwestern University (2020).
[180]Equation (21) is a factor of 3 smaller than Klemens' expression, Eq. 65 of Ref. 60 (which is given for $\theta = \pi/2$). This may be due to differences in assumptions regarding mode conversion when computing the scattering phase space. If one assumes a phonon can scatter into any three of the acoustic branches, then the phase space contribution is $3g_{2d}$. Since in full detail the matrix element will contain a dot product between the incident phonon eigenvector (polarization vector) and the scattered phonon eigenvector, we use g_{2d}.
[181]K. Sääskilahti, J. Oksanen, J. Tulkki, and S. Volz, "Role of anharmonic phonon scattering in the spectrally decomposed thermal conductance at planar interfaces," Phys. Rev. B: Cond. Mat. Mater. Phys. **90**(13), 1–8 (2014).
[182]Y. Guo, Z. Zhang, M. Bescond, S. Xiong, M. Nomura, and S. Volz, "Anharmonic phonon-phonon scattering at the interface between two solids by nonequilibrium Green's function formalism," Phys. Rev. B **103**(17), 174306 (2021).
[183]J. Amrit, A. Ramiere, and S. Volz, "Role of fluttering dislocations in the thermal interface resistance between a silicon crystal and plastic solid," Phys. Rev. B **97**(1), 014308 (2018).